State-Constrained Rotational and Translational Motion Control with Applications to Monolithic and Distributed Spacecraft

Unsik Lee

A dissertation
submitted in partial fulfillment of the
requirements for the degree of

Doctor of Philosophy

University of Washington

2014

Reading Committee:

Mehran Mesbahi, Chair

Brian C. Fabien

Uy-Loi Ly

Mehran Mesbahi

Program Authorized to Offer Degree:
Aeronautics & Astronautics

University of Washington

Abstract

State-Constrained Rotational and Translational Motion Control with Applications to Monolithic and Distributed Spacecraft

Unsik Lee

Chair of the Supervisory Committee:
Professor Mehran Mesbahi
Aeronautics & Astronautics

The research presented in this dissertation deals with translationally and rotationally constrained motion planning for space systems. The topology of the configuration manifold for rigid body systems is fundamentally challenging from a control perspective. This is because the rotational configuration space of rigid body systems is a boundless but compact manifold that does not admit a globally continuous feedback control law. This becomes more troublesome when planning a re-orientation in the presence of rotationally constrained zones. Such problems are of paramount importance as these constraints frequently arise in many space science missions such as space telescope or interferometers; they also pose a challenging computational task for the spacecraft's guidance, navigation, and control subsystem. The complexity of such problems is elevated due to the fact that removing the constrained zones from the boundless compact manifold results in a non-convex region.

In the first part of this dissertation, a novel guidance algorithm is proposed to handle multiple types of attitude constrained zones. Two types of attitude constrained zones are as examined and we show that such attitude constrained zones can be represented as convex regions. The advantage of the proposed approach hinges upon the development of the novel strictly convex logarithmic barrier potential functional that is subsequently used for constructing two types of control laws.

The second part of this dissertation handles the problem of achieving identical orientation

for a group of spacecraft in the presence of rotationally constrained zones. A distributed algorithm for consensus of multiple agents is developed where the shared state is assumed to be constrained in a distinct compact convex set and then augmented to fit in the constrained reorientation framework presented earlier. This consensus algorithm is applicable when each spacecraft is required to satisfy its own attitude constraints while also synchronizing with other spacecraft. Two sets of simulations of synchronizing space interferometers with identical and independent rotationally constrained zones are presented.

In the final part of the dissertation, as an extension to the first part of the dissertation, a general framework for the analysis of rotationally and translationally constrained spacecraft control problems is presented. The general dynamics of the rigid body is addressed in terms of unit dual quaternions parameterizing position and attitude-dependent variables, and an almost globally stable control law is developed for unconstrained rigid-body dynamics via a convex energy like Lyapunov function. The novelty of the unit dual quaternion based approach hinges on the fact that translationally and rotationally constrained zones can be formulated as convex representable sets. Moreover, a convex programming approach is proposed to control synthesis of a planet lander that has the aforementioned constrained zones as its mission requirements. The numerical simulations validate that the proposed approach successfully find feasible trajectories satisfying all mission constraints.

TABLE OF CONTENTS

ACKNOWLEDGMENTS

Many people have contributed, in different ways, to the development of this dissertation and, unfortunately, I cannot take the space to thank them all.

My advisor, Mehran Mesbahi, deserves the first and warmest thanks for his supervision and support. My research here could not have been accomplished without his guidance. I am really in debt with him for helping me opening a tiny door to a huge new world. I extend my appreciation and sincere thanks to the rest of my dissertation committee, Dr. Uy-Loi Ly, Dr. Kristi Morgansen, Dr. Jim Hermanson, Dr. Mitsuru Kurosaka and Dr. Brian C. Fabien whom I had the pleasure to learn from at University of Washington.

Further thanks are given to my fellow lab mates and all my Korean friends that have each contributed in their own ways and have helped to make my research journey all that more rewarding.

Finally, I would like to manifest my deepest gratitude and appreciation to my parents, for their relentless support and unconditional love and to my wife Kotsong and son Daniel for the warmest love and encouragement.

DEDICATION

To my dear wife Kotsong and son Daniel.

NOMENCLATURE

$\mathbb{R}$	set of real numbers
$\mathbb{R}^n$	n-dimensional Euclidean space
$\mathbb{R}^{n\times m}$	set of $n \times m$ real matrices
$\mathbb{R}_{++}$	set of positive real numbers
$\mathbb{R}_{+}$	set of nonnegative real numbers
$\mathbb{S}^n$	set of $n \times n$ symmetric matrices
$\mathbb{S}^n_{++}$	set of $n \times n$ positive definite matrices
$\mathsf{SO}(3)$	special orthogonal group of 3 dimension
$\mathsf{SE}(3)$	special Euclidean group of 3 dimension
$\mathcal{S}^3$	Three-dimensional surface of an unit ball in three-dimensional space
$\mathbf{I}_n$	n-dimensional identity matrix
$\mathbf{0}_{n\times m}$	$n \times m$ zero matrix
$\mathbf{q}$	unit quaternion; $\mathbf{q} = [\, \boldsymbol{q}^T \quad q_0 \,]^T$
$\mathbf{q}^*$	unit quaternion conjugate
$\tilde{\mathbf{q}}$	unit dual quaternion; $\tilde{\mathbf{q}} = [\, \mathbf{q}_1^T \quad \mathbf{q}_2^T \,]^T$

$\tilde{\mathbf{q}}^*$	unit dual quaternion conjugate
$\boldsymbol{q}$	vector part of the unit quaternion $\mathbf{q}$
q_o	scalar part of the unit quaternion
$\mathbf{q_I}$	identity unit quaternion $\mathbf{q_I} = [\,0\;0\;0\;1\,]^T$
$\tilde{\mathbf{q}}_\mathbf{I}$	identity unit dual quaternion $\tilde{\mathbf{q}}_\mathbf{I} = [\,0\;0\;0\;1\;0\;0\;0\;0\,]^T$
$\mathbf{q}_{\boldsymbol{d}}$	desired attitude in unit quaternion
$\tilde{\mathbf{q}}_{\boldsymbol{r}}$	desired unit dual quaternion
$\mathbf{U}_\mathbf{q}$	set of unit quaternions
$\mathbf{q}_{\boldsymbol{f}}$	complement of attitude forbidden zone
$\mathbf{q}_{\boldsymbol{M}}$	set of attitude mandatory zone
$\mathbf{q}_{\boldsymbol{p}}$	set of attitude permissible zone
∂D	boundary of the set D
$\boldsymbol{x} \cdot \boldsymbol{y}$	dot product between vectors $\boldsymbol{x}$ and $\boldsymbol{y}$
$\otimes$	quaternion multiplication
ω	angular velocity vector in the body frame
$R(\boldsymbol{\omega})$	cross product operator associated with $\boldsymbol{\omega}$
$\boldsymbol{\omega}$	angular velocity in quaternion form; $\boldsymbol{\omega} = [\,\omega^T\;0\,]^T$

$\|x\|$	Euclidean 2-norm of vector or quaternion x
$\texttt{diag}(x)$	diagonal matrix with the vector x on its diagonal
$\texttt{Vec}[\,\cdot\,]$	3×1 vector part of the argument

Chapter 1

INTRODUCTION

1.1 Rotationally and Translationally Constrained Motion Control

One of the enabling technologies for spacecraft autonomy is the capability to autonomously and optimally execute a reorientation and translation of the spacecraft while operating under a number of celestial and dynamic constraints. In the field of astronautics, this type of maneuvering occurs often in a number of deep space and earth orbiting missions. For example, spacecraft involved in science missions are often equipped with sensitive instruments, such as infrared telescopes or interferometers, which require re-targeting while avoiding direct exposure to the sunlight or other bright objects; see Fig. 1.1.

This requirement is sometimes accompanied by additional desired maneuvers. For example, the relative orientation of the spacecraft with respect to a fixed object is affected

Figure 1.1: Applications of rotationally and translationally constrained motion planning. Courtesy of NASA/JPL-Caltech

not only by a pure rotation but also by a pure translation, e.g., the Mars lander in its final approach requires that a clear view from a human or certain sensors to a target landing location should be maintained while translationally and rotationally maneuvering for hazard detection and avoidance.

The task of planning attitude and position trajectories that meet all constraints is of paramount importance in such science missions; it also poses a challenging computational task for the spacecraft's guidance, navigation, and control subsystem. The fundamental complexity of such a problem is mainly due to the fact that the special Euclidean group $\mathsf{SE}(3)$, the configuration space for translational and rotational dynamics, is topologically complex, and removing the constrained subset from this configuration space results in a *non-convex* region.

The main goal of this dissertation is the modeling and control of the dynamics of spacecraft the motion of a rigid body in the presence of rotationally and translationally constrained zones by utilizing a novel parameterization of the configuration space. We then present a convex optimization framework to design the maneuvers for a single spacecraft in such a constrained space. The proposed framework is then extended to distributed spacecraft systems. The proposed algorithm enables a spacecraft network to synchronize on their respective dynamic states while also ensuring that individual spacecraft are constrained in independently defined, rotationally-constrained configuration spaces.

1.2 Dissertation Outline

This dissertation can be broadly divided into three parts, depending on the types of parametrization of the configuration space for the spacecraft and their respective missions. The first part comprised of Chapters 2 and 3, where we utilize a *unit quaternion parameterization* to model spacecraft rotational dynamics. We start with a discussion of the advantages of a unit quaternion representation over other representations. In particular, we present the reason why the unit quaternion representation is an ideal choice for parameterizing the rotational dynamics of the spacecraft when considering constrained rotational maneuvers. In addition, we address some of the issues with using unit quaternion representations pertaining to "almost global stability" of the resulting dynamics and the "unwinding phenomenon"

that are also treated in the same context. We then proceed to formulate a convex framework for attitude reorientation planning in the presence of rotationally constrained zones. The advantage of the proposed approach hinges upon the development of a novel strictly convex logarithmic barrier potential that is subsequently used for constructing two types of control laws. Such an approach would enable addressing the feasibility of the spacecraft mission even in highly constrained scenarios. In addition, we investigate quaternion based time/energy-optimal spacecraft reorientation via a judiciously formulated nonlinear optimal control problem, which is subsequently solved using a Gauss pseudospectral method. The first part concludes with extensive simulation results, including typical scenarios faced by many science missions as well as more complex scenarios, in order to demonstrate the viability of the proposed methodology.

The second part of the dissertation includes Chapter 4, where the problem of achieving an identical orientation for a group of spacecraft in the presence of rotationally constrained zones is addressed. In order to develop such an algorithm, we first present a distributed algorithm for consensus of multiple agents where the shared state is assumed to be constrained in a distinct compact convex set. We then show that following the proposed distributed protocol, the agents are guaranteed to reach an agreement on a state that lies at the intersection of individual convex constraint sets. This consensus algorithm is applicable when each spacecraft is required to satisfy its own constraints while also synchronizing with other spacecraft. The spacecraft attitude synchronization problem in the presence of rotationally constrained zones is then formulated based on the proposed distributed protocol. The rotationally constrained zones can be identically defined over the group of spacecraft or can be defined independently. In order to evaluate the effectiveness of the algorithm, we present two sets of simulations where synchronization of six spacecraft with identical and independent rotationally constrained zones with random initial attitudes are considered.

In Chapter 5, as an extension to the first part of the dissertation, we present the general framework for the analysis of rotationally and translationally constrained spacecraft control problems. This study has been inspired by the fact that rotationally constrained zones are often affected by pure translational motions. The challenge for such a problem setup hinges on the fact that dependent variables evolve in distinct configuration spaces- as such,

we adopt a new parameterization, namely, *unit dual quaternions* that can capture this dependency. Using this novel parameterization, we address the general dynamics of the rigid body in terms of *unit dual quaternions*. Moreover, we develop an almost globally stable control laws for unconstrained rigid-body dynamics via a convex energy like Lyapunov function on unit dual quaternions. We then proceed to characterize the convex representable subsets of unit dual quaternion that correspond to translational and rotational states that satisfy a predefined field of view constraints with respect to the body frame. Moreover, we propose a semi-definite programming approach to control synthesis of a planet lander that has the aforementioned constrained zones as its mission requirements. Chapter 5 is concluded with an extensive set of numerical simulations demonstrating the proposed algorithmic approach to constrained spacecraft motion planning problems.

Chapter 2

QUATERNION-BASED ATTITUDE CONTROL

2.1 Attitude Control and Literature Review

Rigid body control has received ample attention from researchers as it is motivated by numerous mechanical applications that involve attitude maneuvering or stabilization, such as spacecraft and atmospheric flight vehicles. Since rigid body control problems are inherently nonlinear, these problems can be categorized into local attitude control with a linearized model, and global attitude control with a nonlinear model. Briefly speaking, local attitude control handles relatively small attitude and angular velocity changes evolve a close neighborhood of equilibrium points with a set of accurate linearized dynamics. On the other hand, global attitude control uses nonlinear dynamics in order to take large angle and angular velocity maneuvering into account. Therefore, local attitude control is typically appropriate for orientation keeping in the presence of small disturbances, whereas global attitude control is suitable when there are arbitrary changes in spacecraft attitude. In this dissertation, we limit our attention to the global attitude control problem based on non-simplified dynamics, since generally, rotationally constrained zones are widely defined over the rotational configuration space such that they cannot be handled by local attitude control schemes. Henceforth, we will refer to the problem considered as the attitude reorientation problem.

Attitude reorientation algorithms have been studied in the context of two different control mechanisms: open-loop and closed-loop control. Open-loop control, generally based on a pre-calculated attitude maneuver trajectory, are designed based on a two-point boundary

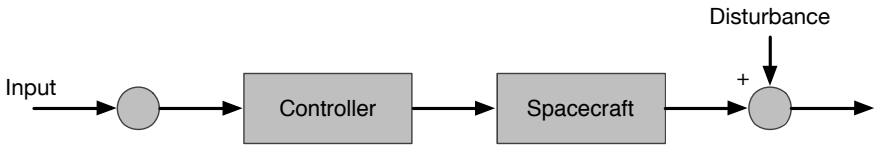

Figure 2.1: Open loop control system

value problem using optimal control techniques. The time/energy optimal attitude maneuver control addressed in §3.6 is an example of an open-loop control law. Such a control algorithm has the advantage that it can present more optimal control schemes regardless of time restrictions, but it does not have guaranteed robustness against system uncertainty and external disturbances, since it cannot exploit information to be used for corrective measures coming from real-time feedback; see Fig. 2.1. Therefore, in general, open-loop-based controllers are sensitive to the aforementioned factors as well as to non-nominal initial conditions. Notable works in this open-loop approach include Xin and Pan [76], Vadali and Junkins [38], Bilimoria and Wie [106], and Lai *et al* [107]. Recently, a nonlinear programming problem using the Legendre pseudo-spectral method at a set of discretization points has been applied for time/energy-optimal rest-to-rest maneuvers of under-actuated spacecraft [27]. This approach has been successfully used in §3.6 to generate time/energy optimal spacecraft attitude maneuver trajectories in the presence of rotationally constrained zones, and subsequently the result was compared with closed-loop control laws addressed in the dissertation. The other approach for spacecraft control is based on feedback. As seen in Fig. 2.2, this approach can calculate an error from the knowledge of disturbances fed by feedback. Thus, such a mechanism is more robust against disturbances. On that account, various feedback approaches have been implemented in the literature. In particular, in the field of aerospace, the spacecraft reorientation problem in the absence of attitude constrained zones has been comprehensively addressed with nonlinear control in terms of feedback [23, 37, 41, 52, 60, 75, 85, 111]. For instance, back-stepping [36, 41, 72, 111], sliding mode control [85], and adaptive control [23, 37] have been applied over recent decades. Moreover, in [54, 76, 82] the problem has been examined in the optimal control framework. In particu-

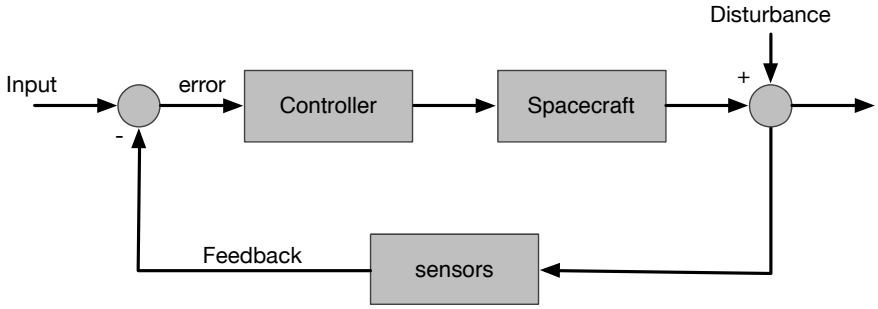

Figure 2.2: Closed loop attitude control system

lar, Robinett *et al* [39] have developed saturated control design based on Lyapunov's direct method, which turned out to be effective in real situations. In addition, model-independent control laws that are robust against uncertainties in the spacecraft's moment of inertia have been explored by Wie and Barba [6], Wie *et al.* [3] and Wie and Lu [56]. Inspired by their approach, we address a model independent control law for spacecraft reorientation as well as a back-stepping based model dependent control law both in the presence of attitude constrained zones.

2.2 Unit Quaternions and $\mathsf{SO}(3)$

2.2.1 Rotation and Orientation

The rotation of a rigid body can be considered as a length preserving linear transformation between an inertially fixed and a body fixed frame in Euclidean space. Such a transformation can be represented by 3×3 orthogonal matrices whose determinant is 1, namely *rotation matrices*. The amount of rotation of a rigid body with respect to an inertially fixed frame represents the *attitude of the rigid body*. Therefore, we can define the configuration space of the attitude of a rigid body as a group of all possible rotations can be represented by the set of all rotation matrices, which is referred to as $\mathsf{SO}(3)$, the *special orthogonal group* of a rigid body rotation in as

$$\mathsf{SO}(3) = \{\, R \in \mathbb{R}^{3\times 3} \mid R^T R = \mathbb{I}_3 \text{ and } \det(R) = 1 \,\}, \tag{2.1}$$

Attitude Representation	Singularity	Uniqueness	Embedded Space
Rotation matrix	No	Yes	$\mathbb{R}^{3\times3}$
Unit quaternion	No	No	$\mathcal{S}^3$
Modified Rodrigues parameters	Yes	No	$\mathbb{R}^3$
Axis-angle	No	No	$\mathbb{R}^4$
Euler angles	Yes	No	$\mathbb{R}^3$

Table 2.1: Properties of various attitude representations

where R denotes a rotation matrix and $\mathbb{I}_3$ denotes the identity matrix in $\mathbb{R}^{3\times3}$. The topological structure of such a group is non-Euclidean, which forms a topologically difficult manifold. In particular, $\mathsf{SO(3)}$ forms a boundary-less compact manifold, which is not diffeomorphic to any vector space [7]. This simple fact precludes the existence of any continuous feedback control law which is *globally asymptotically stable* around a desired attitude; we address this issue in §2.3.

Apart from this issue, the rotation matrix is composed of 9 elements with 6 constraints. This sometimes leads to inefficiencies in handling due to the complexity coming from extra matrix multiplication and memory management issues. Thus, attitude control is typically studied using various reduced attitude parameterizations of $\mathsf{SO(3)}$ such as Euler angles, and unit quaternions, even though there is no reduced parameterization that can replace $\mathsf{SO(3)}$ globally and uniquely [16, 86, 93] due to the distinct topological complexity of $\mathsf{SO(3)}$; see Table 2.1. Attitude parameterizations can be categorized into two types, Euclidean and Non-Euclidean. The Euclidean parameterizations have the advantage that it allows methods of analysis that are suitable for the Euclidean space $\mathbb{R}^3$. However, $\mathsf{SO(3)}$ is inherently non-Euclidean; Euclidean three parameter representations naturally possess singularities [40]. For example, Euler angles ($\mathsf{SO(3)} \mapsto \mathbb{R}^3$), which are broadly used in applications are Euclidean and intuitive to use but represent a certain attitude in 12 different ways that depend on the sequence of the rotation axes among three perpendicular axes. In addition, the time derivatives of Euler angles cannot represent every possible angular velocity of the rigid

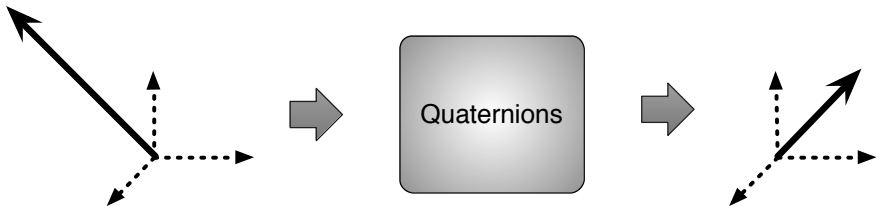

Figure 2.3: Quaternions possess information for the amount of rotation and scaling factor.

body because of *gimbal lock* [100], which caused an IMU failure during the Apollo 11 Moon mission [28]. Meanwhile, the Rodrigues parameters and the modified Rodrigues parameters, which form 3 parameters derived from unit quaternions ($\mathcal{S}^3 \mapsto \mathbb{R}^3$), are geometrically singular since they are not defined for π and 2π rotations. As a result, three parameter representations may be not suitable for continuous feedback control laws.

On the other hand, the four parameter representations such as unit quaternions ($\mathsf{SO(3)} \mapsto \mathcal{S}^3$) and the rotation axis-angle representation ($\mathsf{SO(3)} \mapsto \mathbb{R}^4$) do not possess singularities. For this reason, they are frequently used in practical applications to represent rigid body attitude. However, as shown in Table 2.1, the unit quaternion is defined globally but not uniquely from $\mathsf{SO(3)}$. In fact, they constitute a doubly covering space of $\mathsf{SO(3)}$ which needs to be taken into account in unit quaternion based feedback control laws. This distinct property as well as "extra effort" for feedback control laws are addressed in the following chapter. In this dissertation, we focus on unit quaternion parameterization to represent the attitude of spacecraft.

2.2.2 Unit Quaternion Algebra

The quaternions were first described by Irish mathematician William Rowan Hamilton in 1843 [29]. In his time, there was no concept of a mapping between two vector spaces as we refer now to a matrix algebra. Hamilton described quaternions as the quotient space of two directed lines in a three-dimensional space [30] or, equivalently, as the quotient space of two vectors. As shown in Fig. 2.3, quaternions hold information for rotation amount and scaling factor. The general form of a quaternion is defined as

$$\mathbf{q} = q_1 i + q_2 j + q_3 k + q_0, \tag{2.2}$$

where $q_1, q_2, q_3, q_0 \in \mathbb{R}$ and i, j, k denote three perpendicular complex axes, and q_0 denotes the real part of the quaternion. Quaternions have many analogies to ordinary complex numbers. In their multiplication, they follow the fundamental multiplication rules as

$$i^2 = j^2 = k^2 = ijk = -1, \tag{2.3}$$

$$ij = k,\ ji = -k,\ jk = i,\ kj = -i,\ ki = j,\ ik = -j. \tag{2.4}$$

These simple rules, the great breakthrough in quaternion algebra, finally came to Hamilton as he was walking along the towpath of the Royal Canal in Dublin with his wife on Monday October 16, 1843.

Observing from Eq. (2.4) that multiplications between complex axes i, j and k are sequence-dependent, we note that quaternion multiplication is non-commutative. In fact adopting the notation "$\otimes$" for quaternion multiplication, we have

$$\mathbf{q} \otimes \mathbf{p} = (q_1 i + q_2\, j + q_3\, k + q_0)(p_1\, i + p_2\, j + p_3\, k + p_0) \tag{2.5}$$

$$= (p_0 q_1 + p_1 q_0 - p_2 q_3 + p_3 q_2) i + (p_0 q_2 + p_1 q_3 + p_2 q_0 - p_3 q_1) j$$

$$+ (p_0 q_3 - p_1 q_2 + p_2 q_1 + p_3 q_0) k + (p_0 q_0 - p_1 q_1 - p_2 q_2 - p_3 q_3) \tag{2.6}$$

$$\neq \mathbf{p} \otimes \mathbf{q}. \tag{2.7}$$

Note that the (multiplicative) product of two quaternions is another quaternion. Thus the set of quaternions is *closed* under multiplication as well as under addition. Another important algebraic operation related to quaternions is the *complex conjugate* of a quaternion. We define the *complex conjugation* of the quaternion analogous to that of ordinary complex numbers, as

$$\mathbf{q}^* = -q_1 i - q_2 j - q_3 k + q_0. \tag{2.8}$$

Along with the quaternion product, the complex conjugate of the multiplicative product of quaternions is equal to the multiplicative product of the individual complex conjugates; namely,

$$(\mathbf{q} \otimes \mathbf{p})^* = \mathbf{p}^* \otimes \mathbf{q}^*. \tag{2.9}$$

As we can expect, many algebraic properties of complex numbers are valid with quaternions.

Let us now present a convenient notation for quaternions. Taking advantage of the expressiveness of matrix notation, we can take the vector form of a quaternion as

$$\mathbf{q} \stackrel{\text{def}}{=} \begin{bmatrix} q_1 & q_2 & q_3 & q_0 \end{bmatrix}^T = \begin{bmatrix} \boldsymbol{q}^T & q_0 \end{bmatrix}, \tag{2.10}$$

where $\boldsymbol{q} \in \mathbb{R}^3$ denotes the *vector part* of the quaternion and $q_0 \in \mathbb{R}$ denotes its *scalar part*. The subset of quaternion whose scalar part is zero is called *pure quaternions*, which are 3×1 vectors in the quaternion form.

Consider normalized quaternion where

$$\|\mathbf{q}\|_2 = 1. \tag{2.11}$$

The scaling factor then becomes an identity and the group of quaternions constitute the quotient space of two vectors, representing the rotational difference, which corresponds to a length preserving linear transformation, namely $\mathsf{SO}(3)$. This subset of quaternions is called the *unit quaternions*. Note that each corresponding unit quaternion is an element of a three dimensional unit sphere $\mathcal{S}^3$ embedded in $\mathbb{R}^4$ as

$$\mathcal{S}^3 = \{\, \mathbf{q} \in \mathbb{R}^4 \mid \|\mathbf{q}\|_2 = 1 \,\}. \tag{2.12}$$

The key idea result on how unit quaternions parameterize $\mathsf{SO}(3)$ is based on *Euler's rotation theorem* [50], which implies that any rotation or sequence of rotations of a rigid body in a three-dimensional space is equivalent to a pure rotation about a single fixed axis. Unit quaternions parameterize the pure rotational amount and rotation axis when we define the unit quaternion components as

$$\boldsymbol{q} = \widehat{\mathbf{n}} \sin\left(\frac{\theta}{2}\right) \in \mathbb{R}^3 \tag{2.13}$$

$$q_0 = \cos\left(\frac{\theta}{2}\right) \in \mathbb{R}, \tag{2.14}$$

where $\widehat{\mathbf{n}}$ and θ denote the Euler rotation axis and the rotation angle about this axis, respectively. Notice that the unit quaternion uses a half angle formula. This half angle form in fact is another breakthrough achieved by Hamilton. Since the unit quaternion is an extension of unit complex number, let us address how the half angle form was derived. It is

a well-known that the unit complex number parameterizes a rotation occurring in the two dimensional space, namely $\mathsf{SO}(2)$. In Fig. 2.4, the attitude of a' with respect to a can be parameterized by a unit complex number in the conventional notation as

$$a' = \cos\theta + \sin\theta\, i. \tag{2.15}$$

However, it technically cannot be said that this is a rotation in two dimensional space, because one axis is assigned to a complex axis i. On the other hand, we can consider a general rotation in $\mathbb{R}^2$, e.g., the $x-y$ plane in this case, about the complex axis i, as depicted in Fig. 2.5. The rotation amount of a' with respect to a is represented by a green colored vector in the figure. Numerically, we have

$$a' = \cos\frac{\theta}{2} + \sin\frac{\theta}{2} i, \text{ or } a' = \begin{bmatrix} \sin\frac{\theta}{2} \\ \cos\frac{\theta}{2} \end{bmatrix}_{2\times 1} \tag{2.16}$$

A unit quaternion, as the three dimensional extension of a unit complex number, parameterizes a rotating axis with three perpendicular imaginary axes i, j, and k; see Fig. 2.6. We now have a unit quaternion in a rotation angle and axis form as

$$\mathbf{q} = \begin{bmatrix} \mathbf{n}_x \sin\frac{\theta}{2} \\ \mathbf{n}_y \sin\frac{\theta}{2} \\ \mathbf{n}_z \sin\frac{\theta}{2} \\ \cos\frac{\theta}{2} \end{bmatrix}. \tag{2.17}$$

Quaternion Multiplication

Returning to the quaternion algebra using the matrix notation, we can find its multiplicative product in the following form as

$$\mathbf{q} \otimes \mathbf{p} = \begin{bmatrix} q_0\boldsymbol{p} + p_0\boldsymbol{q} + \boldsymbol{q} \times \boldsymbol{p} \\ q_0 p_0 - \boldsymbol{q}^T\boldsymbol{p} \end{bmatrix}, \tag{2.18}$$

where $\mathbf{q} = [\boldsymbol{q}^T,\ q_0]^T$ and $\mathbf{p} = [\boldsymbol{p}^T,\ p_0]^T$. Another quaternion operation is the "unit quaternion conjugation" given as $\mathbf{q}^* = [\,-\boldsymbol{q}^T\ q_0\,]^T$ in the vector notation, which facilitates

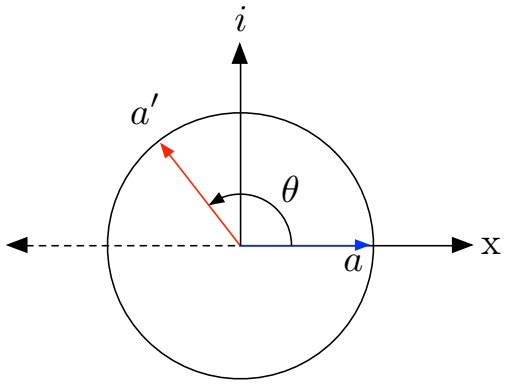

Figure 2.4: Unit complex parameterization for a rotation in two dimensional space in the conventional form.

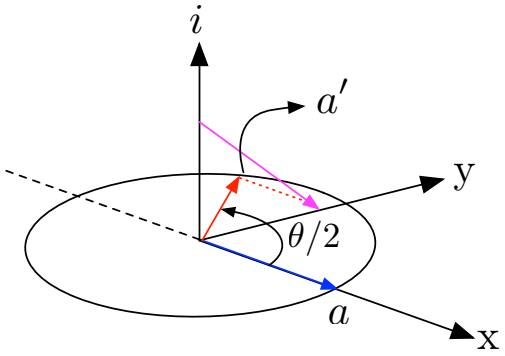

Figure 2.5: Unit complex parameterization for a rotation in two dimensional space with a half angle form.

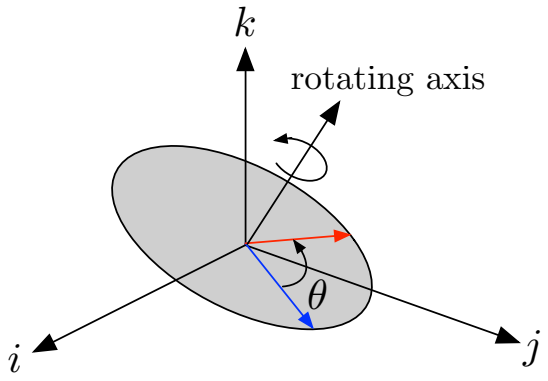

Figure 2.6: Unit quaternion parameterization for a rotation in three dimensional space with a half angle form.

the judicious definition of the "attitude difference/error" of $\mathbf{p}$ with respect to $\mathbf{q}$ as

$$\mathbf{q}_e \stackrel{\text{def}}{=} \mathbf{q}^* \otimes \mathbf{p} = \begin{bmatrix} q_0\boldsymbol{p} - p_0\boldsymbol{q} - \boldsymbol{q} \times \boldsymbol{p} \\ q_0 p_0 + \boldsymbol{q}^T\boldsymbol{p} \end{bmatrix}. \tag{2.19}$$

Note that the identity quaternion is expressed by $\mathbf{q_I} = [\,0\;0\;0\;1\,]^T$. Quaternion multiplication is analogous in many ways to vector cross products. Thus, the quaternion multiplcation can be expressed as the product of a skew symmetric matrix and a quaternion:

$$\mathbf{q} \otimes \mathbf{p} = [\mathbf{q}]_{\otimes}\,\mathbf{p} = \begin{bmatrix} [\boldsymbol{q}]_{\times} + q_0\mathbf{I_3} & \boldsymbol{q} \\ -\boldsymbol{q}^T & q_0 \end{bmatrix} \begin{bmatrix} \boldsymbol{p} \\ p_0 \end{bmatrix} \tag{2.20}$$

$$= [\mathbf{p}]^*_{\otimes}\,\mathbf{q} = \begin{bmatrix} [\boldsymbol{p}]^T_{\times} + p_0\mathbf{I_3} & \boldsymbol{p} \\ -\boldsymbol{p}^T & p_0 \end{bmatrix} \begin{bmatrix} \boldsymbol{q} \\ q_0 \end{bmatrix}, \tag{2.21}$$

where $[\mathbf{q}]_{\otimes}$ and $[\mathbf{p}]^*_{\otimes}$ denote 4×4 skew symmetric matrices related to "$\mathbf{q}$" and "$\mathbf{p}$", respectively; $[\boldsymbol{a}]_{\times}$ denotes a cross product operator associated with a vector $\boldsymbol{a}$ defined by

$$[\boldsymbol{a}]_{\times} = \begin{bmatrix} 0 & -a_3 & a_2 \\ a_3 & 0 & -a_1 \\ -a_2 & a_1 & 0 \end{bmatrix}. \tag{2.22}$$

When quaternions are represented as elements in $\mathbb{R}^4$, their algebraic properties are extended with vector-based products such as the inner product. The following are notable extended algebraic properties of quaternions:

$$\mathbf{a} \otimes (\mathbf{b} + \mathbf{c}) = \mathbf{a} \otimes \mathbf{b} + \mathbf{a} \otimes \mathbf{c} \tag{2.23}$$

$$(\mathbf{a} \otimes \mathbf{b})^* = \mathbf{b}^* \otimes \mathbf{a}^* \tag{2.24}$$

$$(\gamma\mathbf{a}) \otimes \mathbf{b} = \mathbf{a} \otimes (\gamma\mathbf{b}) = \gamma(\mathbf{a} \otimes \mathbf{b}) \tag{2.25}$$

$$\mathbf{a} \otimes (\mathbf{b} \otimes \mathbf{c}) = (\mathbf{a} \otimes \mathbf{b}) \otimes \mathbf{c} \tag{2.26}$$

$$\mathbf{a}^T(\mathbf{b} \otimes \mathbf{c}) = c^T(\mathbf{b}^* \otimes \mathbf{a}) = \mathbf{b}^T(\mathbf{a} \otimes \mathbf{c}^*), \tag{2.27}$$

where $\gamma \in \mathbb{R}$. Note that quaternions $\mathbf{a}, \mathbf{b}, \mathbf{c} \in \mathbb{R}^4$ and all properties are valid with unit quaternions since $\mathcal{S}^3 \in \mathbb{R}^4$. In particular, Eq. (2.27) is an interesting new identity. Now,

let us present another interesting algebraic properties only applicable to unit quaternions. This identity is inspired by the Binet-Cauchy identity [89].

Theorem 2.1 (Unit Quaternion Triple Identity)**.** *Assume that* $\mathbf{t}$ *and* $\mathbf{v}$ *are quaternions, and* $\mathbf{q}$ *is a unit quaternion. Then, for the vector inner product between two quaternion products, the following identity holds:*

$$(\mathbf{t} \otimes \mathbf{q})^T (\mathbf{y} \otimes \mathbf{q}) = (\mathbf{q} \otimes \mathbf{t})^T (\mathbf{q} \otimes \mathbf{y}) = \mathbf{t}^T \mathbf{y}, \tag{2.28}$$

where $\mathbf{t}, \mathbf{y} \in \mathbb{R}^4$ *and* $\mathbf{q} \in \mathcal{S}^3$.

Proof. The following proof utilizes the properties of quaternions. Using Eq. (2.27), we have

$$\begin{aligned}
(\mathbf{t} \otimes \mathbf{q})^T (\mathbf{y} \otimes \mathbf{q}) &= \mathbf{y}^T ((\mathbf{t} \otimes \mathbf{q}) \otimes \mathbf{q}^*) && (2.29)\\
&= \mathbf{y}^T (\mathbf{t} \otimes (\mathbf{q} \otimes \mathbf{q}^*)) && (2.30)\\
&= \mathbf{y}^T \mathbf{t}, && (2.31)
\end{aligned}$$

and

$$\begin{aligned}
(\mathbf{q} \otimes \mathbf{t})^T (\mathbf{q} \otimes \mathbf{y}) &= \mathbf{y}^T (\mathbf{q}^* \otimes (\mathbf{q} \otimes \mathbf{t})) && (2.32)\\
&= \mathbf{y}^T (\mathbf{q}^* \otimes \mathbf{q}) \otimes \mathbf{t}) && (2.33)\\
&= \mathbf{y}^T \mathbf{t}, && (2.34)
\end{aligned}$$

which concludes the proof. Note that this identity is still valid when $\mathbf{t}, \mathbf{y}$ are pure quaternions, namely, when $\mathbf{t} = [\, \boldsymbol{t}^T \; 0 \,]$, $\mathbf{v} = [\, \boldsymbol{v}^T \; 0 \,]$ with $\boldsymbol{t}, \boldsymbol{v} \in \mathbb{R}^3$. □

Quaternion Rotation Operator

Given the attitude $\mathbf{q}$, the position vector $\boldsymbol{t}_b$ in body frame $\mathcal{B}$ can be represented in the inertial frame $\mathcal{O}$ as

$$\mathbf{t}_o = L_q(\boldsymbol{t}_b) = \mathbf{q} \otimes \mathbf{t}_b \otimes \mathbf{q}^*, \tag{2.35}$$

where $\boldsymbol{t}_o$ denotes the same vector expressed in the inertial frame $\mathcal{O}$. Note that $\mathbf{t}_b$ and $\mathbf{t}_o$ are in the form of pure quaternions from $\boldsymbol{t}_b, \boldsymbol{t}_o \in \mathbb{R}^3$. Conversely, the position vector $\boldsymbol{t}_o$ can be

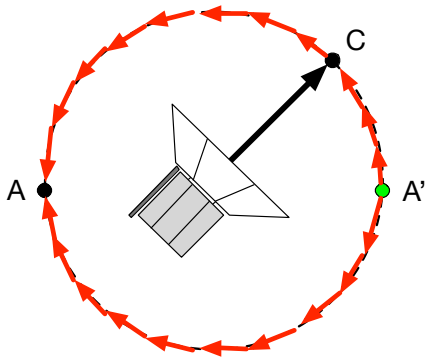

Figure 2.7: Illustration of the impossibility of global stabilization for planar rotation using continuous time-invariant feedback control.

represented with respect to the body frame $\mathcal{B}$ as

$$\mathbf{t}_b = L_q^{-1}(\boldsymbol{t}_o) = \mathbf{q}^* \otimes \mathbf{t}_o \otimes \mathbf{q}. \tag{2.36}$$

We note here that Eq. (2.35) is also interpreted as a "rotation $\mathbf{q}$ of the vector $\boldsymbol{y}$" when assuming two frames are aligned initially, whereas Eq. (2.36) is a "rotation $\mathbf{q}$ of the body frame $\mathcal{B}$" as the unit quaternion $\mathbf{q}$ represents how much the body frame $\mathcal{B}$ has rotated from the inertial frame $\mathcal{O}$.

2.3 Notion of Almost Global Stability

The rigid body attitude configuration space $\mathsf{SO(3)}$ is a boundary-less compact manifold which is not diffeomorphic to any vector space. This simple fact leads to the *impossibility of global attitude stabilization* using continuous time-invariant feedback control [7, 45]. To understand this issue, consider a single degree of freedom rotation of rigid body about a fixed axis, namely the rotational configuration on the unit circle $\mathcal{S}^1$ as depicted in Fig. 2.7. This one dimensional rotation is helpful for understanding the analogous results when attitude configurations are in $\mathsf{SO(3)}$ or $\mathcal{S}^3$. We design a control law to stabilize the orientation of the spacecraft, represented by the black arrow from point C to point A in the attitude configuration of $\mathcal{S}^1$, by applying a force at the tip of the black arrow which is tangent to the configuration space. The control action is governed by the development of a

Representations	Stable Equilibrium	Unstable Equilibria
Rotation Matrix $\mathsf{SO}(3) \times \mathbb{R}^3$	$\begin{bmatrix} 1 & 0 & 0 \\ 0 & 1 & 0 \\ 0 & 0 & 1 \end{bmatrix}$	$\begin{bmatrix} 1 & 0 & 0 \\ 0 & -1 & 0 \\ 0 & 0 & -1 \end{bmatrix}, \begin{bmatrix} -1 & 0 & 0 \\ 0 & -1 & 0 \\ 0 & 0 & 1 \end{bmatrix}, \begin{bmatrix} -1 & 0 & 0 \\ 0 & 1 & 0 \\ 0 & 0 & -1 \end{bmatrix}$
Unit quaternion $\mathcal{S}^3 \times \mathbb{R}^3$	$\begin{bmatrix} 0 \\ 0 \\ 0 \\ 1 \end{bmatrix}$	$\begin{bmatrix} 0 \\ 0 \\ 0 \\ -1 \end{bmatrix}$

Table 2.2: Stable and unstable equilibria corresponding to the continuous feedback control law using the rotation matrix and unit quaternion.

continuous vector field that rotates the orientation to point A. However, if we attempt to construct a continuous vector field around point A, then an additional equilibrium point A' is created naturally. This is because the rotational configuration space is a boundary-less closed manifold which results in the fact that the force vector fields are non-vanishing and acting in opposing direction following the upper half and lower half of the circle in Fig. 2.7. Since the control law is continuous, it must vanish at some point, thereby creating a second equilibrium A' in addition to A. We note that additionally created equilibria are unstable as we can easily see from Fig. 2.7.

In the case of full attitude stabilization, the continuous control law analogously creates three additional unstable equilibria in $\mathsf{SO}(3) \times \mathbb{R}^3$ along with a stable equilibrium when combined with the attitude dynamics that evolve on $\mathbb{R}^3$. The unit quaternion, parameterizing $\mathsf{SO}(3)$ globally, can also have continuous feedback control over its entire domain. Interestingly, it produces only one additional equilibrium; see Table 2.2. We further address this issue with unit quaternions in the following section.

With the knowledge of the existence of extra unstable equilibria, the objective of globally asymptotic stability then has to be relaxed. Many researchers settle for *almost* globally

asymptotic stability on such topologically complex manifolds. In fact, the "almost global" terminology originates in the spacecraft attitude literature, which has used this term to mean asymptotic stability over an open and dense set in $\mathsf{SO(3)}$ [4, 90], the literature adopted the terminology to refer to the case where feedback control stabilizes all situations, excluding those starting in a nowhere dense set. A nowhere dense set is considered thin and negligible in a topological sense. In practical applications, this relaxation is still reasonable since disturbances and noise will prevent the system from falling into a nowhere dense set [5, 65].

2.4 Unwinding Phenomenon and its Remedy

Unit quaternion-based attitude control laws have received particular attention in the recent decade [1,43,56,72,103] since the unit quaternion is the minimal globally singular-free representation of a rigid body's attitude. However, unit quaternions double cover the rotational configuration space $\mathsf{SO(3)}$ in the sense that each attitude corresponds to two distinct unit quaternions. This can be observed from the map $R : \mathbf{q} \in \mathcal{S}^3 \to \mathsf{SO(3)}$ defined as

$$R(\mathbf{q}) = I_3 + 2q_0[\boldsymbol{q}]_\times + 2[\boldsymbol{q}]_\times^2, \tag{2.37}$$

where $[\boldsymbol{q}]_\times$ denotes the cross product operator associated with the vector part of the unit quaternion as

$$[\boldsymbol{q}]_\times = \begin{bmatrix} 0 & -q_3 & q_2 \\ q_3 & 0 & -q_1 \\ -q_2 & q_1 & 0 \end{bmatrix}, \text{ with } \mathbf{q} = \begin{bmatrix} \boldsymbol{q} \\ q_0 \end{bmatrix}. \tag{2.38}$$

Note that in continuous feedback control, this property combined with the existence of the extra unstable equilibrium of $-\mathbf{q}$, is referred to as the *unwinding phenomenon* [7]. Briefly speaking, continuous time-invariant feedback control using unit quaternions can give rise to regions of attraction and repulsion in the neighborhood of $\mathbf{q}$ and $-\mathbf{q}$, respectively, where $\mathbf{q}$ and $-\mathbf{q}$ represent the same desired attitude in $\mathsf{SO(3)}$. To understand this phenomena, consider an attitude reorientation trajectory from $\mathbf{q}$ to $-\mathbf{q}$ in the unit quaternion space. We can choose an initial angular velocity such that a trajectory connecting these regions of repulsion and attraction arise. This trajectory connects the vicinity of $\mathbf{q}$ to the vicinity of $-\mathbf{q}$

in $\mathcal{S}^3$, with a terminal velocity that is close to zero. The corresponding actual trajectory in $\mathsf{SO(3)}$ starts and ends close to the desired attitude corresponding to $\mathbf{q}$. However, in the quaternion space, since $-\mathbf{q}$ has a region of repulsion, the trajectory is repelled from $-\mathbf{q}$ yielding an unwinding rotation close to 2π, then converging to $-\mathbf{q}$. Therefore, unit quaternion based control law may be said to be locally asymptotically stable or almost globally stable without having asymptotic stability. The presence of unwinding motion prevents the global asymptotic stability in the sense of Lyapunov.

Here we present a simple remedy against the unwinding phenomenon for a set point control. The key idea to avoid an undesired unwinding phenomenon is to use a metric which can capture the geodesic distance in S^3 as a Euclidean distance between the current orientation and desired orientation. This is a straightforward result as the arc length (geodesic rotation) between two points on the unit sphere is proportional to the chord length between these points, as shown in Fig. 2.8. Therefore, given the current attitude $\mathbf{p}$ and the desired attitude $\mathbf{q}$, we find the desired attitude between $\mathbf{q}$ and $-\mathbf{q}$ depending on the choice that yields the smaller chord length, namely between

$$\| \mathbf{p} - \mathbf{q} \| \quad \text{and} \quad \| \mathbf{p} + \mathbf{q} \|. \tag{2.39}$$

In Fig. 2.8, we observe that $\mathbf{q}$ has a shorter Euclidean distance from $\mathbf{p}$ on $\mathcal{S}^3$ as compared with $-\mathbf{q}$. This chordal approach is subsequently used in our discussion on the spacecraft reorientation in the presence of attitude constrained zones.

We note that the fact that unit quaternions can represent attitude error in two distinct ways such that one is geodesic and the other is non-geodesic, is not always a disadvantage; see Fig. 2.9. This is in light of the fact that rotation matrices can not distinctly represent rotations $\theta < -\pi$ and $\theta \geq \pi$. For example, the rotation $\frac{3}{2}\pi$ represented by R is identical to the rotation $-\frac{1}{2}\pi$ about the same axis, i.e.,

$$R\Big(\frac{3}{2}\pi, \boldsymbol{n}\Big) = R\Big(-\frac{1}{2}\pi, \boldsymbol{n}\Big), \tag{2.40}$$

where $\boldsymbol{n}$ denotes the rotation axis. This observation can be important when a non-geodesic rotation is required for space science mission. For example, a space telescope reorientation while keeping the antenna's boresight pointed toward the ground station may not be available when a wide rotationally constrained zone is positioned in the middle of the geodesic

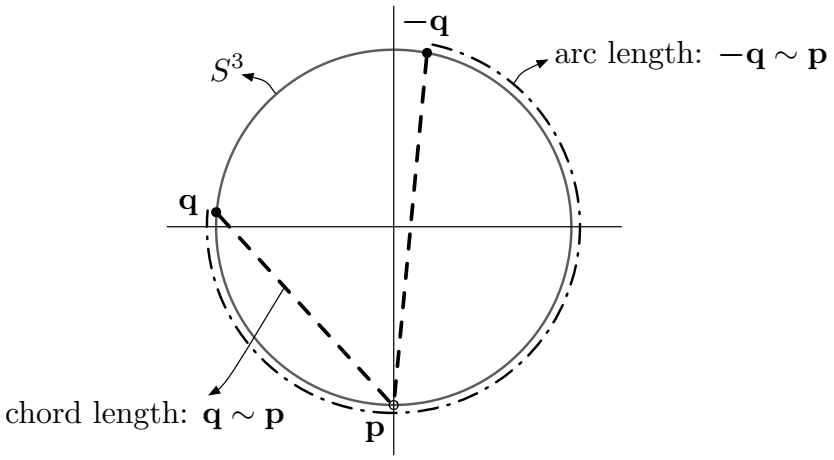

Figure 2.8: Chord length can be used to determine which arc length is geodesic. In this example, $\| \mathbf{p} - \mathbf{q} \|$ is shorter than $\| \mathbf{p} + \mathbf{q} \|$.

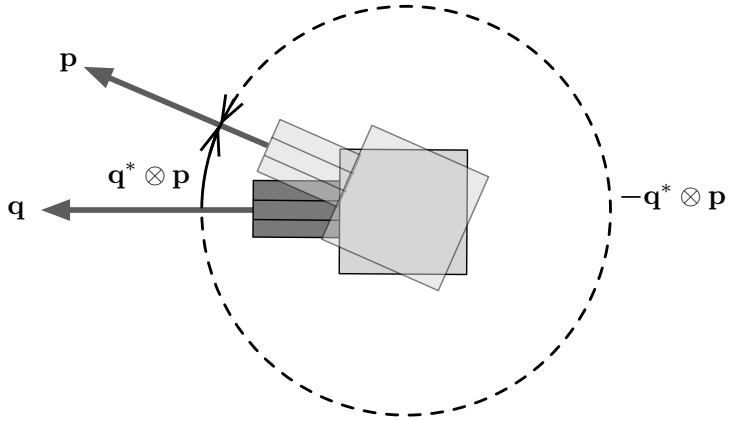

Figure 2.9: Attitude difference/error of $\mathbf{p}$ with respect to $\mathbf{q}$ and with respect to $-\mathbf{q}$. In this example, $\mathbf{q}^\star \otimes \mathbf{p}$ exhibits a geodesic rotation error over $-\mathbf{q}^\star \otimes \mathbf{p}$

rotation trajectory. We treat a more extreme case of this scenario to evaluate the effectiveness, and demonstrate the viability of the proposed algorithm in Chapter 3.

Chapter 3

ROTATIONALLY CONSTRAINED RIGID BODY CONTROL

The execution of large angle reorientation of spacecraft while avoiding pointing onboard instruments to certain celestial objects is one of the challenging but critical technologies for spacecraft autonomy. In this chapter, we consider the spacecraft reorientation control problem in the presence of rotationally constrained zones. Planning such a reorientation poses a challenging computational task for the spacecraft guidance, navigation, and control subsystem. The fundamental complexity of such problems is mainly due to the fact that the rotational configuration space, $\mathsf{SO}(3)$ is a boundary-less compact manifold and removing the constrained zones from $\mathsf{SO}(3)$ results in a *non-convex* region.

3.1 Literature Reviews

The attitude reorientation problem in the presence of attitude constrained zones has been examined in only a few research works. For example, McInnes considered and implemented maneuver planning in the presence of attitude constrained zones via an artificial potential function in [61–63]. However, due to the use of Euler angles in McInnes' works, the possibility of having singularities during reorientation maneuvers could not be ruled out. Another set of approaches to constrained attitude control which rely on geometric relations between the direction of an instrument's bore-sight and the bright celestial object to be avoided, has been introduced by Spindler [94], Hablani [25], and Frakes *et al.* [55]. In these research works, a feasible attitude trajectory is determined prior to the reorientation maneuver and

generated based on the geometric relations with exclusion zones. These approaches have a disadvantage of not being extendible to more complex situations, those involving multiple celestial constrained zones, as often encountered in actual space missions. Over the last decade, alternative approaches using randomized algorithms have also been proposed by Frazzoli *et al.* [46], Kornfeld [47], and Cui *et al.* [12]. The randomization-based approaches have an advantage in terms of their ability to handle distinct classes of constraints, with provable–albeit probabilistic–convergence properties. The randomized algorithms, however, have limitations in terms of their on-board implementation and might result in execution times that, depending on the types of constrained zones and initial and final attitudes, can be of exponential order. Recently, Koenig [42] proposed an algorithm which alters the boresight pointing direction, rotating it by some angle in normal direction to that of the rate command, and Kjellberg and Lightsey [51] presented a discretized pathfinding algorithm through the pixelization of the configuration space.

In the meantime, Kim and Mesbahi [26, 64] proposed the quaternion-based convex attitude constraint parameterization which builds on the constraint set representation discussed in [105]. In this paper, we expand upon the results of [26, 64] to propose a potential function based approach to constrained attitude control over more general constrained sets. The advantage of the proposed approach hinges upon the fact that the logarithmic barrier potential used for constructing the corresponding control law is smooth and strictly convex. This in turn implies that the proposed methodology can simultaneously handle a large number of forbidden and mandatory zones, while guaranteeing computational tractability and guaranteed convergence. Subsequently, two types of feedback control laws for constrained reorientation problems are derived in this paper. These feedback controllers will be referred to as model independent and model dependent. In this direction, the model independent control law is first derived from an energy-based Lyapunov function. The model dependent control law, on the other hand, is obtained by the modified backstepping method. The backstepping method has been favored by a number of researchers due to the cascade structure of the attitude dynamics. In this paper, we adopt the modified backstepping method introduced in [41] in order to avoid excessive control torque commands during the initial phase of the reorientation maneuver.

3.2 Constrained Zone Formulation in Unit Quaternion

In this section, we define three types of attitude constrained zones that will be the focus of the current chapter in this dissertation:

- **Attitude Forbidden Zone** : A set of spacecraft orientations, such as the set of attitudes that lead the sensitive on-board instruments to have a direct exposure to certain celestial objects, e.g., the sun, is considered as an attitude forbidden zone. Multiple constrained zones can be specified with respect to a single instrument bore-sight vector.

- **Attitude Mandatory Zone** : A set of spacecraft orientations, such as the set of attitudes that lead certain on-board instruments to point toward specified objects, e.g., pointing a high gain antenna to a ground station, is considered as an attitude mandatory zone. The attitude mandatory zones for each instrument should be non-conflicting.

- **Attitude Permissible Zone** : A set of spacecraft orientations is considered to be in the attitude permissible zone when it is at the intersection of the complements of attitude forbidden zones on one hand, and the attitude mandatory zones, on the other.

Proposition 3.1. *[83, 105] Suppose that an angle* ***strictly greater*** *than θ should be maintained between the normalized bore-sight vector y of the spacecraft instrument and the normalized vector x pointing toward a certain celestial object, as shown in Fig. 3.1. This requirement can be expressed as*

$$\boldsymbol{x} \cdot \boldsymbol{y}' < \cos\theta, \tag{3.1}$$

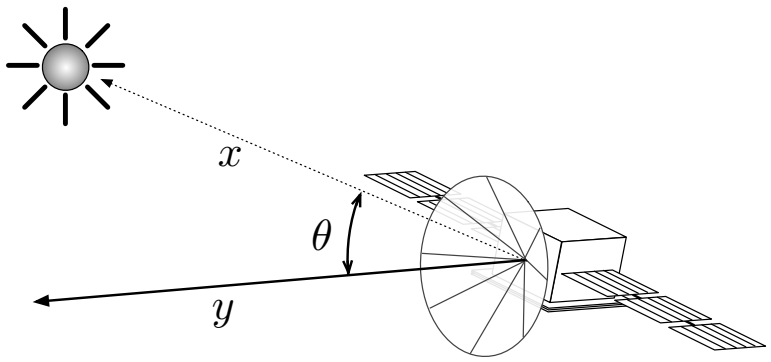

Figure 3.1: Maintaining a minimum angle of θ between the bore-sight vector y in the body frame and the inertial vector x

where

$$\begin{aligned}
\boldsymbol{y}' &= \mathbf{q} \otimes \boldsymbol{y} \otimes \mathbf{q}^* \\
&= \begin{bmatrix} \boldsymbol{q} \\ q_0 \end{bmatrix} \otimes \begin{bmatrix} \boldsymbol{y} \\ 0 \end{bmatrix} \otimes \begin{bmatrix} -\boldsymbol{q} \\ q_0 \end{bmatrix} && (3.2) \\
&= \begin{bmatrix} q_0^2\boldsymbol{y} + 2q_0(\boldsymbol{q} \times \boldsymbol{y}) + (\boldsymbol{q}^T\boldsymbol{y})\boldsymbol{q} - (\boldsymbol{q} \times \boldsymbol{y}) \times \boldsymbol{q} \\ -q_0\boldsymbol{q}^T\boldsymbol{y} + q_0\boldsymbol{y}^T\boldsymbol{q} + (\boldsymbol{q} \times \boldsymbol{y})^T\boldsymbol{q} \end{bmatrix} && (3.3) \\
&= \boldsymbol{y} - 2(\boldsymbol{q}^T\boldsymbol{q})\boldsymbol{y} + 2(\boldsymbol{q}^T\boldsymbol{y})\boldsymbol{q} - 2q_0(\boldsymbol{y} \times \boldsymbol{q}) && (3.4)
\end{aligned}$$

denotes the instrument's bore-sight vector represented in the inertial frame, taking into account the spacecraft attitude $\mathbf{q}$*. Note that the position vector* $\boldsymbol{x}$ *is represented in the inertial frame. Combining Eqs. (3.1), (3.4) yields*

$$2\boldsymbol{q}^T\boldsymbol{y}\boldsymbol{q}^T\boldsymbol{x} - \boldsymbol{q}^T\boldsymbol{q}\boldsymbol{x}^T\boldsymbol{y} + q_0^2\boldsymbol{x}^T\boldsymbol{y} - 2q_0\boldsymbol{q}^T(\boldsymbol{x} \times \boldsymbol{y}) < \cos\theta. \tag{3.5}$$

After some algebraic manipulations, we obtain

$$\mathbf{q}^T \begin{bmatrix} A & b \\ b^T & d \end{bmatrix} \mathbf{q} < 0, \tag{3.6}$$

where

$$A = \boldsymbol{x}\boldsymbol{y}^T + \boldsymbol{y}\boldsymbol{x}^T - (\boldsymbol{x}^T\boldsymbol{y} + \cos\theta)\,\mathbf{I}_3,$$
$$b = -\boldsymbol{x} \times \boldsymbol{y}, \qquad d = \boldsymbol{x}^T\boldsymbol{y} - \cos\theta. \tag{3.7}$$

Such a representation, on the other hand, enables the parameterization of the three aforementioned constrained zones into the form of quadratic inequalities, as we proceed to show below.

Complement of Attitude Forbidden Zones

Let the unit quaternion $\mathbf{q} \in \mathcal{S}^3$ describe the attitude of the spacecraft whose bore-sight vector $\boldsymbol{y}_j$ for the jth instrument, e.g., a telescope, lies *outside of the attitude forbidden zone*, i.e., $\beta_2 > \theta_2$ in Fig. 3.2. Then the subset $\mathbf{q}_{\boldsymbol{F}_i^j} \subseteq \mathcal{S}^3$ satisfying the above condition can be represented as,

$$\mathbf{q}_{\boldsymbol{F}_i^j} = \{\, \mathbf{q} \in \mathcal{S}^3 \mid \mathbf{q}^T M_i^j(\theta_i^j)\mathbf{q} < 0\}, \tag{3.8}$$

with

$$M_i^j(\theta_i^j) = \begin{bmatrix} A_i^j & b_i^j \\ b_i^{jT} & d_i^j \end{bmatrix}, \tag{3.9}$$

where

$$A_i^j = \boldsymbol{x}_i\boldsymbol{y}_j^T + \boldsymbol{y}_j\boldsymbol{x}_i^T - (\boldsymbol{x}_i^T\boldsymbol{y}_j + \cos\theta_i^j)\,\mathbf{I}_3, \tag{3.10}$$
$$b_i^j = -\boldsymbol{x}_i \times \boldsymbol{y}_j, \qquad d_i^j = \boldsymbol{x}_i^T\boldsymbol{y}_j - \cos\theta_i^j, \tag{3.11}$$
$$i = 1, 2, \ldots, n, \quad j = 1, 2, \ldots, m.$$

Let us elaborate on the notation used above. The index i represents the number of constrained objects associated with the jth on-board instrument; the index j on the other hand, is the number of instruments. Thus M_i^j corresponds to the ith celestial object and the jth instrument, i.e., $\boldsymbol{x}_i$, $\boldsymbol{y}_j$. Moreover, $\boldsymbol{x}_i$ denotes the unit vector (specified in the inertial frame) for the ith constrained object to be avoided, while $\boldsymbol{y}_j$ indicates the unit vector (in the body frame) representing the bore-sight direction of the jth sensitive instrument on

the spacecraft. The angle θ_i^j is the constraint angle about the direction of the ith object specified by $\boldsymbol{x}_i$ for the jth instrument bore-sight vector $\boldsymbol{y}_j$. Without loss of generality, the domain of the angle θ_i^j, for all i, j, is restricted to be $(0, \pi)$. We note that an attitude forbidden zone with $\theta_i^j \geq \frac{1}{2}\pi$ represents the same attitude constrained zone on the celestial sphere as *the attitude mandatory zone* with an angle $\pi - \theta_i^j$. The attitude forbidden zone is generally defined not only with respect to the number of onboard sensitive instruments m, but also with respect to the number of constraint objects n.

Attitude Mandatory Zone

The set $\mathbf{q_M} \subseteq \mathcal{S}^3$ representing possible attitudes of the spacecraft on which the bore-sight vector of an on-board instrument, e.g., an antenna, lies inside the attitude mandatory zone, i.e., $\beta_M < \theta_M$ in Fig. 3.3. This set can be represented as,

$$\mathbf{q_M} = \{\, \mathbf{q} \in \mathcal{S}^3 \mid \mathbf{q}^T M_M(\theta_M)\mathbf{q} > 0 \,\}, \tag{3.12}$$

where $M_M(\theta_M)$ and θ_M are defined analogous to Eq. (3.9), with respect to the bore-sight vector of an on-board instrument, which should stay in the attitude mandatory zone. The angle θ_M in Eq. (3.12) is the constraint angle for the attitude mandatory zone about the direction of the object specified by $\boldsymbol{x}_1$ in Fig. 3.3. Note that we have considered the case where only one attitude mandatory zone is present; this is without loss of generality, as if multiple mandatory zones are present, only the set defined by their intersection can be considered.

Attitude Permissible Zone

Let us now provide a representation for the Attitude Permissible Zone. The subset $\mathbf{q_p}$, parameterizing the attitude of the spacecraft satisfying the attitude mandatory zones, as well as avoiding the attitude forbidden zones, is given by,

$$\mathbf{q_p} = \{\mathbf{q} \in \mathcal{S}^3 \mid \mathbf{q} \in \mathbf{q}_{\boldsymbol{F_i^j}} \text{ and } \mathbf{q} \in \mathbf{q_M}\}, \tag{3.13}$$
$$i = 1, 2, \ldots, n,\ j = 1, 2, \ldots, m.$$

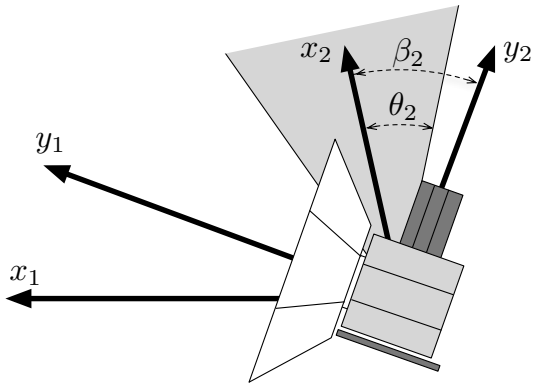

Figure 3.2: The complement of attitude forbidden zone associated with an instrument bore-sight vector $\boldsymbol{y}_2$.

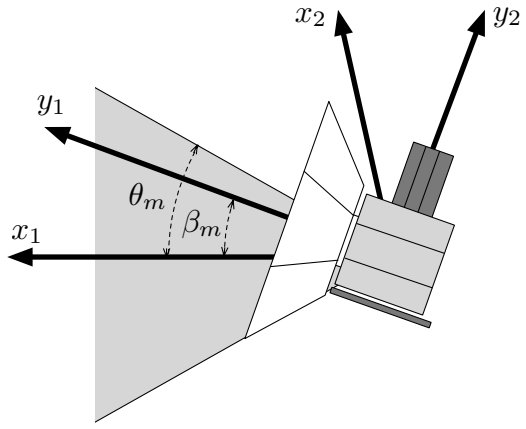

Figure 3.3: An attitude mandatory zone associated with an instrument bore-sight vector $\boldsymbol{y}_1$.

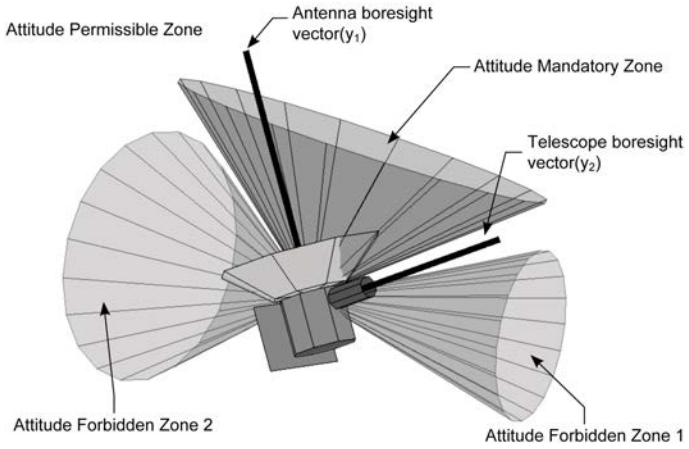

Figure 3.4: Three types of constrained zones shown on the celestial space. Attitude Mandatory zone is associated with an antenna bore-sight vector y_1 while a telescope bore-sight vector y_2 is associated with Attitude Forbidden zone 1 and 2.

Fig. 3.4 depicts three types of attitude constrained zones shown on the celestial sphere, defined with respect to two instrument bore-sight vectors $\boldsymbol{y}_1$ and $\boldsymbol{y}_2$.

3.3 Convexification of Attitude Constrained Zones

We now consider the problem of designing feedback control laws of the form $u = f(\mathbf{q}, \boldsymbol{\omega})$, such that $\mathbf{q} \to \mathbf{q}_d$ and $\boldsymbol{\omega} \to \mathbf{0}$, where $\mathbf{q}_d$ denotes the desired attitude, while guaranteeing that $\mathbf{q}(t) \in \mathbf{q}_{\boldsymbol{p}}$, for all $t \geq 0$, where $\mathbf{q}_{\boldsymbol{p}}$ denotes the *Attitude Permissible Zone*.

We first provide the necessary observations that will be subsequently used for the convex parameterization of the forbidden and mandatory zones and their respective embedding in a *potential function*.

Proposition 3.2. *Let $M(\theta)$ be the matrix used in the representation of the complement of attitude forbidden zones in Eq. (3.9). Then for $\theta \in (0, \pi)$, one has*

$$-2 < \lambda_{\min}(M) \leq \mathbf{q}^T M \mathbf{q} \leq \lambda_{\max}(M) < 2. \tag{3.14}$$

Proof. From Eq. (3.9), the symmetric matrix $M(\theta)$ can be written as

$$M(\theta) = P(\theta) - \cos\theta \mathbf{I}_4 \tag{3.15}$$

where

$$P(\theta) = \begin{bmatrix} \boldsymbol{x}\boldsymbol{y}^T + \boldsymbol{y}\boldsymbol{x}^T - (\boldsymbol{x}^T\boldsymbol{y})\mathbf{I}_3 & \boldsymbol{x} \times \boldsymbol{y} \\ (\boldsymbol{y} \times \boldsymbol{x})^T & \boldsymbol{x}^T\boldsymbol{y} \end{bmatrix}. \tag{3.16}$$

Since vectors $\boldsymbol{x}$ and $\boldsymbol{y}$ are unit vectors, $P^T P = \mathbf{I}_4$. Thus,

$$\begin{aligned} P\boldsymbol{v} &= \lambda_p \boldsymbol{v} \\ P^T P\boldsymbol{v} &= \lambda_p P\boldsymbol{v}, \\ \left(\mathbf{I}_4 - \lambda_p^2\right)\boldsymbol{v} &= 0, \end{aligned}$$

where λ_p is an eigenvalue of P, and $\boldsymbol{v}$ is the corresponding eigenvector. The eigenvalues of P, on the other hand, are

$$\lambda_p = -1,\ -1,\ 1,\ 1. \tag{3.17}$$

Note that from Eq. (3.15), eigenvalues of the matrix $M(\theta)$ are shifted from λ_p by $\cos\theta$, which assumes values between -1 and 1. Therefore, in view of the fact that $\|\mathbf{q}(t)\| = 1$, Eq. (3.14) follows. □

Proposition 3.3. *Let $M_i^j(\theta_i^j)$ be the matrix employed to represent the complement of attitude forbidden zones in Eq. (3.9). Consider the quaternion subset $\mathbf{q}_{\boldsymbol{F}_i^j} \subseteq \mathcal{S}^3$ defined in Eq. (3.8) specified as*

$$\mathbf{q}_{\boldsymbol{F}_i^j} = \{\, \mathbf{q} \in \mathcal{S}^3 \mid \mathbf{q}^T M_i^j(\theta_i^j)\mathbf{q} < 0 \,\}. \tag{3.18}$$

Then this set can be represented as a convex set

$$\mathbf{q}'_{\boldsymbol{F}_i^j} = \{\, \mathbf{q} \in \mathcal{S}^3 \mid \mathbf{q}^T \tilde{M}_i^j(\theta_i^j)\mathbf{q} < 2 \,\}, \tag{3.19}$$

where $\tilde{M}_i^j(\theta) \in \mathbb{S}_{++}^4$.

Proof. The proof is inspired by an analogous argument presented in [64]. From Eq. (3.14)

in Proposition 3.2, it follows that

$$\begin{aligned}
-2 < \lambda_{\min}(M_i^j(\theta_i^j)) \leq \mathbf{q}^T M_i^j(\theta_i^j)\mathbf{q} < 0,\\
-2 < \lambda_{\min}(M_i^j(\theta_i^j)) + 2 \leq \mathbf{q}^T M_i^j(\theta_i^j)\mathbf{q} + 2 < 2,\\
-2 < \lambda_{\min}(M_i^j(\theta_i^j)) + 2 \leq \mathbf{q}^T M_i^j(\theta_i^j)\mathbf{q} + 2\mathbf{q}^T\mathbf{q} < 2,\\
-2 < \lambda_{\min}(M_i^j(\theta_i^j)) + 2 \leq \mathbf{q}^T (M_i^j(\theta_i^j) + 2\mathbf{I}_4)\mathbf{q} < 2,\\
0 < \lambda_{\min}(M_i^j(\theta_i^j)) + 2 \leq \mathbf{q}^T \tilde{M}_i^j(\theta_i^j)\mathbf{q} < 2,\\
0 < \mathbf{q}^T \tilde{M}_i^j(\theta_i^j)\mathbf{q} < 2,
\end{aligned}$$

where $\mathbf{q}^T\mathbf{q} = 1$ and $\tilde{M}_i^j(\theta_i^j) \in \mathbb{S}^4_{++}$. Therefore the subsets $\mathbf{q}_{\boldsymbol{F_i^j}}$ and $\mathbf{q}'_{\boldsymbol{F_i^j}}$ above represent the same convex set. □

Proposition 3.4. *Analogous to Proposition 3.3, let $M_M(\theta) \in \mathbb{S}^4$ be the matrix in the representation (3.12). Then the subset $\mathbf{q}_{\boldsymbol{M}} \subseteq \mathcal{S}^3$ specifying the Attitude Mandatory Zone,*

$$\mathbf{q}_{\boldsymbol{M}} = \{\, \mathbf{q} \in \mathcal{S}^3 \mid 0 < \mathbf{q}^T M_M(\theta)\mathbf{q} \,\} \tag{3.20}$$

can be represented as a convex set

$$\mathbf{q}'_{\boldsymbol{M}} = \{\, \mathbf{q} \in \mathcal{S}^3 \mid \mathbf{q}^T \tilde{M}_M(\theta)\mathbf{q} < 2 \,\}, \tag{3.21}$$

where $\tilde{M}_M(\theta) \in \mathbb{S}^4_{++}$.

Proof. The proof follows by observing the following inequalities,

$$\begin{aligned}
0 < \mathbf{q}^T M_M(\theta)\mathbf{q} \leq \lambda_{\max}(M(\theta)) < 2\\
-2 < \mathbf{q}^T M_M(\theta)\mathbf{q} - 2 \leq \lambda_{\max}(M(\theta)) - 2 < 2,\\
-2 < -\mathbf{q}^T \tilde{M}_M(\theta)\mathbf{q} \leq \lambda_{\max}(M(\theta)) - 2 < 0,\\
0 < -\lambda_{\max}(M(\theta)) + 2 \leq \mathbf{q}^T \tilde{M}_M(\theta)\mathbf{q} < 2,
\end{aligned}$$

where $\mathbf{q}^T\mathbf{q} = 1$ and $\tilde{M}_M \in \mathbb{S}^4_{++}$. Hence, the two subsets $\mathbf{q}_{\boldsymbol{M}}$ and $\mathbf{q}'_{\boldsymbol{M}}$ above represent the same convex set. □

3.4 Convex Log Barrier Potential

The unit quaternion is globally non-singular in representing an attitude on $\mathsf{SO(3)}$. The potential function

$$V_I : \mathcal{S}^3 \to \mathbb{R}_+$$

for attitude tracking to the desired attitude $\mathbf{q}_d$, can be defined as

$$V_I = \| \mathbf{q}_d^* \otimes \mathbf{q} \pm \mathbf{q}_\mathrm{I} \|^2, \tag{3.22}$$

which can be made to be a *Lyapunov function* about $\mathbf{q}_d$ along the rigid body kinematics, leading to a stabilizing control law.

Proposition 3.5. *The following two norm squares are identical:*

$$\| \mathbf{q}_d^* \otimes \mathbf{q} \pm \mathbf{q}_\mathrm{I} \|^2 = \| \mathbf{q}_d \pm \mathbf{q} \|^2. \tag{3.23}$$

where $\mathbf{q}_d$ denotes a desired attitude

Proof. The proof follows by utilizing the properties of unit quaternions as

$$\begin{aligned} \| \mathbf{q}_d^* \otimes \mathbf{q} \pm \mathbf{q}_\mathrm{I} \|^2 &= 2 \pm 2\mathbf{q}_\mathrm{I}^T(\mathbf{q}_d^* \otimes \mathbf{q}) \\ &= 2 \pm 2\mathbf{q}_d^T\mathbf{q} \\ &= \mathbf{q}_d^T\mathbf{q}_d + \mathbf{q}^T\mathbf{q} \pm 2\mathbf{q}_d^T\mathbf{q} \\ &= \| \mathbf{q}_d \pm \mathbf{q} \|^2, \end{aligned}$$

which employs the identity $(\mathbf{q}_d^* \otimes \mathbf{q})^T(\mathbf{q}_d^* \otimes \mathbf{q}) = 1$. □

A direct consequence of Proposition 3.5 is that the function V_I (3.22) defines a quaternion error potential function with respect to the desired quaternion. As we discussed in §2.4, the unit quaternion inherently possesses a sign ambiguity; for example, $\frac{1}{2}\pi$ rotation and $-\frac{3}{2}\pi$ rotation about the same eigen-axis geometrically represent the same attitude on $\mathsf{SO(3)}$, but correspond to two distinct unit quaternions, say $\mathbf{q}$ and $-\mathbf{q}$. This ambiguity leads to having two choices for a *desired* quaternion in the potential function in V_I, namely $\mathbf{q}_d$ and $-\mathbf{q}_d$. A poorly chosen sign for the desired quaternion can cause an undesirable unwinding behavior,

where the reorientation trajectory is non-geodesic. As we discussed in the previous chapter, for a simple remedy, we choose the sign of the desired quaternion $\mathbf{q}_d$ corresponding to the one yielding the shorter Euclidean distance between

$$\| \mathbf{q_d} - \mathbf{q}_0 \| \quad \text{and} \quad \| \mathbf{q_d} + \mathbf{q}_0 \|, \tag{3.24}$$

where $\mathbf{q}_0$ denotes current attitude or initial attitude. In subsequent sections, we will utilize an attitude error function $V : \mathcal{S}^3 \times \mathcal{S}^3 \to \mathbb{R}_+$, measuring the error between the current attitude and the desired attitude as

$$V = \| \mathbf{q}_d \pm \mathbf{q} \|^2, \tag{3.25}$$

where $\mathbf{q}_d$ denotes the desired attitude and $\pm$ denotes the sign which will be chosen depending on the sign of $\mathbf{q}_d$.

A negative log barrier function is a continuous convex function whose value on a point increases to infinity as the point approaches the boundary of the feasible region. It is used as a penalizing term for violations of constraints. For example, given the feasible set $\mathcal{D}_x = \{x | x > 0\}$, consider $f : x \in \mathcal{D}_x \to \mathbb{R}$,

$$f(x) = -\log(x) \tag{3.26}$$

where log denotes the natural logarithm. Then, since

$$-\log(x) \to \infty \text{ as } x \to 0, \tag{3.27}$$

$f(x)$ blows up at the boundary and therefore it presents a barrier around the feasible set. In order to utilize the convex parameterization of the forbidden and mandatory zones in the context of a potential function, we consider such a logarithmic barrier function $V : \mathbf{q_p} \to \mathbb{R}_+$,

$$V(\mathbf{q}) = \|\mathbf{q}_d - \mathbf{q}\|^2 \Big[\underbrace{\sum_{j=1}^{m} \sum_{i=1}^{n} -k_1 \log\Big(-\frac{\mathbf{q}^T M_i^j \mathbf{q}}{2} \Big)}_{\text{attitude forbidden zones}} \underbrace{-k_2 \log\Big(\frac{\mathbf{q}^T M_M \mathbf{q}}{2} \Big)}_{\text{attitude mandatory zone}} \Big], \tag{3.28}$$

where $\mathbf{q_p} \subseteq \mathcal{S}^3$, k_1 and k_2 are positive weighting parameters for the attitude forbidden zones and mandatory zones, respectively, and $\mathbf{q}_d$ is the desired destination attitude. We note that

the notational dependency of the matrices M_i^j and M_M on the angle θ_i^j as well as the chosen sign of $\mathbf{q}_d$ have been suppressed above; we will continue to use this shortened notation for the remainder of our discussion.

Proposition 3.6. *The potential function V in Eq. (3.28) is smooth and strictly convex for all $\mathbf{q} \in \mathbf{q}_{\boldsymbol{p}}$ and admits a global minimum at $\mathbf{q}_d \in \mathbf{q}_{\boldsymbol{p}}$.*

Proof. We will show that V in Eq. (3.28) meets the following three conditions:

1. $V(\mathbf{q}_d) = 0$,
2. $V(\mathbf{q}) > 0, \quad \text{for all } \mathbf{q} \in \mathbf{q}_{\boldsymbol{p}} \backslash \{\mathbf{q}_d\}$,
3. $\nabla^2 V(\mathbf{q})$ is positive definite for all $\mathbf{q} \in \mathbf{q}_{\boldsymbol{p}}$.

It is clear that $V(\mathbf{q}_d) = 0$. From Eqs. (3.18) and (3.20), the inequalities,

$$0 < -\frac{\mathbf{q}^T M_i^j \mathbf{q}}{2} < 1 \text{ and } 0 < \frac{\mathbf{q}^T M_M \mathbf{q}}{2} < 1, \tag{3.29}$$

hold and hence the negative logarithm function Eq. (3.28) is always positive; moreover, for all $\mathbf{q} \in \mathbf{q}_{\boldsymbol{p}}$,

$$\sum_{i=1}^{n} -\log\left(-\frac{\mathbf{q}^T M_i^j \mathbf{q}}{2}\right) > 0 \text{ and } -\log\left(\frac{\mathbf{q}^T M_M \mathbf{q}}{2}\right) > 0. \tag{3.30}$$

Hence $V(\mathbf{q}) > 0$ for all $\mathbf{q} \in \mathbf{q}_{\boldsymbol{p}} \backslash \{\mathbf{q}_d\}$.

The last part of the proposition can be shown by first swapping the quaternion quadratic terms $-\mathbf{q}^T M_i^j \mathbf{q}$ and $\mathbf{q}^T M_M \mathbf{q}$ for the following equivalent terms:

$$\begin{aligned} -\mathbf{q}^T M_i^j \mathbf{q} &> 0, \\ -\mathbf{q}^T M_i^j \mathbf{q} + \beta_1 - \beta_1 &> 0, \\ \mathbf{q}^T \tilde{M}_i^j \mathbf{q} - \beta_1 &> 0, \end{aligned} \tag{3.31}$$

where β_1 is defined as $-\lambda_{\max}(M_i^j) + \beta_1 > 0$ such that $\tilde{M}_i^j$ is a positive definite matrix, and

$$\begin{aligned} \mathbf{q}^T M_M \mathbf{q} &> 0, \\ \mathbf{q}^T M_M \mathbf{q} + \beta_2 - \beta_2 &> 0, \\ \mathbf{q}^T \tilde{M}_M \mathbf{q} - \beta_2 &> 0, \end{aligned} \tag{3.32}$$

where β_2 is defined as $\lambda_{\min}(M_M) + \beta_2 > 0$ such that $\tilde{M}_M$ is a positive definite matrix. Now the potential function (3.28) assumes the form

$$V(\mathbf{q}) = \|\mathbf{q}_d - \mathbf{q}\|^2 \Big[\Big(\sum_{j=1}^{m} \sum_{i=1}^{n} -k_1 \log(\frac{\mathbf{q}^T \tilde{M}_i^j \mathbf{q} - \beta_1}{2}) \Big) - k_2 \log(\frac{\mathbf{q}^T \tilde{M}_M \mathbf{q} - \beta_2}{2}) \Big]. \tag{3.33}$$

The above expression for the potential function is comprised of linear combinations of logarithmic functions. Since the summation of strictly convex functions is strictly convex, it suffices to analyze one of the terms in more detail, say,

$$V(\mathbf{q}) = \|\mathbf{q}_d - \mathbf{q}\|^2 \Big[\sum_{i} -k \log(\frac{\mathbf{q}^T \tilde{M}_i^j \mathbf{q} - \beta_1}{2}) \Big], \tag{3.34}$$

for some indices i and j. In this direction, the gradient of V is calculated as

$$\begin{aligned} \nabla V = & \Big(\frac{\partial}{\partial \mathbf{q}} \|\mathbf{q}_d - \mathbf{q}\|^2 \Big) \Big[\sum_{i} -k \log(\frac{\mathbf{q}^T \tilde{M}_i^j \mathbf{q} - \beta_1}{2}) \Big] \\ & + \|\mathbf{q}_d - \mathbf{q}\|^2 \Big[\sum_{i} \frac{-2k}{\mathbf{q}^T \tilde{M}_i^j \mathbf{q} - \beta_1} \mathbf{q}^T \tilde{M}_i^j \Big], \end{aligned} \tag{3.35}$$

and the Hessian $\nabla^2 V$ is given as

$$\begin{aligned} \nabla^2 V = & \Big(\frac{\partial^2}{\partial \mathbf{q}^2} \|\mathbf{q}_d - \mathbf{q}\|^2 \Big) \Big[\sum_{i} \Big(- k \log(\frac{\mathbf{q}^T \tilde{M}_i^j \mathbf{q} - \beta_1}{2}) \Big) \Big] \\ & + \Big(\frac{\partial}{\partial \mathbf{q}} \|\mathbf{q}_d - \mathbf{q}\|^2 \Big)^T \Big[\sum_{i} \frac{-2k}{\mathbf{q}^T \tilde{M}_i^j \mathbf{q} - \beta_1} \mathbf{q}^T \tilde{M}_i^j \Big] \\ & + \Big[\sum_{i} \frac{-2k}{\mathbf{q}^T \tilde{M}_i^j \mathbf{q} - \beta_1} \mathbf{q}^T \tilde{M}_i^j \Big]^T \Big(\frac{\partial}{\partial \mathbf{q}} \|\mathbf{q}_d - \mathbf{q}\|^2 \Big) \\ & + \|\mathbf{q}_d - \mathbf{q}\|^2 \Big[\sum_{i} \frac{4k}{\big(\mathbf{q}^T \tilde{M}_i^j \mathbf{q} - \beta_1\big)^2} \Big(\mathbf{q}^T \tilde{M}_i^j \Big)^T \mathbf{q}^T \tilde{M}_i^j \Big] \\ & + \|\mathbf{q}_d - \mathbf{q}\|^2 \Big[\sum_{i} \frac{-2k}{\mathbf{q}^T \tilde{M}_i^j \mathbf{q} - \beta_1} \tilde{M}_i^j \Big]. \end{aligned} \tag{3.36}$$

From the fact that

$$\frac{\partial}{\partial \mathbf{q}} \big(\|\mathbf{q}_d - \mathbf{q}\|^2 \big) = -2\mathbf{q}_d^T, \tag{3.37}$$

it follows that $\frac{\partial^2}{\partial \mathbf{q}^2} \big(\|\mathbf{q}_d - \mathbf{q}\|^2 \big) = \mathbf{0}_{4\times 4}$, and $\|\mathbf{q}_d - \mathbf{q}\|^2 = 2 - 2\mathbf{q}_d^T \mathbf{q}$, and thus the expression

(3.36) simplifies to

$$\begin{aligned}\nabla^2 V = \sum_i \Big\{ & \frac{4k}{\mathbf{q}^T \tilde{M}_i^j \mathbf{q} - \beta_1} \big(\mathbf{q}_d \mathbf{q}^T \tilde{M}_i^j + \tilde{M}_i^j \mathbf{q} \mathbf{q}_d^T\big) \\ & + \big(2 - 2\mathbf{q}_d^T \mathbf{q}\big) \frac{4k}{\big(\mathbf{q}^T \tilde{M}_i^j \mathbf{q} - \beta_1\big)^2} \big(\mathbf{q}^T \tilde{M}_i^j\big)^T \mathbf{q}^T \tilde{M}_i^j \\ & - \big(2 - 2\mathbf{q}_d^T \mathbf{q}\big) \frac{2k}{\mathbf{q}^T \tilde{M}_i^j \mathbf{q} - \beta_1} \tilde{M}_i^j \Big\}. \end{aligned} \tag{3.38}$$

Multiplying the last identity by $\mathbf{q}^T$ and $\mathbf{q}$ from left and right, respectively, yields

$$\begin{aligned}\mathbf{q}^T \nabla^2 V \mathbf{q} = \sum_i \Big\{ & \frac{8k}{\mathbf{q}^T \tilde{M}_i^j \mathbf{q} - \beta_1} \mathbf{q}^T \mathbf{q}_d \big(\mathbf{q}^T \tilde{M}_i^j \mathbf{q}\big) \\ & + \big(2 - 2\mathbf{q}_d^T \mathbf{q}\big) \frac{4k}{\big(\mathbf{q}^T \tilde{M}_i^j \mathbf{q} - \beta_1\big)^2} \big(\mathbf{q}^T \tilde{M}_i^j \mathbf{q}\big)^2 \\ & - \frac{2k\big(2 - 2\mathbf{q}_d^T \mathbf{q}\big)}{\mathbf{q}^T \tilde{M}_i^j \mathbf{q} - \beta_1} \big(\mathbf{q}^T \tilde{M}_i^j \mathbf{q}\big) \Big\}. \end{aligned} \tag{3.39}$$

By letting

$$\gamma = \frac{4k \mathbf{q}^T \tilde{M}_i^j \mathbf{q}}{(\mathbf{q}^T \tilde{M}_i^j \mathbf{q} - \beta_1)^2}, \tag{3.40}$$

which is always a positive value, we obtain

$$\mathbf{q}^T \nabla^2 V \mathbf{q} = \sum_i \gamma \Big\{ \big(\mathbf{q}^T \tilde{M}_i^j \mathbf{q} - 3\beta_1\big) \mathbf{q}_d^T \mathbf{q} + \big(\mathbf{q}^T \tilde{M}_i^j \mathbf{q} + \beta_1\big) \Big\}, \tag{3.41}$$

where $\beta_1 > 0$ and $\mathbf{q}^T \tilde{M}_i^j \mathbf{q} + \beta_1 > 0$ for all $\mathbf{q} \in \mathbf{q_p}$ from Eq. (3.31). The above equation is a linear function of $\mathbf{q}_d^T \mathbf{q}$. Since $\mathbf{q}_d^T \mathbf{q} \in [-1, 1]$, one has

$$-\mathbf{q}^T \tilde{M}_i^j \mathbf{q} - \beta_1 < \mathbf{q}^T \tilde{M}_i^j \mathbf{q} - 3\beta_1 < \mathbf{q}^T \tilde{M}_i^j \mathbf{q} + \beta_1. \tag{3.42}$$

Note that the left inequality is derived from Eq. (3.31). Then, the right-hand side of the equality in Eq. (3.41) remains positive for all $\mathbf{q}$, $\mathbf{q}_d \in \mathbf{q_p}$. Therefore, the Hessian of V is positive definite and V is smooth and strictly convex. □

Fig. 3.5 depicts the plot of $\mathbf{q}^T \nabla^2 V \mathbf{q}$ over values of $\mathbf{q}_d^T \mathbf{q}$; note that as long as $\mathbf{q}_d^T \mathbf{q} \in [-1, 1]$, $\mathbf{q}^T \nabla^2 V \mathbf{q}$ remains positive when $\mathbf{q} \neq \mathbf{q}_d$.

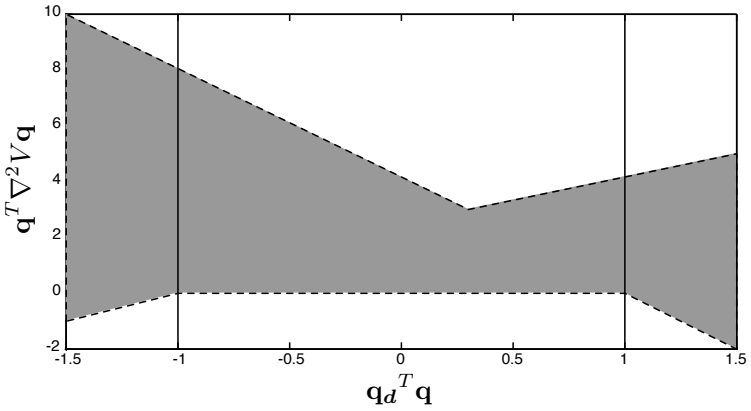

Figure 3.5: Plot of $\mathbf{q}^T\nabla^2 V\mathbf{q}$ over $\mathbf{q}_d^T\mathbf{q}$ for $k = 0.005$

3.5 Feedback Control Laws using Thrusters

In this section, we derive two control laws based on the logarithmic barrier potential function–now used as a Lyapunov function– for the purpose of showing almost global asymptotic stability of the corresponding closed loop system.

3.5.1 Rigid Body Dynamics

Prior to delving into the main topic of the present section, let us briefly review fundamentals of rigid body dynamics [104]. The attitude dynamics of a rigid spacecraft, equipped with fully actuated body-fixed torquing devices, can be described as,

$$\dot{\mathbf{q}}(t) = \frac{1}{2}\mathbf{q}(t) \otimes \boldsymbol{\omega}(t), \tag{3.43}$$

$$J\dot{\omega}(t) = -[\omega]_\times J\omega(t) + u(t), \tag{3.44}$$

where $\mathbf{q}(t)$ is the unit quaternion representing the attitude of the rigid body at time t, $\omega(t) \in \mathbb{R}^3$ denotes the angular velocity of the spacecraft in the body frame, $\boldsymbol{\omega}(t) = [\,\omega^T \;\; 0\,]^T_{4\times 1}$, $J = \mathtt{diag}(J_1,\ J_2,\ J_3)$ denotes the inertia matrix of the spacecraft in the body frame, $\boldsymbol{u}(t) \in \mathbb{R}^3$ represents the control torques about the body axes, and $[\omega]_\times$ denotes a cross

product operator in the matrix form associated with ω given as

$$[\omega]_\times = \begin{bmatrix} 0 & -\omega_3 & \omega_2 \\ \omega_3 & 0 & -\omega_1 \\ -\omega_2 & \omega_1 & 0 \end{bmatrix}. \tag{3.45}$$

In this section, in order to focus on deriving reorientation control laws for constrained attitude maneuvers, we assume that all external disturbances on the spacecraft are negligible.

3.5.2 Model Independent Control Law (Direct Lyapunov Method)

Given the unit quaternion parameterization of the spacecraft attitude, a number of model-independent feedback control laws for the rigid body reorientation may be derived using the following procedure. In fact, a qualified strictly convex penalty (cost) function $V(\mathbf{q}) \geq 0$ and the linearity of quaternion kinematics, i.e., $\dot{\mathbf{q}} = \frac{1}{2}\mathbf{q} \otimes \boldsymbol{\omega}$, enable us to derive a almost globally stable control law on the quaternion domain. In this venue, given a cost function $V(\mathbf{q})$ in unit quaternions, define

$$V_t = V + \frac{1}{2}\omega^T J \omega. \tag{3.46}$$

Then $V_t \geq 0$ for all $(\mathbf{q}, \omega)$ and the time derivative of V_t along Eqs. (3.43-3.44) is given by

$$\dot{V}_t = \nabla V^T (\frac{1}{2}\mathbf{q} \otimes \boldsymbol{\omega}) + \omega^T J \dot{\omega} \tag{3.47}$$

$$= \omega^T \mathtt{Vec}[-\nabla V^* \otimes \frac{1}{2}\mathbf{q}] + \omega^T u \tag{3.48}$$

$$= \omega^T \Big(\mathtt{Vec}[-\nabla V^* \otimes \frac{1}{2}\mathbf{q}] + u \Big), \tag{3.49}$$

where the operator $\mathtt{Vec}[\cdot]$ denotes the vector part of $[\cdot]$. By taking

$$u = -\alpha\omega + \frac{1}{2}\mathtt{Vec}[\nabla V^* \otimes \mathbf{q}], \tag{3.50}$$

where α denotes a positive parameter, Eq. (3.49) yields

$$\dot{V}_t = -\alpha \omega^T \omega \leq 0; \tag{3.51}$$

the implication of such an observation is now formally discussed.

Proposition 3.7. *The feedback control law given by Eq. (3.50) leads the cost function V, as well as the combined cost function V_t, to converge to zero asymptotically.*

Proof. Consider V_t as a candidate Lyapunov function. Let $S = \{\, \omega \,|\, \dot{V}_t = 0 \,\}$. From Eq. (3.51), it follows that $\dot{V}_t = 0$ implies that $\omega = 0$, which in turn, implies $u = 0$ by Eq. (3.44). Similarly, $\omega = 0$ and $u = 0$ implies that $\nabla V^* = 0$ in Eq. (3.50) since $\mathbf{q} \neq \mathbf{0}$. In addition, the fact V is strictly convex leads to the equivalency

$$\{\mathbf{q} \,|\, \nabla V = \nabla V^* = \mathbf{0}\} \Longleftrightarrow \{\mathbf{q} \,|\, V = 0\}; \tag{3.52}$$

hence the invariant set contains $\mathbf{q}_d$ for which we have $V(\mathbf{q}_d) = 0$, i.e,

$$\{\, \omega \,|\, \dot{V}_t = 0\} \Longrightarrow \{\, (\omega, \mathbf{q}) \,|\, V(\mathbf{q}_d) = 0 \text{ and } \omega = 0\}. \tag{3.53}$$

Therefore, by LaSalle's invariance principle [49], the equilibrium $(\mathbf{q}_d, \omega)$ is asymptotically stable. □

Remark 3.1. *As we discussed in the Chapter 2.3, a unit quaternion based continuous feedback control stabilizes the system almost globally asymptotically stable. This terminology originates from the fact that there is another bi-existent unstable equilibrium point $(-\mathbf{q}_d, \boldsymbol{\omega})$ in quaternion based dynamics. Thus, the proposed control, Eq. (3.50) necessarily stabilizes the system almost globally. For more details, see [13, 14, 77].*

Now, we propose a cost function for the attitude reorientation in the presence of attitude constrained zones. From Eq. (3.28), we have

$$V_t = V(\mathbf{q}) + \frac{1}{2}\omega^T J \omega, \tag{3.54}$$

where $\mathbf{q}_{\boldsymbol{p}} \subseteq \mathcal{S}^3$. As $V(\mathbf{q})$ is strictly convex in $\mathbf{q}$, according to *Proposition 8*, the dynamics induced by the negative gradient of V_t guide the state $\mathbf{q}$ towards the final $\mathbf{q}_d$ as V_t converges to zero. Moreover, if $\mathbf{q} \to \partial\mathbf{q}_{\boldsymbol{p}}$ or $\boldsymbol{\omega} \to \infty$, one has $V_t \to \infty$ which violates the (negative) gradient flow property of the underlying dynamics. From Eq. (3.50), we thus obtain an almost globally stabilizing model independent control

$$\boldsymbol{u} = -\alpha\omega - \mathtt{Vec}\Big[\big(l_g\, \mathbf{q}_d^* - \frac{1}{2}\|\mathbf{q}_d - \mathbf{q}\|^2\, \nabla {l_g}^*\big) \otimes \mathbf{q}\Big], \tag{3.55}$$

where $\alpha > 0$, and l_g denotes the summation of the logarithmic barrier potentials in Eq. (3.28) as

$$l_g = -\sum_{j=1}^{m}\sum_{i=1}^{n} k_1 \log\Big(\frac{\mathbf{q}^T M_i^j \mathbf{q}}{2}\Big) - k_2 \log\Big(\frac{\mathbf{q}^T M_M \mathbf{q}}{2}\Big). \tag{3.56}$$

3.5.3 Model Dependent Control Laws (Modified Integrator Backsteeping Method)

Our second type of feedback control for attitude constrained maneuvering is obtained using the modified backstepping method. This is achieved by observing that the spacecraft dynamics described by Eqs. (3.43)-(3.44) have a "cascaded" structure, thus making this dynamics suitable for control design based on the backstepping method [48]. However, one of the drawbacks of the conventional backstepping method is a typical excessive control during the initial phase of the trajectory, and sluggish closed loop dynamics in the later part of the trajectory–both of which are undesirable in practice. In this direction, we adopt the modified back-stepping method as discussed in [41], and propose an improved nonlinear error function for the constrained attitude control problem.

In this direction, let us first note that by letting

$$\dot{\mathbf{q}}(t) = -\nabla V(\mathbf{q}), \tag{3.57}$$

we have

$$\dot{V} = \frac{\partial V}{\partial \mathbf{q}} \cdot \frac{\partial \mathbf{q}}{\partial t} = \nabla V^T \cdot \dot{\mathbf{q}} = -\left\|\nabla V\right\|^2 < 0, \tag{3.58}$$

for all $\mathbf{q} \neq \mathbf{q}_d$, qualifying V as a *strong Lyapunov function* for the dynamics described by Eqs. (3.43)-(3.44), with respect to the equilibrium $\mathbf{q}_d$. Note that ∇V has units of $1/s$ since parameters k_1 and k_2 have units of $1/s$ in Eq. (3.28). Our strategy involves considering $\tilde{\boldsymbol{\omega}}$ in Eq. (3.43) as a "virtual" control input in order to have an asymptotically stable system Eq. (3.43) after closing the loop. Using quaternion identities, we now set

$$\tilde{\boldsymbol{\omega}}_c = -2\mathbf{q}^\star \otimes \nabla V. \tag{3.59}$$

Note that $\tilde{\boldsymbol{\omega}}_c$ has the form of quaternion with the last element identically zero as $\tilde{\boldsymbol{\omega}}_c = [\,\omega_c^T \; 0\,]^T$. Let $\tilde{\boldsymbol{z}}$ denote the error between $\tilde{\boldsymbol{\omega}}$ and its desired value $\tilde{\boldsymbol{\omega}}_c$ as,

$$\tilde{\boldsymbol{z}} = \tilde{\boldsymbol{\omega}} - \tilde{\boldsymbol{\omega}}_c = \tilde{\boldsymbol{\omega}} + 2\mathbf{q}^\star \otimes \nabla V, \tag{3.60}$$

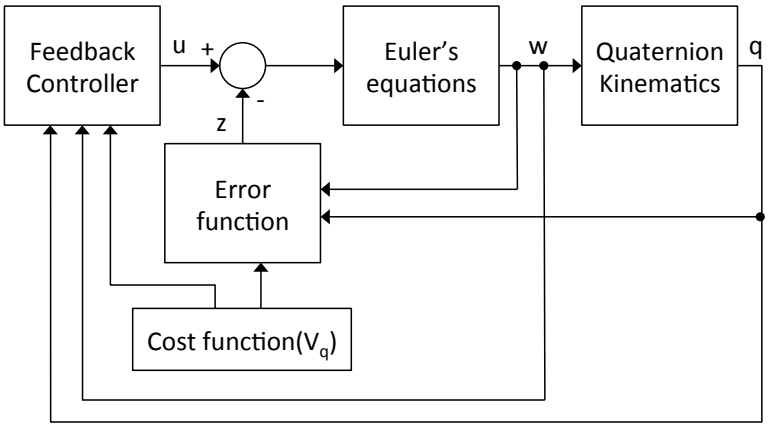

Figure 3.6: Modified Back-stepping controller scheme

where $\tilde{\boldsymbol{z}} = [\, \boldsymbol{z}^T \; 0\,]^T$. In the control scheme depicted in Fig. 3.6, the error function $\tilde{\boldsymbol{z}}$ acts as a feed-forward term and causes excessive control inputs in the initial phase of the control input when the error is large. Hence, we propose a modified error function as

$$\tilde{\boldsymbol{z}} = \alpha \arctan \beta(\tilde{\boldsymbol{\omega}} - \tilde{\boldsymbol{\omega}}_c) = \alpha \arctan \beta(\tilde{\boldsymbol{\omega}} + 2\mathbf{q}^\star \otimes \nabla V), \tag{3.61}$$

where α and β are the shaping parameters [41]. Thereby

$$\tilde{\boldsymbol{\omega}} = \frac{1}{\beta} \tan\left(\frac{1}{\alpha}\tilde{\boldsymbol{z}}\right) - 2\mathbf{q}^\star \otimes \nabla V. \tag{3.62}$$

Next, by plugging the above expression for $\tilde{\boldsymbol{\omega}}$ in Eq. (3.43), we obtain

$$\begin{aligned} \dot{\mathbf{q}} &= \frac{1}{2}\mathbf{q} \otimes \tilde{\boldsymbol{\omega}} \\ &= \frac{1}{2}\mathbf{q} \otimes \left(\frac{1}{\beta}\tan\left(\frac{1}{\alpha}\tilde{\boldsymbol{z}}\right)\right) - \nabla V. \end{aligned} \tag{3.63}$$

In addition, the time derivative of the vector part of Eq. (3.61) along with Eq. (3.44) is now given as

$$\begin{aligned} J\dot{\boldsymbol{z}} &= J\frac{d}{dt}\alpha \arctan \beta\,(\boldsymbol{\omega} - \boldsymbol{\omega}_c) \\ &= C_1\big(R(\omega)\, J\boldsymbol{\omega}(t) + \boldsymbol{u}(t) - J\dot{\boldsymbol{\omega}}_c\big), \end{aligned} \tag{3.64}$$

where $C_1 = \alpha\beta\left[I_3 + \beta^2\, \mathtt{diag}(\boldsymbol{\omega} - \boldsymbol{\omega}_c)^2\right]^{-1}$.

In order to find an input $\boldsymbol{u}(t)$ which stabilizes the system Eqs. (3.63)-(3.64), we define an augmented candidate Lyapunov function

$$V(\mathbf{q}, \boldsymbol{z}) = V + \frac{1}{2}\boldsymbol{z}^T J \boldsymbol{z}. \tag{3.65}$$

Taking the time derivative of V along the trajectories of Eqs. (3.63)-(3.64), we obtain,

$$\begin{aligned}\dot{V} &= \nabla V^T \dot{\mathbf{q}} + \boldsymbol{z}^T J \dot{\boldsymbol{z}} \\ &= \nabla V^T (\frac{1}{2}\mathbf{q} \otimes \tilde{\boldsymbol{z}}) - \|\nabla V\|^2 + \boldsymbol{z}^T C_1 (R(\boldsymbol{\omega})\, J\boldsymbol{\omega}(t) + \boldsymbol{u}(t) - J\dot{\boldsymbol{\omega}}_c).\end{aligned} \tag{3.66}$$

By rearranging the term $\nabla V^T(\frac{1}{2}\mathbf{q} \otimes \tilde{\boldsymbol{z}})$ and using quaternion identities, Eq. (3.66) now assumes the form,

$$\begin{aligned}\dot{V} &= \nabla V^T (\frac{1}{2}\mathbf{q} \otimes \tilde{\boldsymbol{z}}) - \|\nabla V\|^2 + \boldsymbol{z}^T C_1 (R(\boldsymbol{\omega})\, J\boldsymbol{\omega}(t) + u(t) - \boldsymbol{J\dot{\omega}_c}) \\ &= \boldsymbol{z}^T (\frac{1}{2} q_0 \mathtt{Vec}[\nabla V_q] + \frac{1}{2}\mathtt{Vec}[\nabla V] \times \mathbf{q} - \frac{1}{2}\nabla V_0 \mathbf{q}) - \|\nabla V\|^2\, \boldsymbol{z}^T C_1 (R(\boldsymbol{\omega})\, J\boldsymbol{\omega}(t) + \boldsymbol{u}(t) - J\dot{\boldsymbol{\omega}}_c) \\ &= \boldsymbol{z}^T \big(\frac{1}{2} q_0 \mathtt{Vec}[\nabla V] + \frac{1}{2}\mathtt{Vec}[\nabla V] \times \boldsymbol{q} - \frac{1}{2}\nabla V_0 \boldsymbol{q} + C_1 [R(\omega)\, J\omega(t) u(t) - J\dot{\boldsymbol{\omega}}_c]\big) - \|\nabla V\|^2 ,\end{aligned} \tag{3.67}$$

where $\nabla V = [\,\mathtt{Vec}[\nabla V]^T \;\; \nabla V_0]^T$. Then by choosing the actuator torque as,

$$u(t) = J\dot{\boldsymbol{\omega}}_c - R(\boldsymbol{\omega})\, J\boldsymbol{\omega}(t) - C_1^{-1}\big[\frac{1}{2} q_0 \mathtt{Vec}[\nabla V] - \frac{1}{2}\mathtt{Vec}[\nabla V] \times \boldsymbol{q} + \frac{1}{2}\nabla V_0 \boldsymbol{q} - \boldsymbol{z}\big], \tag{3.68}$$

one has

$$\dot{V} = -\|\nabla V\|^2 - \boldsymbol{z}^T \boldsymbol{z} \leq 0, \tag{3.69}$$

guaranteeing that the overall system is asymptotically stable. From Eq. (3.61), on the other hand, we note that

$$\boldsymbol{z} = \alpha \arctan \beta \left(\mathtt{Vec}[\tilde{\boldsymbol{\omega}} + 2\mathbf{q}^\star \otimes \nabla V]\right). \tag{3.70}$$

Now, rewriting the actuator torque $\boldsymbol{u}$ in $\boldsymbol{\omega}$ using the quaternion identities, we obtain,

$$\boldsymbol{u}(\boldsymbol{\omega}) = J\dot{\boldsymbol{\omega}}_c - R(\boldsymbol{\omega})\, J\boldsymbol{\omega} + \frac{1}{2} C_2 \mathtt{Vec}[\nabla \boldsymbol{V}^\star \otimes \mathbf{q}] - \boldsymbol{z}, \tag{3.71}$$

where

$$C_2 = (1/\alpha\beta)[I_3 + \beta^2\, \mathtt{diag}(\boldsymbol{\omega} - \boldsymbol{\omega}_c)^2].$$

The next step pertains to computing the term $\dot{\boldsymbol{\omega}}_{\boldsymbol{c}}$ which appears in the control law Eq. (3.71). This term is the time derivative of Eq. (3.59), which should be computed directly when the control law is implemented. In the meantime, the time derivative of the vector part of $\tilde{\boldsymbol{\omega}}_c$ can be given as,

$$\begin{aligned}\dot{\boldsymbol{\omega}}_c &= \frac{\partial}{\partial t}\big(2\nabla V_0 \boldsymbol{q} - 2q_0 \mathtt{Vec}[\nabla V] + 2\boldsymbol{q} \times \mathtt{Vec}[\nabla V]\big) \\ &= -2(\mathtt{Vec}[\dot{\mathbf{q}}^\star \otimes \nabla \boldsymbol{V} + \mathbf{q}^\star \otimes \nabla^2 \boldsymbol{V} \dot{\mathbf{q}}]). \end{aligned} \tag{3.72}$$

3.5.4 Numerical Simulations

In this section, in order to illustrate the effectiveness of the proposed methodology, we present simulation results for three types of cases. In all of these cases, it has been assumed that the spacecraft carries a light sensitive instrument with a fixed bore-sight in the spacecraft body axes, directed along the Z direction. Moreover, it is assumed that a high gain antenna has been mounted on the spacecraft such that its bore-sight is directed along the Y axis; see Fig. 3.7. We note that the parameters k_i's in Eq. (3.28) influence the convergence rate of the algorithm since the corresponding logarithmic terms rapidly increase as the norm $\|\mathbf{q}_d - \mathbf{q}\|^2$, associated with an attraction term towards the destination attitude, decreases. From the simulations presented here, the values of k_i's are chosen around 0.005 for each constraint, while the spacecraft's moments of inertia is set as,

$$J = \mathtt{diag}[\,694,\ 572,\ 360\,]\ \text{kg}{\cdot}m^2. \tag{3.73}$$

Generally, larger values of k_i prolong the convergence to the destination attitude, particularly when the desired attitude is close to the boundary of the constraint set.

Case 1 (4 attitude forbidden zones)

We consider the case in which the spacecraft is re-targeting its telescope while avoiding four attitude forbidden zones in the spacecraft rotational configuration space. Both initial and desired attitudes are randomly chosen in the attitude permissible zone, satisfying the following inequalities for all i,

$$\mathbf{q}_0^T M_i^1 \mathbf{q}_0 < 0 \quad \text{and} \quad \mathbf{q}_d^T M_i^1 \mathbf{q}_d < 0, \tag{3.74}$$

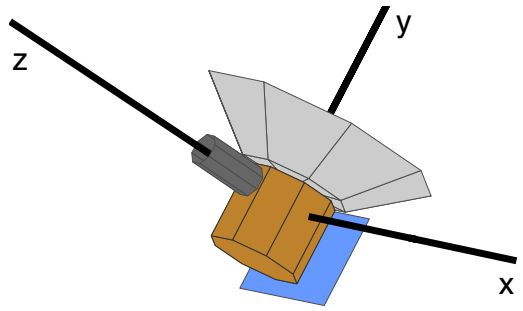

Figure 3.7: Spacecraft configuration with one light sensitive instrument (z axis) and a high gain antenna (y axis).

where $\mathbf{q}_0$ and $\mathbf{q}_d$ are the initial and desired unit quaternions, respectively. These attitude forbidden zones are randomly chosen with the provision of not overlapping with each other in this example–however, this is not necessary in general as long as a feasible trajectory exists. Also, the identity unit quaternion $\mathbf{q_I}$ is chosen to have the opposite sign as the scalar part of $\mathbf{q}_d^\star \otimes \mathbf{q}_0$ in order to avoid the unwinding phenomenon.

We conduct the simulations in the context of two different scenarios and two types of control laws discussed in this paper. In Table 3.1, the initial and desired spacecraft attitudes are given in unit quaternions as well as the normalized position vectors, indicating four constrained sets (forbidden zones), all expressed with respect to the inertial frame. The potential function for this case is given as,

$$V(\mathbf{q}) = \|\mathbf{q}_d - \mathbf{q}\|^2 \left[\Big(\sum_{i=1}^{4} -k_1 \log(-\frac{\mathbf{q}^T M_i^1 \mathbf{q}}{2}) \Big) \right], \tag{3.75}$$

where M_i^1 depends on the ith position vector indicating the corresponding constraint set. Fig. 3.8 represents the trajectories of the pointing direction of the light sensitive instrument on the celestial sphere generated by model independent control laws with the initial attitude (denoted by '$\circ$') and the desired attitude (denoted by '$\times$'). In Fig. 3.9 the same trajectories are depicted on the cylindrical projection of the corresponding celestial spheres for model independent and model dependent control laws. For comparison, Fig. 3.9 also traces the analogous plots for the non-geodesic (longer) trajectories obtained using $-\mathbf{q_I}$. As shown in Figs. 3.10-3.11, the required final states are achieved asymptotically in all scenarios.

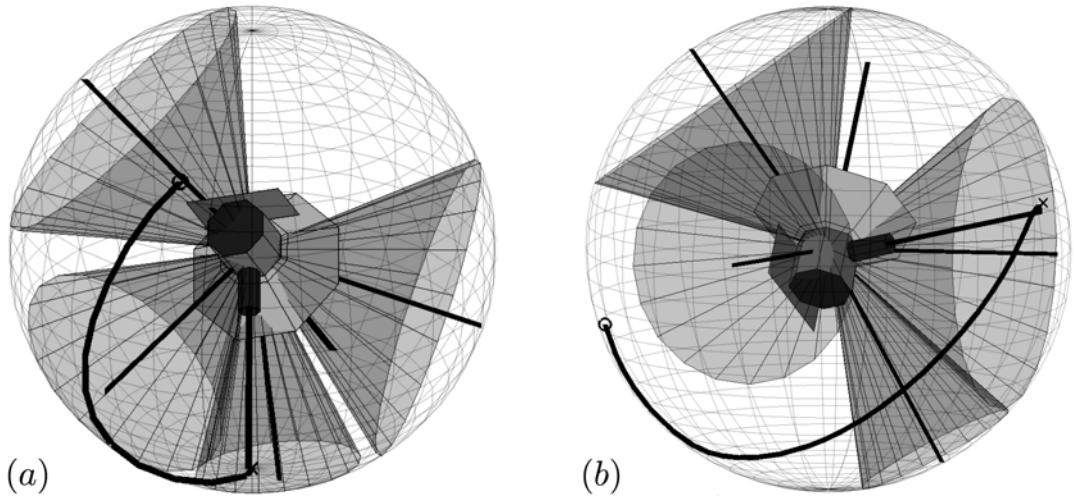

Figure 3.8: Case 1: Trace of the telescope pointing direction on the celestial sphere generated by model independent control law. The "circle" and the "cross" on the sphere indicate the directions of the initial and final orientations, respectively.

Case 1-(a)

Initial Attitude	Constrained object	Angle
[-0.187 -0.735 -0.450 -0.470]	[0.174, -0.934, -0.034]	40 deg
	[0, 0.707 0.707]	40 deg
Desired Attitude	[-0.853, 0.436, -0.286]	30 deg
[0.592 -0.675 -0.215 0.382]	[-0.122, -0.140, -0.983]	20 deg

Case 1-(b)

Initial Attitude	Constrained object	Angle
[0.452 0.682 0.465 -0.336]	[0.163, -0.986, 0.02]	20 deg
	[0, 0.573, 0.819]	30 deg
Desired Attitude	[-0.067, -0.462, -0.88]	20 deg
[0.029 0.659 -0.619 -0.425]	[-0.813, 0.548, -0.19]	40 deg

Table 3.1: Case 1 simulation parameters (4 attitude forbidden zones)

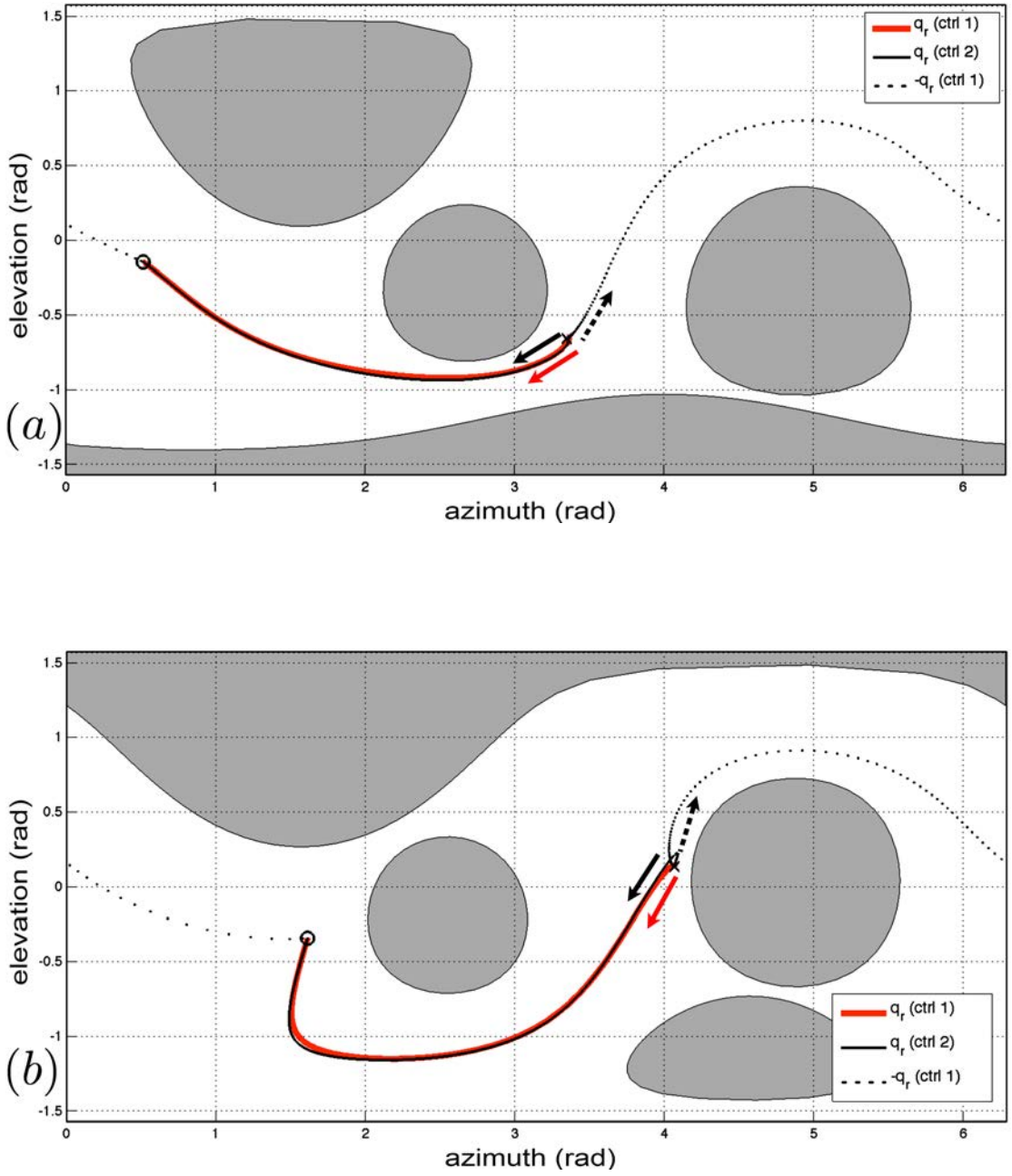

Figure 3.9: Case 1: Reorientation trajectories in the 2-D cylindrical projection for two types of controls (solid line); for comparison, non-geodesic trajectories are also depicted (dotted line).

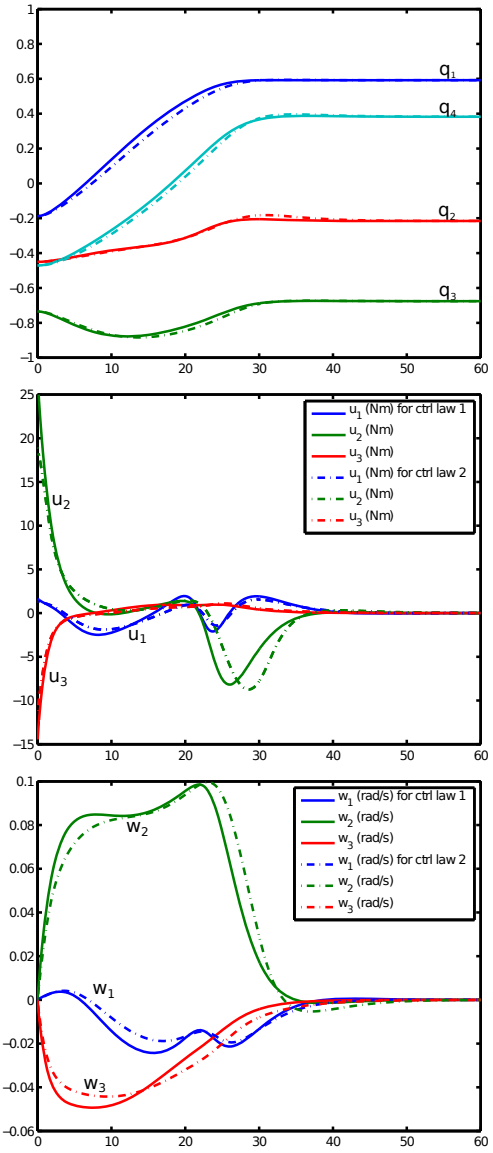

Figure 3.10: Case 1-a: time histories for quaternion trajectories, control inputs, and angular velocities; the time axis is in seconds.

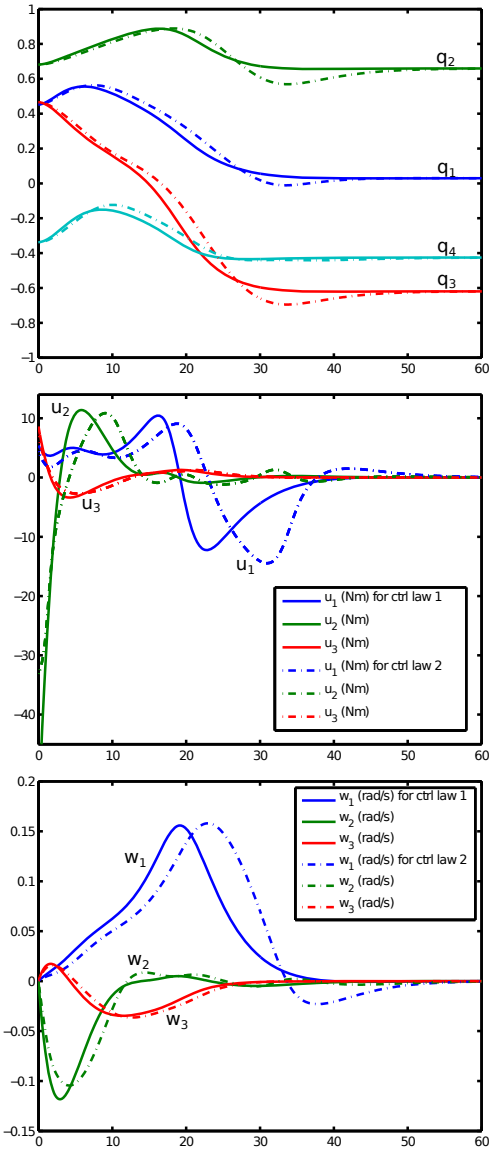

Figure 3.11: Case 1-b: time histories for quaternion trajectories, control inputs, and angular velocities; the time axis is in seconds.

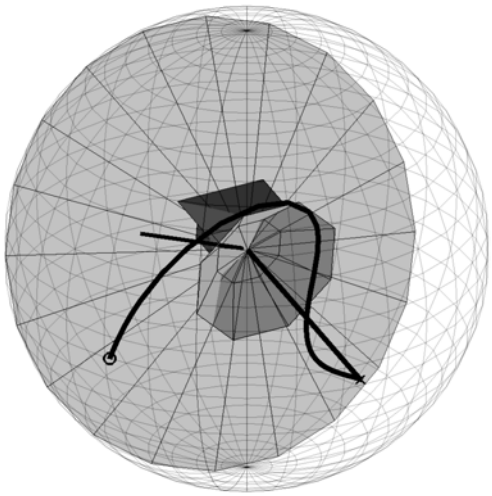

Figure 3.12: Case 2: Trajectory in the celestial attitude mandatory zone.

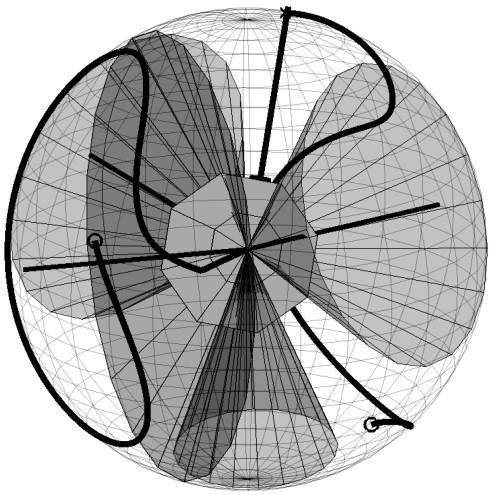

Figure 3.13: Case 3: Trajectory in the celestial attitude mandatory and forbidden zones.

Case 2 (1 attitude mandatory zone)

The purpose of this simulation scenario is to verify the utility of the proposed methodology for reorientation maneuvers frequently required for micro-satellite formation flying. Since each micro-satellite is not fully equipped with necessary inertial position sensors on-board, e.g., star trackers, it becomes important that the on-board guidance system has the ability to point the directional antenna in a specified direction for inter-spacecraft communication and sensing. Therefore in this simulation, we have considered a reorientation maneuver within the attitude mandatory zone associated with an on-board antenna. In these simulations, the moment of inertia and the shaping parameter k_2 are set as,

$$J = \texttt{diag}(\,2.4,\ 3.1,\ 1.4\,)\ \text{kg}{\cdot}m^2 \quad \text{and} \quad k_2 = 0.02. \tag{3.76}$$

The logarithmic barrier potential function for this case assumes the form,

$$V(\mathbf{q}) = \|\mathbf{q}_d - \mathbf{q}\|^2 \Big[- k_2 \log(\frac{\mathbf{q}^T M_M \mathbf{q}}{2}) \Big], \tag{3.77}$$

where M_M is given in Eq. (3.9). The initial and desired attitudes on the other hand, which should be in the mandatory zone, have been specified as,

$$\mathbf{q}_0^T M_M \mathbf{q}_0 > 0 \quad \text{and} \quad \mathbf{q}_d^T M_M \mathbf{q}_d > 0, \tag{3.78}$$

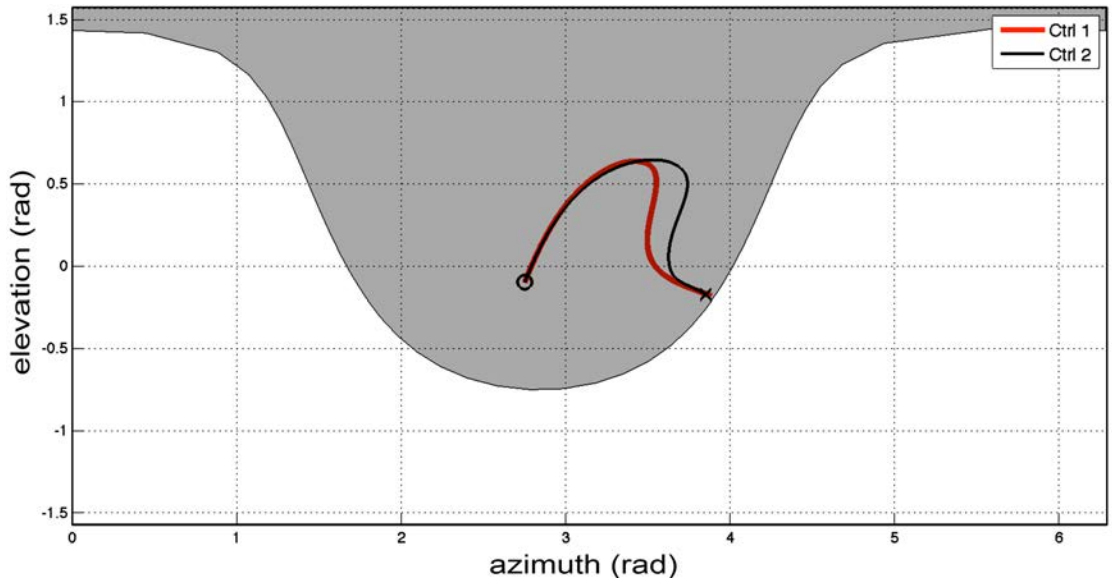

Figure 3.14: Case 2: Reorientation trajectories in the 2-D cylindrical projection space in the presence of 1 attitude mandatory zone.

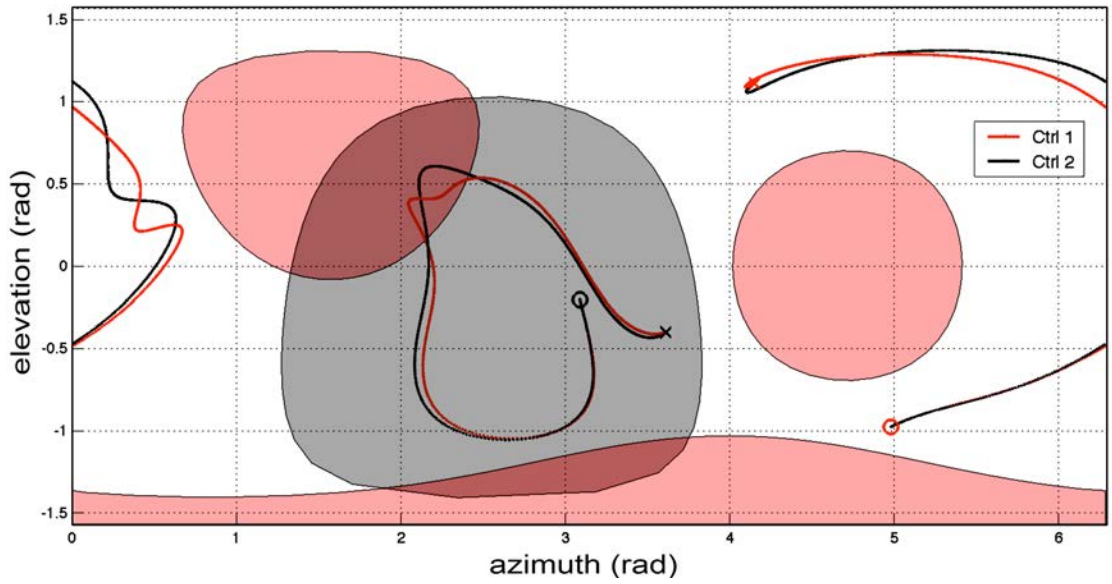

Figure 3.15: Case 3: Reorientation trajectories in the 2-D cylindrical projection space. Shown trajectory is geodesic. Non-geodesic rotation (from wrongly signed $\mathbf{q}$) will cause many oscillations around the boundary.

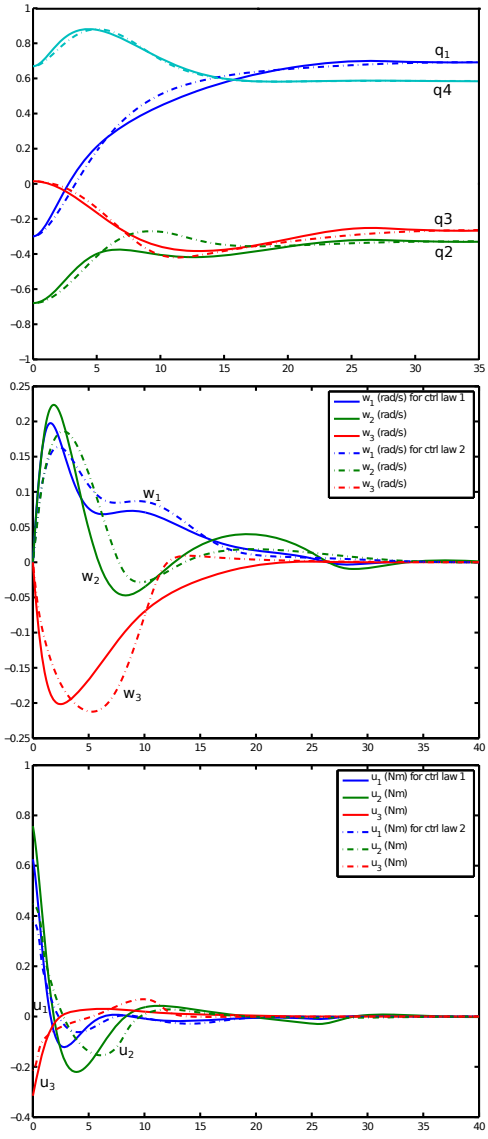

Figure 3.16: Case 2: time histories for quaternion trajectories, control inputs, and angular velocities; the time axis is in seconds.

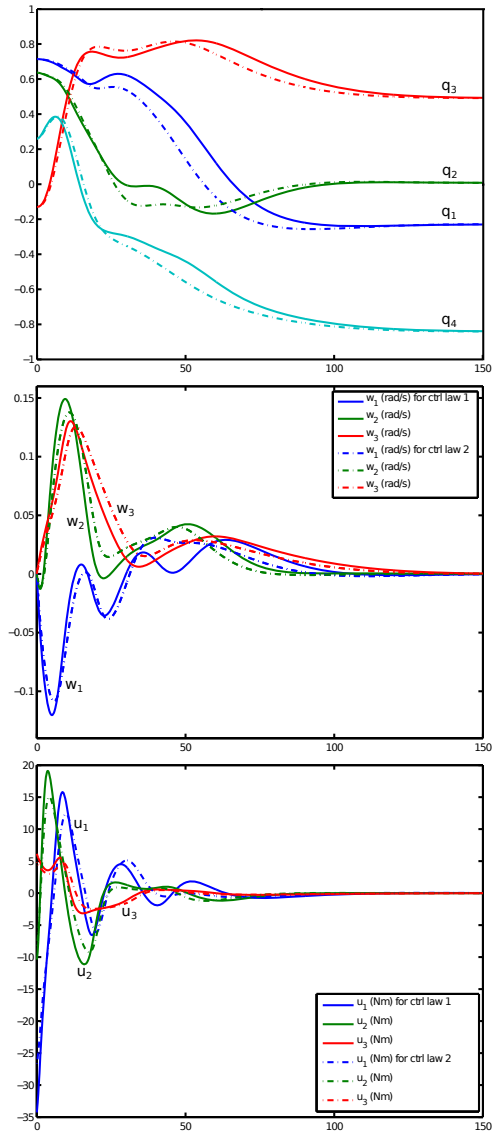

Figure 3.17: Case 3: time histories for quaternion trajectories, control inputs, and angular velocities; the time axis is in seconds.

Initial Attitude	Constrained object	Angle	Type
[-0.299 -0.679 0.014 0.669]	[-0.852 0.265 0.449]	70 deg	M

Desired Attitude
[0.693 -0.327 -0.263 0.585]

Table 3.2: Case 2 Constraint parameters

where $\mathbf{q}_0$, $\mathbf{q}_d$ are the initial and desired spacecraft attitudes, respectively. Figs. 3.12 depicts the model independent control generated reorientation trajectory on the celestial sphere while Fig 3.14. represents the trajectories governed by two types of control law; see Fig. 3.16 for the corresponding simulation results as well as Table 3.2 for the simulation parameters. In this simulation scenario, we have assumed that the spacecraft is initially stationary.

Remark 3.2. *It is worth noting that in the presence of an attitude mandatory zone, it becomes more important to choose the right unit quaternion for the geodesic (shorter) trajectories. Otherwise, the non-geodesic rotation will lead it to the boundary and cause a large number of oscillations by convex potential.*

Case 3 (3 attitude forbidden zones and 1 mandatory zone)

In case 3, we examine a more complex reorientation maneuver (see Fig. 3.18) for keeping a fixed bore-sight vector, e.g., an antenna, within a certain angle in order to continuously communicate with the ground station while the spacecraft is re-targeting its light sensitive instrument avoiding multiple bright objects or constrained zones. In this case, the feasible spacecraft attitude for reorientation can be represented using a combination of an attitude mandatory zone and attitude forbidden zones. For this scenario, the antenna has been aligned along the Z-axis while the sensitive instrument has been aligned along the Y-axis; see Fig. 3.7. This case is distinct from the earlier ones because in order for the spacecraft

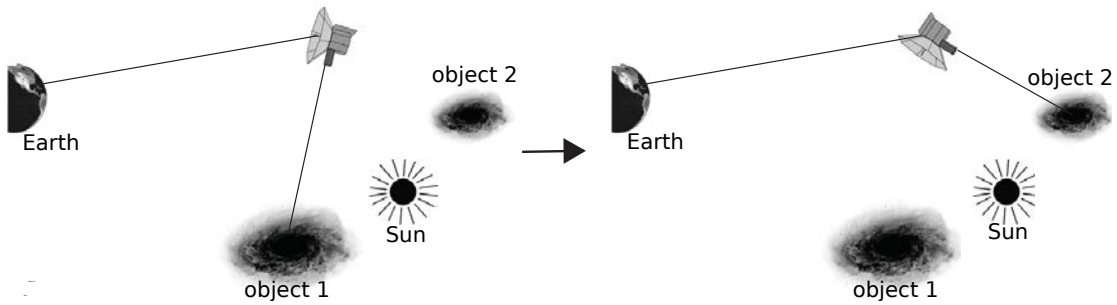

Figure 3.18: Reorientation under a combination of attitude mandatory and forbidden zones (Case 3)

reorientation to be feasible, one has to take an additional condition into account as

$$\mathbf{q}_0^T M_M(\theta_M)\mathbf{q}_0 > 0 \text{ and } \mathbf{q}_0^T M_i^j \mathbf{q}_0 < 0, \text{ for all } i, j, \tag{3.79}$$

and

$$\mathbf{q}_d^T M_M(\theta_M)\mathbf{q}_d^T > 0 \text{ and } \mathbf{q}_d^T M_i^j \mathbf{q}_d^T < 0, \quad \text{for all } i, j. \tag{3.80}$$

Note that the set of physically feasible conditions is a subset of the above requirements.

Remark 3.3. *We note that since this case includes an attitude mandatory zone(case 2) as well as attitude forbidden zones, selecting the right signed unit quaternion for geodesic rotation is more important than the other cases. Depends on the initial configuration, the non-geodesic rotation may cause a large number of oscillations to reach the desired orientation.*

In this direction, let us adopt the potential function,

$$V(\mathbf{q}) = \|\mathbf{q}_d - \mathbf{q}\|^2 \Big[\Big(\sum_{i=1}^{3} -k_1 \log(-\frac{\mathbf{q}^T M_i^1 \mathbf{q}}{2})\Big) - k_2 \log(\frac{\mathbf{q}^T M_M \mathbf{q}}{2})\Big], \tag{3.81}$$

where M_1, M_2, and, M_3 are associated with the three attitude forbidden zones and M_M corresponds to the attitude mandatory zone. We use the spacecraft's moments of inertia as in Eq. (4.73). Figs. 3.13 and 3.15 demonstrate a reorientation maneuver while keeping the antenna's bore-sight vector within 70 degrees of the permissible cone by the proposed

Initial attitude	Constrained object	Angle	Type
[0.714 0.637 -0.13 0.26]	[-0.813 0.548 -0.192]	70 deg	M
	[0 -1 0]	40 deg	F
Desired Attitude	[0 0.819 0.573]	40 deg	F
[-0.23 0.008 0.491 -0.84]	[-0.122 -0.139 -0.982]	20 deg	F

Table 3.3: Simulation settings for case 3

control laws. The simulation parameters for this scenario are given in Table 3.3. Fig. 3.17 shows the time histories for the quaternions trajectories and control inputs along the three independent spacecraft axes, as well as the time history for the spacecraft angular velocity.

3.5.5 Concluding Remarks

In this section, an autonomous maneuver planning algorithm for three axes attitude reorientation in the presence of multiple types of attitude constrained zones has been proposed. This has been achieved via a convex logarithmic barrier potential that is built on the convex parameterization of attitude constraint sets in the unit quaternion space. Based on such a potential function, we then proceeded to develop two types of control laws, referred to as model independent and model dependent. Simulation results have been presented within three distinct scenarios.

The main advantage of the proposed algorithm is its feedback-based *almost global* convergence properties from any initial condition, as well as its tractability and scalability for distinct classes of attitude constrained zones. Since this approach is analytical and computationally tractable, it is suitable for on-board autonomous spacecraft attitude maneuver planning.

3.6 Energy/Time Optimal Control

One of the key technologies of modern small spacecraft is fine attitude control, requiring high pointing accuracy and regulation [17]. As space system technology has developed,

smaller spacecraft, in the category of micro-satellites, have emerged as new candidates for space science missions. Recently developed micro reaction wheels enable micro-satellites to execute large angle reorientations. Planning a reorientation, while avoiding unwanted celestial objects is essential for science missions, since this type of maneuvering occurs frequently in actual missions. In order to conduct such missions with limited resources, energy/time optimal control assumes a critical role.

In the following section, we apply a direct numerical method to the convex attitude constrained zone parameterization to develop an algorithm for optimal attitude path planning in the presence of attitude constrained zones that uses minimal energy and time. Such direct numerical methods for trajectory optimization are attractive because explicit consideration of the necessary conditions such as adjoint equations, transversality conditions, and maximum principle, are not required [9]. In particular, the infinite dimensional optimal control problem is directly converted into a finite dimensional parameter optimization problem [19, 35, 84].

The presented problem is solved via a Gauss pseudospectral method where the optimal control problem is discretized at collocation points, and then transcribed to a nonlinear programming problem (NLP).

3.6.1 Optimal Attitude Control

In this section, we formulate the problem of reorienting a spacecraft with a dynamic model described in the previous section. We consider a rest-to-rest maneuver only. The optimal energy/time spacecraft reorientation control problem in the presence of attitude constrained zones is then determined by finding the state $\mathbf{q} \in S^3$ and the control torques on reaction wheels $\boldsymbol{u} \in \mathbf{R}^3$ that minimize the performance cost

$$J = \int_{t_0}^{t_f} \big(\rho + (1-\rho)|\boldsymbol{u}(t)| \big) dt. \tag{3.82}$$

Note that ρ denotes a weighting factor on the time, where $\rho = 0$ and $\rho = 1$ yield the energy optimal and time optimal performance cost, respectively. This objective is subject to the

differential dynamic constraints for $t \in [t_0, t_f]$,

$$\dot{\mathbf{q}}(t) = \frac{1}{2}\mathbf{q}(t) \otimes \tilde{\boldsymbol{\omega}}(t) \tag{3.83}$$

$$J\dot{\boldsymbol{\omega}}(t) = (J\boldsymbol{\omega} + J_r\boldsymbol{\omega}_r) \times \boldsymbol{\omega} - J_r\boldsymbol{u} \tag{3.84}$$

$$\dot{\boldsymbol{w}}_r = \boldsymbol{u}, \tag{3.85}$$

the boundary conditions

$$\mathbf{q}(t_0) = \mathbf{q}_{t_0}, \;\; \mathbf{q}(t_f) = \mathbf{q}_{t_f}, \;\; \boldsymbol{\omega}(t_0) = \mathbf{0}, \;\; \boldsymbol{\omega}(t_f) = \mathbf{0}, \quad \boldsymbol{\omega}_r(t_0) = \mathbf{0}, \tag{3.86}$$

control constraints, angular velocity limits on spacecraft and reaction wheels

$$|\, u_i \,| \leq \beta_u, \tag{3.87}$$

$$|\, \omega_i \,| \leq \beta_\omega, \tag{3.88}$$

$$|\, \omega_{r_i} \,| \leq \beta_{\omega_r}, \quad \text{for } i = 1, 2, 3, \tag{3.89}$$

path constraints for n attitude forbidden zones

$$\boldsymbol{q}^T M_{f_i} \boldsymbol{q} < 0, \quad \text{for } i = 1, ..., n \tag{3.90}$$

and path constraints for attitude mandatory zone

$$\boldsymbol{q}^T M_m \boldsymbol{q} > 0. \tag{3.91}$$

This optimal control problem was solved by a Gauss pseudospectral method (direct optimal control method) using the open source optimal control software GPOPS [31, 32] in conjunction with the nonlinear programming solver SNOPT and the automatic differentiator INTLAB.

3.6.2 Gauss Pseudospectral Method

Gauss pseudospectral method is a class of direct collocation where the optimal control problem is transcribed into a nonlinear programming problem (NLP) by approximating the state and control states using global orthogonal polynomials and collocating the differential

dynamic equations on *Legendre-Gauss* collocation points. The time interval $t \in [t_0, t_f]$ can be normalized to the time interval $\tau \in [-1, 1]$ via the affine transformation,

$$\tau = \frac{2t - t_f - t_0}{t_f - t_0}. \tag{3.92}$$

The states $\mathbf{q}(\tau)$ is approximated by the polynomial $\tilde{\mathbf{q}}(\tau)$ using a basis of $N+1$ Lagrange interpolating polynomials on the time interval of $[-1, 1]$ as

$$\mathbf{q}(\tau) \approx \tilde{\mathbf{q}}(\tau) = \sum_{i=0}^{N} \mathbf{q}(\tau_i) L_i(\tau_i), \tag{3.93}$$

where $L_i(\tau)$ is the ith Lagrange polynomial defined as

$$L_i(\tau) = \prod_{j=0, j\neq i}^{N} \frac{\tau - \tau_j}{\tau_i - \tau_j}, \quad (i = 0, ..., N). \tag{3.94}$$

The derivative of the state approximation is similarly obtained as

$$\dot{\mathbf{q}}(\tau_k) \approx \dot{\tilde{\mathbf{q}}}(\tau_k) = \sum_{i=0}^{N} \tilde{\mathbf{q}}(\tau_i) \dot{L}_i(\tau_k) = \sum_{i=0}^{N} D_{k,i} \tilde{\mathbf{q}}(\tau_i), \tag{3.95}$$

where $D_{k,i}$ are elements of the non-square matrix $D \in \mathbf{R}^{N \times (N+1)}$ called a *Gauss pseudospectral differentiation matrix*. See ref. [31–33] for more details. The performance cost in terms of τ is approximated using a Gauss quadrature as

$$J = \frac{t_f - t_0}{2} \sum_{k=1}^{N} w_k \big(\rho + (1-\rho) |\, \boldsymbol{u}(\tau_k)\,|\big), \tag{3.96}$$

where w_k are the Gauss weights. The above performance index together with constraints approximated by Eq. (3.93), lead to formulation of a nonlinear programming problem with the initial and final states, $\mathbf{q}(t_0) = \tilde{\mathbf{q}}(\tau_0)$ and $\mathbf{q}(t_f) = \tilde{\mathbf{q}}(\tau_f)$, respectively, which can be solved using the Sparse Nonlinear OPTimizer (SNOPT) solver.

3.6.3 Numerical Simulations

In this section, for two scenarios we present several numerical results including energy optimal and time optimal missions. The first scenario is assumed to have four attitude forbidden zones while the second scenario is assumed to have three attitude forbidden zones and one mandatory zone.

Scenario 1 (four attitude forbidden zones)

We consider a scenario in which the spacecraft is re-targeting its telescope while minimizing energy/time consumption and avoiding *four attitude forbidden zones* in the spacecraft rotational configuration space. The four attitude forbidden zones are randomly chosen, not overlapping with each other. Both initial and desired attitudes are randomly chosen in the *complement of attitude forbidden zones*, not violating the constrained zones as

$$\mathbf{q}_{t_0}^T M_{f_i} \mathbf{q}_{t_0} < 0 \quad \text{and} \quad \mathbf{q}_{t_f}^T M_{f_i} \mathbf{q}_{t_f} < 0, \quad i = 1, 2, 3, 4, \tag{3.97}$$

where $\mathbf{q}_{t_0}$ and $\mathbf{q}_{t_f}$ are the initial and desired unit quaternions, respectively. It has been assumed that the spacecraft carries a light-sensitive instrument with a fixed bore-sight in the spacecraft body axes, directed along the Z direction. Simulation parameters are given in Table 3.4.

Figs. 3.19 and 3.20 trace the geodesic pointing direction of the light-sensitive instrument on the celestial sphere as well as the same trajectory on the 2D cylindrical projection of the celestial sphere for the time and energy optimal case; on the other hand, Figs. 3.21-3.22 depict the non-geodesic rotations for the time and energy optimal case. The initial attitude is denoted by '$\circ$' and the desired attitude is denoted by '$\times$'. Figs. 3.23-3.26 exhibit the unit quaternions, angular velocities, control inputs and reaction wheel angular velocities over time. Note that the time optimal case terminates in about 14 seconds while the energy optimal case terminates in 20 seconds.

Scenario 2 (three attitude forbidden zones and one attitude mandatory zones)

In scenario 2, we examine a more complex reorientation maneuver keeping a fixed antenna bore-sight vector within a certain angle for continuous communication with the ground station while the spacecraft is re-targeting its light sensitive instrument avoiding multiple bright objects or constrained zones. For this scenario, the antenna has been aligned along the Z-axis while the sensitive instrument has been aligned along the Y-axis; We note that since this case includes a attitude mandatory zone as well as attitude forbidden zones, selecting the *right signed* unit quaternion for geodesic rotation plays a more crucial role than for the

J	`diag` [54, 63, 59] $kg \cdot m^2$		
J_r	`diag` [1, 0.8, 0.8] $kg \cdot m^2$		
Initial Attitude	[0.6085, -0.6300, -0.2369, -0.4204]		
Desired Attitude	[-0.0238, 0.7127, -0.2734, -0.6455]		
$\|\omega\|$	$\leq$ 0.3 rad/s		
$\|\omega_r\|$	$\leq$ 6 rad/s		
$\|u\|$	$\leq$ 2 rad/s^2		
t_f	$\leq 20s$		
Constrained object 1	[0.1632, -0.9863, 0.0250]	40 deg	Forbidden
Constrained object 2	[0.0734, 0.6938, 0.7164],	40 deg	Forbidden
Constrained object 3	[-0.5000, 0.6634, -0.5567],	30 deg	Forbidden
Constrained object 4	[-0.0677, -0.4628, -0.8839]	20 deg	Forbidden

Table 3.4: Case 1 simulation parameters

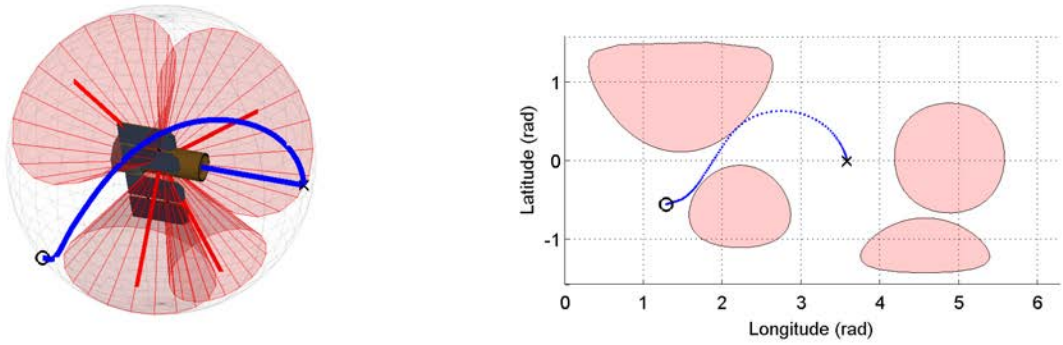

Figure 3.19: Geodesic: Target orientation is given by q_{t_f}. The corresponding trace of the telescope pointing direction on the celestial sphere and 2D cylindrical projection for the time optimal case are depicted. The circle and the cross indicate the directions of the initial and final orientations, respectively.

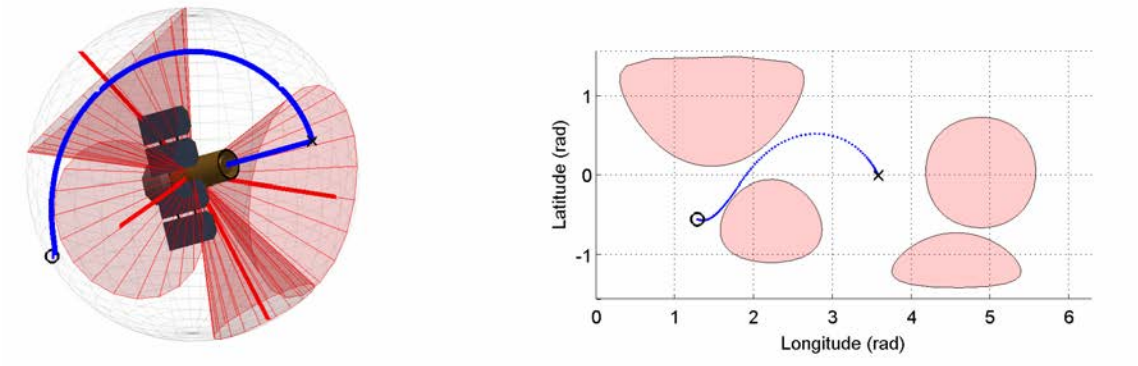

Figure 3.20: Geodesic: Target orientation is given by q_{t_f}. The corresponding trace of the telescope pointing direction on the celestial sphere and 2D cylindrical projection for the energy optimal case are depicted.

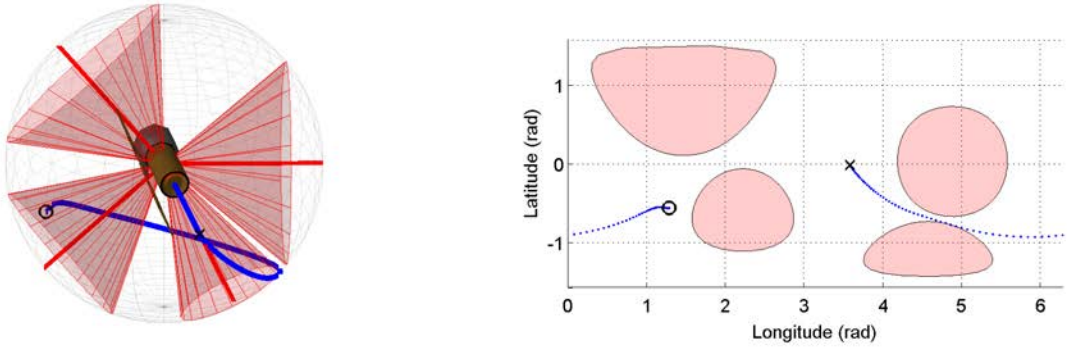

Figure 3.21: Non-geodesic: Target orientation is given by $-q_{t_f}$. The corresponding trace of the telescope pointing direction on the celestial sphere and 2D cylindrical projection for the time optimal case are depicted

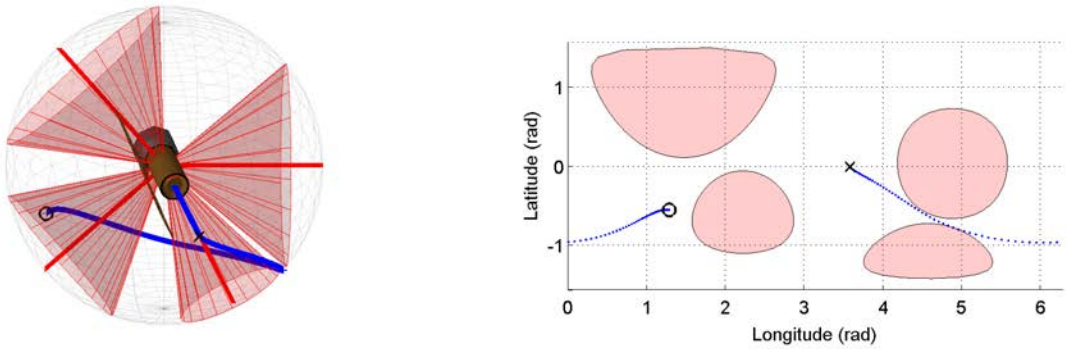

Figure 3.22: Non-geodesic: Target orientation is given by $-q_{t_f}$. The corresponding traces are depicted for the energy optimal case.

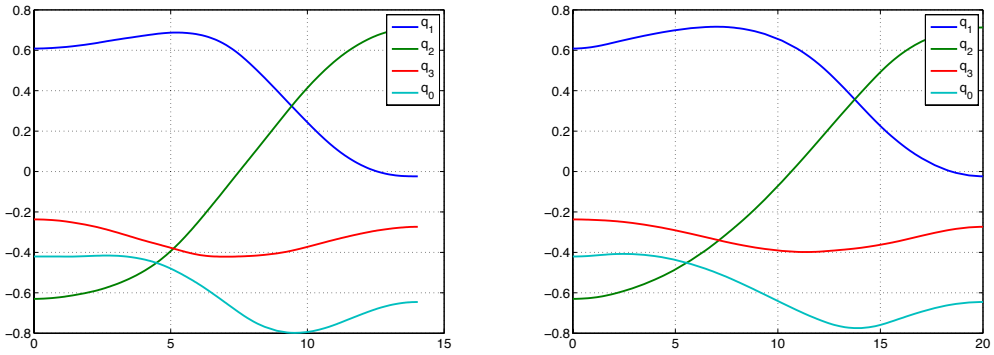

Figure 3.23: Unit quaternion trajectories for the time optimal (left) and energy optimal cases (right).

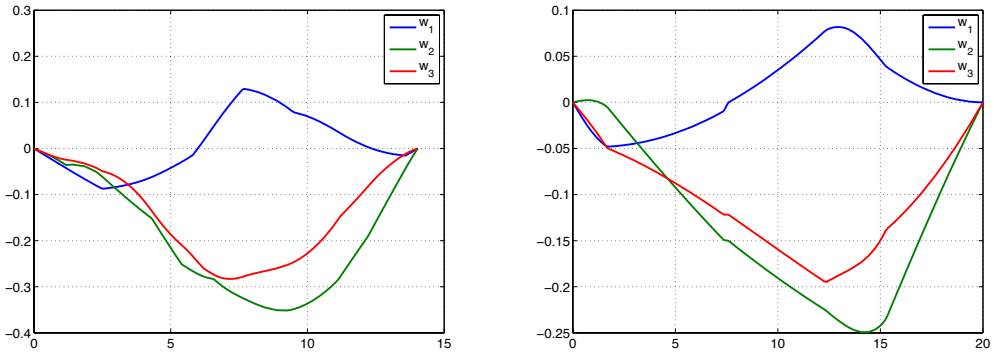

Figure 3.24: Spacecraft angular velocity trajectories for the time optimal (left) and energy optimal cases (right).

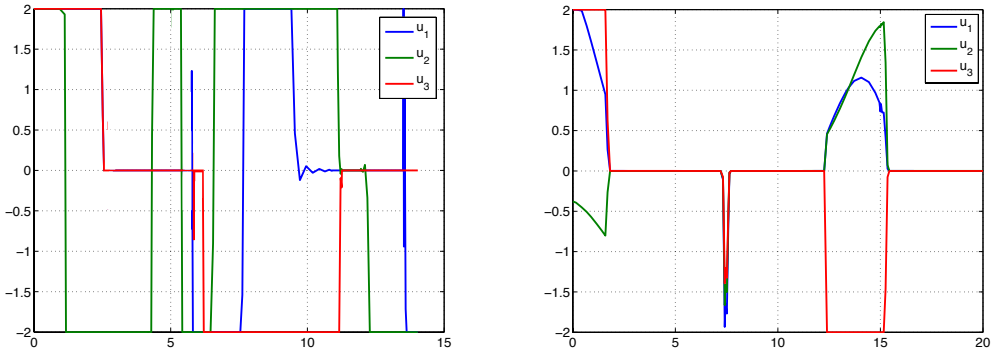

Figure 3.25: Control trajectories for the time optimal (left) and energy optimal cases (right).

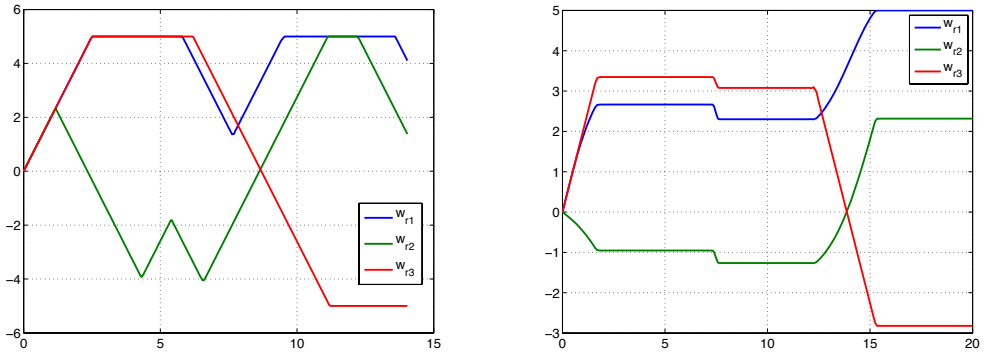

Figure 3.26: Reaction wheel angular velocitiy trajectories for the time optimal (left) and energy optimal cases (right).

first case; the non-geodesic rotation may not be able to reach the final orientation. The three attitude forbidden zones are randomly chosen, not overlapping with each other and both initial and desired attitudes are chosen not to violate the *complement of attitude forbidden zones* and *attitude mandatory zone* such that

$$\mathbf{q}_{t_0}^T M_{f_i} \mathbf{q}_{t_0} < 0 \text{ and } \mathbf{q}_{t_f}^T M_{f_i} \mathbf{q}_{t_f} < 0, \quad i = 1, 2, 3, \tag{3.98}$$

and

$$\mathbf{q}_{\boldsymbol{t_0}}^T M_m \mathbf{q}_{\boldsymbol{t_0}}^T > 0 \text{ and } \mathbf{q}_{\boldsymbol{t_f}}^T M_m \mathbf{q}_{\boldsymbol{t_f}}^T > 0. \tag{3.99}$$

Note that the set of physically feasible orientations is a subset in the configuration space that satisfies the above requirements. Figs. 3.27 and 3.28 demonstrate reorientation maneuvers while keeping the antenna's bore-sight vector within 70 degrees of the mandatory cone (black shaded area). The simulation parameters for this scenario are given in Table 3.5. Figs. 3.29-3.32 show the time histories for the quaternions, angular velocities, control inputs, and the reaction wheel angular velocities.

3.6.4 Concluding Remarks

In this section, quaternion-based energy and time optimal spacecraft reorientation in the presence of complex attitude constrained zones has been proposed. This has been achieved

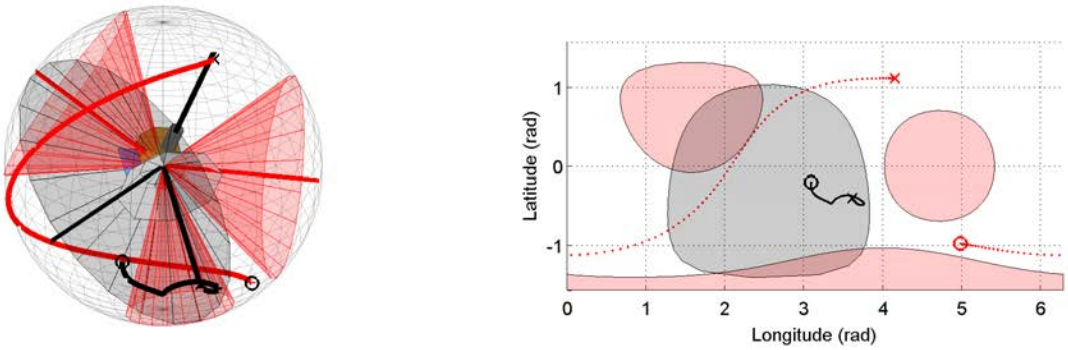

Figure 3.27: Geodesic: Target orientation is given by q_{t_f}. The corresponding trace of the telescope pointing direction on the celestial sphere (left) and 2D cylindrical projection for time optimal case (right).

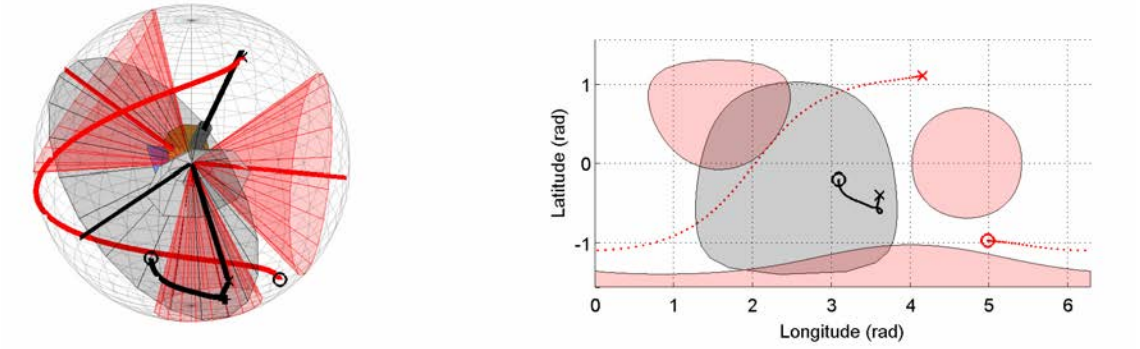

Figure 3.28: Geodesic: Target orientation is given by q_{t_f}. The trace of the telescope pointing direction on the celestial sphere (left) and 2D cylindrical projection for energy optimal case (right).

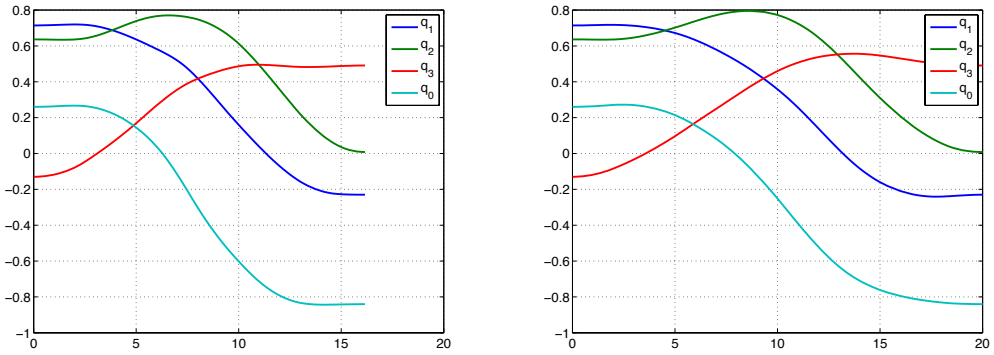

Figure 3.29: Uunit quaternion trajectories for time optimal (left) and energy optimal case (right).

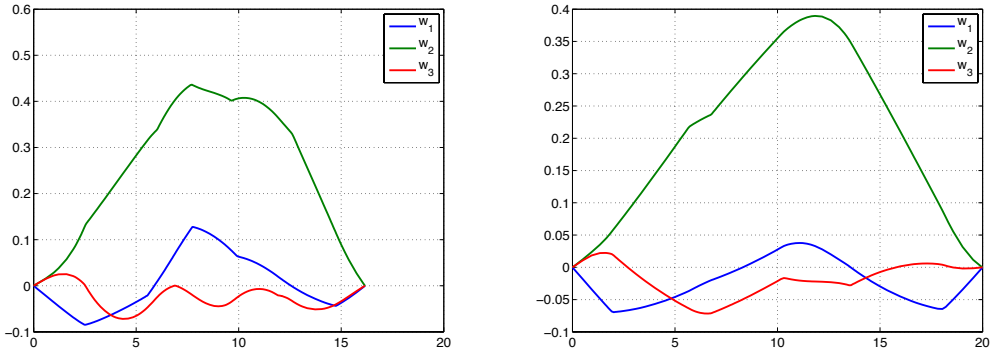

Figure 3.30: Spacecraft angular velocity trajectories for time optimal (left) and energy optimal case (right).

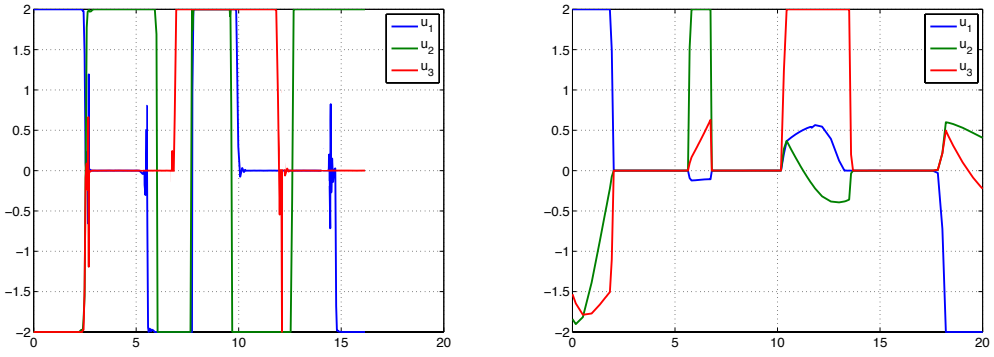

Figure 3.31: Control trajectories for time optimal (left) and energy optimal case (right).

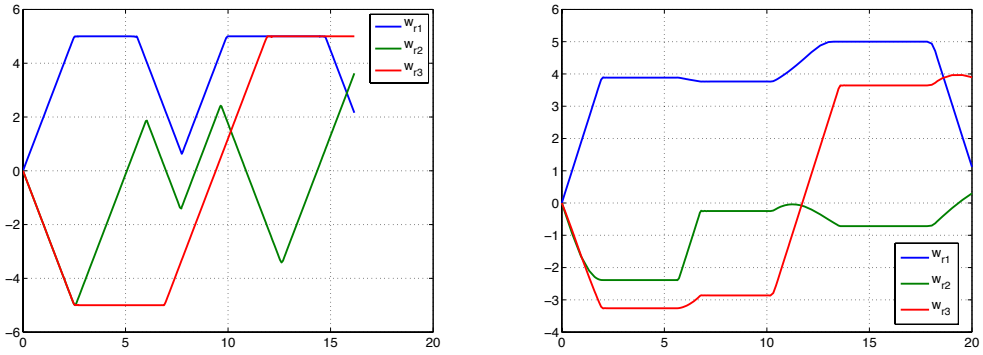

Figure 3.32: Reaction wheel angular velocitiy trajectories for time optimal (left) and energy optimal case (right).

J	`diag` [54, 63, 59] $kg \cdot m^2$
J_r	`diag` [1, 0.8, 0.8] $kg \cdot m^2$
Initial Attitude	[0.7143, 0.6365, -0.1300, 0.2602]
Desired Attitude	[0.2297, -0.0081, -0.4909, 0.8404]
$\|\omega\|$	$\leq$ 0.3 rad/s
$\|\omega_r\|$	$\leq$ 6 rad/s
$\|u\|$	$\leq$ 2 rad/s^2
t_f	$\leq 20s$

Constrained object 1	[-0.8138, 0.5483, -0.1926]	70 deg	Mandatory
Constrained object 2	[0, -1, 0],	40 deg	Forbidden
Constrained object 3	[0, 0.8192, 0.5736],	30 deg	Forbidden
Constrained object 4	[-0.1220, -0.1397, -0.9827]	20 deg	Forbidden

Table 3.5: Case 2 simulation parameters

via a Gauss pseudospectral method based on quaternion attitude constrained zone formulations. Ambiguity on geodesic/non-geodesic rotations has been discussed and a novel algorithm is presented. Extensive simulation results have been presented within two distinct scenarios to demonstrate the viability of the proposed methodology.

Chapter 4

ROTATIONALLY CONSTRAINED ATTITUDE SYNCHRONIZATION

In this chapter, we consider the problem of achieving identical orientation for a group of spacecraft in the presence of rotationally constrained zones. First, we address a consensus algorithm for attitude synchronization among multiple rigid bodies without attitude constraints. Then, we present a novel distributed constrained consensus algorithm operating under attitude constraints which are composed of rotationally forbidden zones. The proposed algorithm is guaranteed to reach an agreement on an orientation that lies at the intersection of individual convex constraint sets when the spacecraft network is connected.

4.1 Networked Dynamic Systems and Rigid-body Attitude Synchronization

During the past decade, networked dynamic systems have received significant attention from researchers across various fields of science and engineering, in the realm of collective behavior [18,57,74,88], multi-robot control [34,66,67], and attitude alignment [8,73,108,116]. The motivation for using networked systems in the space industry is their potential impact on system robustness, flexibility, and scalability. For example, it has been shown that the functionality of the overall space system could dramatically be improved by having distributed systems working together for a number of earth and space science missions [78].

Consensus type coordination algorithms have emerged as a convenient framework to reason about a number of issues surrounding distributed networked dynamic systems. Cooperative control laws among distributed systems using consensus-like protocols generally assume

that these systems are modeled as single or double integrators [34,66,88]. However, the problem of cooperative control for rigid bodies consists of intricate challenges that are mainly due to its inherent nonlinear dynamics. The fundamental aspects of spacecraft formations have been presented in Scharf *et al.* [78]. Recently, a few research works have investigated the relative attitude synchronization for a group of spacecraft [8, 73, 87, 91, 108, 109, 116]. In Lawton and Beard [8], for example, a behavioral approach has been utilized to maintain attitude alignment between a group of spacecraft interacting over a ring topology. The work [87] has extended this result for more general communication topologies. Moreover, the passivity approach has been adopted in Bai *et al.* [109] to derive a control law for the spacecraft formation without the angular velocity measurements, this work in principle assumes that consensus occurs on identical closed manifolds for connected network of agents.

In the following sections, we first develop a distributed algorithm for consensus of multiple agents in the presence of convex state constraints on the individual agent state. Each agent's state is assumed to be constrained in a distinct compact convex set. We then show that following the proposed distributed protocol, the agents are guaranteed to reach an agreement on a state that lies at the intersection of individual convex constraint sets. This modified consensus algorithm is applied to attitude synchronization in the presence of attitude constraints, where each spacecraft is required to stay away from pre-defined attitude forbidden zones while synchronizing their attitudes with others.

4.2 Multi-agent Framework

The communication topology of a multi-agent network is represented using a directed graph $\mathcal{G}$, e.g., in such a graph an agent i can transmit information to agent j when the link $i \to j$ is present in the graph. A directed graph $\mathcal{G}$ is represented as a pair $\mathcal{G} = (V, E)$, where V is a finite nonempty set of agents as $V = \{v_1, v_2, \ldots, v_n\}$ and E is referred as the set of directed edges of $\mathcal{G}$ and denoted as $E = \{e_1, e_2, \ldots e_m\}$. An element of E, e.g., $e_k \in E$, consists of pairs of distinct agents as (v_i, v_j) which implies that e_k is directed from v_i to v_j. Here, v_i is the initial vertex edge (tail) and v_j is the terminal edge (head). Analogously, the neighbors

of the jth agent are denoted by

$$\mathcal{N}_j = \{v_j \in V \,|\, \{v_i,\, v_j\} \in E\}\,,$$

and implies a group of agents which transmit information to the jth agent. The graph $\mathcal{G}$ is connected if for every pair of distinct agents in V, there is a path that has them as its end agents. The graph $\mathcal{G}$ can be specified in terms of matrices. These specifications provide far more efficient ways of representing a large and complicated graph than pictorial representation [20]. Under the assumption that labels have been associated with the edges in a graph, arbitrarily oriented, the $n \times m$ incidence matrix $D(\mathcal{G})$ is defined as

$$D = [d_{ij}],\ \text{where } d_{ij} = \begin{cases} -1 & \text{if } v_i \text{ is the tail of } e_j \quad \text{[out-degree]} \\ 1 & \text{if } v_i \text{ is the head of } e_j \quad \text{[in-degree]} \\ 0 & \text{otherwise.} \end{cases}$$

The advantage of using an incidence matrix over an adjacency representation is that it holds the orientation (vector) of the connection between two agents. The constrained consensus algorithm proposed in this paper is equally applicable to weighted graphs.

Definition 4.1 (Strongly connected)**.** *A directed graph is called* ***strongly connected*** *if there is a path in each direction between each pair of vertices of the graph. In a directed graph G that may not itself be strongly connected, a pair of vertices u and v are said to be strongly connected to each other if there is a path in each direction between them.*

Definition 4.2 (Balanced)**.** *A directed graph is called a balanced if for every node $v \in V$, the number of in-degree edges is equal to the number of out-degree edges. Namely,*

$$\mathbf{1}^T D = 0. \tag{4.1}$$

Another matrix representation of a graph $\mathcal{G}$, used in this paper, is the graph Laplacian, $L(\mathcal{G})$. The symmetric Laplacian matrix which is defined as $L(\mathcal{G}) = DD^T$ holds the connection information among pairs of agents. This matrix is a positive semi-definite matrix and has eigenvalues that can be ordered as

$$\lambda_1(\mathcal{G}) \leq \lambda_2(\mathcal{G}) \leq \cdots \leq \lambda_n(\mathcal{G}), \tag{4.2}$$

where $\lambda_1(\mathcal{G}) = 0$. The graph $\mathcal{G}$ is connected if and only if $\lambda_2(\mathcal{G}) > 0$ [21]. The weighted graph Laplacian associated with the weighted graph $\mathcal{G} = (V,\ E,\ w)$ can be formed as

$$L_w = \frac{1}{2}\ DWD^T, \tag{4.3}$$

where W is a diagonal matrix whose elements consist of the numeric weights $w(e_j)$ corresponding to an edge e_j. It is well-known that $\lambda_2(\mathcal{G}) > 0$ still holds valid for weighted connected graphs as long as the weights are positive.

4.3 Constrained Consensus Algorithm

The constrained consensus problem has been examined in a handful of recent research works. In this venue, Moore *et al.* [58] have examined the constrained consensus when a subset of state variables are constrained. In Nedic *et al.* [81], the authors have proposed a framework for the constrained consensus by utilizing a projection algorithm and presented its convergence properties. The projection algorithm [24] provides means by which one can determine the state's closeness to a set defined by linear constraints, which in turn, can be parameterized using measures on an appropriate function space.

In this section, we present a constrained consensus algorithm framework where the agents values are constrained to be in convex sets and each agent is only aware of its own constrained set. This algorithm is based on the log barrier potential initially proposed in previous chapter, in this chapter we augment the unique properties of this potential to address the constrained consensus problem.

4.3.1 Log Barrier potential

Proposition 4.1. *The function* $J : x, x_r \in \mathbf{int}(\mathcal{D}_x) \to \mathbb{R}$,

$$J(x) = \|x_r - x\|^2\big[-\log\big(\frac{f(x)}{e^2\beta}\big)\big], \tag{4.4}$$

where

$$\mathcal{D}_x = \{x \in \mathbb{R}^m \mid f(x) \leq 0\}, \tag{4.5}$$

is a strictly convex function on $\mathbf{int}(\mathcal{D}_x)$ *and has a globally unique minimum at* $x = x_r$ *as it meets the following requirements:*

1. *$f(x) : \mathbb{R}^m \to \mathbb{R}$ is continuous and at least double differentiable,*

2. *$f(x)$ is convex on $x \in \mathcal{D}_x$,*

3. *$\mathcal{D}_x$ is closed and there exists a negative lower bound β for all $x \in \mathcal{D}_x$ as $\beta \leq f(x)$.*

Proof. First, it is easy to see $J(x_r) = 0$ and from the requirement (3), we have

$$0 < \frac{f(x)}{e^2\beta} < 1, \quad \forall x \in \mathbf{int}(\mathcal{D}_x), \tag{4.6}$$

where $\mathbf{int}(\mathcal{D}_x)$ denotes interior points of $\mathcal{D}_x$. Thus $J(x) > 0$ for all $x \in \mathbf{int}(\mathcal{D}_x) \backslash \{x_r\}$. The Hessian is calculated as:

$$\begin{aligned} \nabla^2 J = & -2\log(\frac{f(x)}{e^2\beta}) + \frac{4}{f}(x_r - x)\frac{\partial f}{\partial x}^T \\ & + \frac{1}{f^2}\|x_r - x\|^2 \frac{\partial f}{\partial x}\frac{\partial f}{\partial x}^T + \|x_r - x\|^2 \frac{1}{-f}\nabla^2 f. \end{aligned} \tag{4.7}$$

Let

$$p(x_r, x) = \frac{1}{f}(x_r - x)\frac{\partial f}{\partial x}^T, \tag{4.8}$$

then it follows by

$$\nabla^2 J = p^T p + 4p + m(\beta), \tag{4.9}$$

where

$$m(\beta) = -2\log(\frac{f(x)}{\beta}) + 4 + \|x_r - x\|^2 \frac{1}{-f}\nabla^2 f > 4. \tag{4.10}$$

Note that $-2\log(1/e^2) = 4$ and the convexity of $f(x)$ as well as a double differentiable properties guarantee $m(\beta) > 4$ in Eq.(4.10). Then, the quadratic equation Eq.(4.9) becomes positive. Therefore, for all $p(x_r, x)$, $\nabla^2 J$ is positive definite and V is smooth and strictly convex. □

Consider the case $x_r \notin \mathcal{D}_x$ in preceding proposition. Still the function $J(x)$ satisfies all requirements and is strictly convex, but it reaches a global minimum where $\|x_r - x\|$ is non-zero. This can be considered as a *weighted projection.*

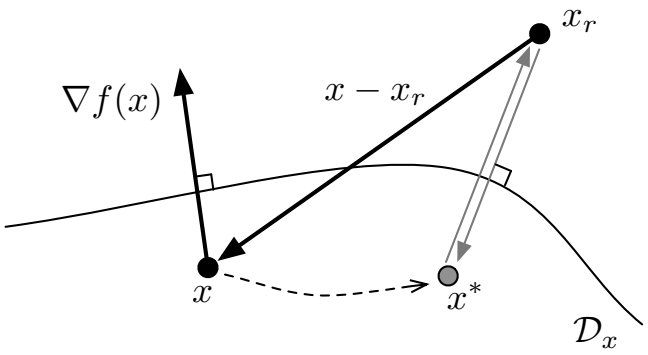

Figure 4.1: Illustration of the location of x^* in the case where $x_r \notin \mathcal{D}_x$ in Proposition 4.2. When V is at global minimum($x = x^*$), the sum of two vectors, $(x - x_r)$ and ∇f becomes zero.

Proposition 4.2. *For $x_r \notin \mathcal{D}_x$ and $x \in \mathbf{int}(\mathcal{D}_x)$, $J(x)$ in Proposition 4.1 has a globally unique minimum that lies on the line passing x_r and the projection point of x_r toward the $\mathcal{D}_x$ (closest point in $\mathcal{D}_x$). See Fig. 4.1 for an illustration.*

Proof. Since J is strictly convex in x, at its minimum, it holds that

$$\nabla J = -2\log\big(\frac{f}{e^2\beta}\big)[x - x_r] + \frac{\|x_r - x\|^2}{-f(x)}[\nabla f] \tag{4.11}$$

$$= \gamma_1[x - x_r] + \gamma_2[\nabla f] = 0. \tag{4.12}$$

The fact that $-f(x)$ is positive implies that the two vectors $[x - x_r]$ and $[\nabla f]$ always have positive multipliers, *i.e.*, γ_1 and γ_2. Therefore, when $J(x)$ is at the globally unique minimum ($x = x^*$), the only way it can have a vanishing gradient is that the sum of two vectors become zero from Eq. (4.12) where x^* lies on the line passing x_r and the projection point toward $\mathcal{D}_x$ as depicted in Fig. (4.1). Note that Eq. (4.11) implies that γ_1 and γ_2 are continuous and bounded for all $x \in \mathbf{int}(\mathcal{D}_x)$. This implies the following relations:

$$x \to \partial\mathcal{D}_x \quad \Longleftrightarrow \quad f(x) \to 0 \quad \Longleftrightarrow \quad \gamma_1, \gamma_2 \to \infty. \tag{4.13}$$

Therefore, the globally unique x^* as well as its transition trajectory from an initial x always stay in the interior of $\mathcal{D}_x$. □

The preceding two propositions can be generalized when the closed convex set D_x is expressed by a finite number of convex functions, e.g., a polyhedra.

Proposition 4.3. *The compact convex set $\mathcal{D}_x$ can be represented by zero sub-level sets of p convex functions $f_{i,k} : \mathbf{R}^m \to \mathbf{R}$ defined as*

$$\mathcal{D}_x \doteq \{x \in R^m \,|\, f_1(x) \leq 0, \ldots, f_p(x) \leq 0\}. \tag{4.14}$$

Additionally, we define a shift parameter β_i which is obtained from a minimum of the kth convex function as

$$\beta_i = \min_x f_k(x), \quad x \in \mathcal{D}_{x_i}, \tag{4.15}$$

where $k = 1, ..., p$. With the newly defined $\mathcal{D}_x$, the extended log barrier potential is given as

$$J = \|x_r - x\|^2 \Big[\sum_{k=1}^{p} -\log\big(\frac{f_k(x)}{e^2 \beta_k}\big)\Big]. \tag{4.16}$$

Then, Propositions 4.1 and 4.2 are still valid for Eq. (4.16).

Proof. All properties are preserved from a regular log barrier potential since the sum of strictly convex functions is also strictly convex [101]. □

4.3.2 Potentials for the Canonical Consensus Algorithm

Under the assumption that the communication topology is strongly connected and balanced, the *ith* agent in a connected network can be considered to have a local potential function J_i representing the disagreement of shared variables from its neighbors as

$$J_i = \sum_{i,j \in E} \alpha_{ij} \|x_j - x_i\|^2. \tag{4.17}$$

Then, the total potential [68] is given as

$$J = \sum_i J_i = \frac{1}{2} \sum_i \sum_{i,j \in E} \alpha_{ij} \|x_j - x_i\|^2 \tag{4.18}$$

$$= \frac{1}{2} \boldsymbol{x} D W D^T \boldsymbol{x} = \boldsymbol{x}^T L_w \boldsymbol{x}, \tag{4.19}$$

where $\boldsymbol{x}$ denotes the stack of vectors $x_i \in \mathbf{R}^m$, and L_w denotes a weighted graph Laplacian associated with positive weights a_{ij} acting on the respective edge. The assumption that all agents are strongly connected and balanced assures that L_w is positive semidefinite

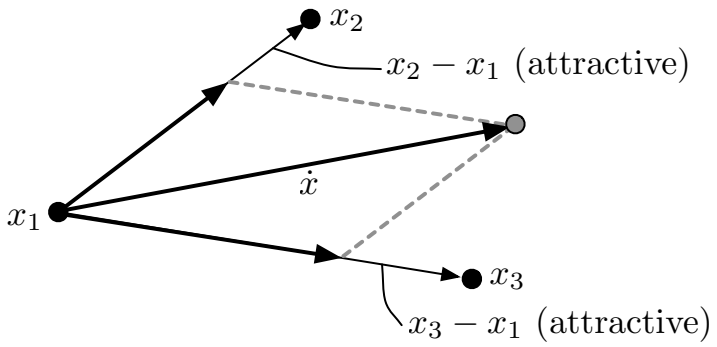

Figure 4.2: Geometric illustration of the vector $\dot{x}_1$ from canonical consensus algorithm in the presence of two neighbors

and convex in $\boldsymbol{x}$ [21]. Furthermore, Eq.(4.19) uniquely vanishes at $\boldsymbol{x} = \alpha\mathbf{1}$. By utilizing these facts, the canonical consensus algorithm can be represented as the flow following the negative gradient of the total potential function J. Taking a negative gradient of Eq. (4.19) gives

$$\dot{\boldsymbol{x}} = -\nabla J, \tag{4.20}$$

or component-wise,

$$\dot{x}_i = \sum_{i,j \in E} a_{ij}(x_j - x_i). \tag{4.21}$$

This consensus algorithm leads x_i to the agreement subspace

$$\mathcal{A} = \{x \in \mathbf{R}^m | x_i = x_j\}, \text{ for all } i, j, \tag{4.22}$$

due to the fact that the $\boldsymbol{Null}(L_w)$ is only spanned by $\alpha\mathbf{1}$. Geometrically speaking, the algorithm provides a weighted directional derivative for the agents' state as a function of its relative states with its neighbors as illustrated in Fig. 4.2. Thus, it is intuitive that this algorithm leads to a consensus on the weighted average of the agents' initial states. In non-weighted case, the consensus value is given by $\frac{\boldsymbol{x}(0)^T\mathbf{1}}{n}\mathbf{1}$ [21].

Remark 4.1. *Aforementioned consensus algorithm is still valid on undirected communication topology since the connected network in the assumption with undirected links is strongly connected and balanced from a directed link perspective.*

4.3.3 Constrained Consensus Algorithm

In this section, we introduce a continuous constrained consensus algorithm. First, under directed links, there are n agents in the strongly connected and balanced network, and we consider each agent having a log barrier potential with x_r representing its neighbor's state

$$x_r \to x_j, \quad i, j \in E \tag{4.23}$$

where E is a strongly connected and balanced edge set in the graph $\mathcal{G}$. For each agent, the logarithm part are defined differently based on the shape of the convex sets. In order to deal with a log barrier potential seamlessly, let us define g_i to the ith agent's logarithm part.

Log barrier potential g : The log barrier potential for the ith agent is defined by

$$g_i = -\log\Big(\frac{f_i(x)}{e^2\beta_i}\Big). \tag{4.24}$$

Then, Eq. (4.16) is rewritten for the ith agent by

$$J_i = \|x_j - x_i\|^2 g_i. \tag{4.25}$$

Analogously to *the Canonical Consensus Algorithm*, the total potential is given by the summation of local potentials $J : \boldsymbol{x} \to \boldsymbol{R}$

$$J = \sum_i J_i = \sum_i \sum_{i \leftarrow j} \frac{1}{2}\|x_j - x_i\|^2 g_i, \tag{4.26}$$

where $\boldsymbol{x} = [\, x_1, ..., x_n \,]^T$.

Proposition 4.4. *The total cost function J given in Eq. (4.26) is positive semi-definite and convex in $\boldsymbol{x}$. Thus, it has a globally unique minimum at zero, which is spanned by the subspace $\mathcal{A}$,*

$$\mathcal{A} = \{x \in \mathbf{R} \mid x_i = x_j\}, \text{ for all } i, j \tag{4.27}$$

where $\boldsymbol{x} = [\, x_1, ..., x_n \,]^T$ when the following requirements are met:

1. *The network is strongly connected and balanced.*

2. The set which intersects all domains $\mathcal{D}_{x_i}$ is nonempty, i.e.,

$$\bigcap_{i=1}^{n} \mathcal{D}_{x_i} \neq \emptyset.$$

Proof. The proof is based on the fact that the potential function J can be made to be convex in $\boldsymbol{x}$ by having appropriate values for β_i in g_i in Eq.(4.24). When the network is strongly connected and balanced, the potential function Eq. (4.26) can be represented in terms of the incidence matrix D as

$$\begin{aligned} J = \sum_i J_i &= \sum_i \sum_{i \leftarrow j} \frac{1}{2} \|x_j - x_i\|^2 g_i \\ &= \frac{1}{2} \boldsymbol{x}^T D W D^T \boldsymbol{x} \qquad (4.28) \\ &= \frac{1}{2} \boldsymbol{x}^T L \boldsymbol{x}, \qquad (4.29) \end{aligned}$$

where D denotes the incidence matrix representing the strongly connected and balanced network in $\mathcal{G}$. The matrix W denotes a $m \times m$ diagonal matrix where m designates the number of all edges in the graph $\mathcal{G}$. We assume that all edges are ordered by the agents, and the weighting matrix W has the form

$$W = \texttt{diag}(g_1, ..., g_1, \underbrace{g_2, ..., g_2}, ..., g_n, ..., g_n). \qquad (4.30)$$

Number. of in-degree edges for the second agent

Note that W is a positive definite matrix. The potential in Eq.(4.29) can be viewed as disagreement between agents in the network with state dependent weights.

First, W is full rank since its a positive diagonal matrix. Its positive definiteness is assured when all states x_i stay within their convex sets for all time by Eq.(4.24). Likewise, if we consider the potential's global minimum is only spanned by the agreement subspace $\mathcal{A}$, it is a natural to conclude that on agreement, W should not be infinity, which implies that the set of intersection of all domains $\mathcal{D}_{x_i}$ should nott empty.

For the balanced network, D^T has rank $n-1$ and its null space is spanned by $\alpha\mathbf{1}$ [21]. The rank property [79] assures that the rank of DWD^T is $n-1$ and the null space is uniquely spanned by $\mathbf{1}$ vector. Therefore, the potential J is semi-positive definite when the

network is connected as

$$J = \boldsymbol{x}^T [DWD^T]\boldsymbol{x} > 0, \quad \forall x \in \boldsymbol{A}^{\perp} \tag{4.31}$$

where

$$\mathcal{A}^{\perp} \stackrel{\text{def}}{=} \mathbb{R} \setminus \mathcal{A} = \{x \in \boldsymbol{R} | x \notin \mathcal{A}\}. \tag{4.32}$$

The minimum of J is contained in the set

$$\{x \in \mathbb{R}^n \,|\, J = 0\} = \mathcal{A}, \tag{4.33}$$

which in turn, is exactly the null space of the graph Laplacian L. Moreover, the gradient of Eq. (4.28) with respect to $\boldsymbol{x}$ is calculated as

$$\nabla J = 2[DWD^T]\boldsymbol{x} + \begin{bmatrix} \boldsymbol{x}^T D \frac{\partial W}{\partial x_1} D^T \boldsymbol{x} \\ \vdots \\ \boldsymbol{x}^T D \frac{\partial W}{\partial x_n} D^T \boldsymbol{x} \end{bmatrix}, \tag{4.34}$$

where we adopt the notation $\frac{\partial}{\partial x_i} W$ that denotes the partial differentiation of the diagonal components of the matrix W with respect to x_i, e.g.,

$$\frac{\partial W}{\partial x_2} = \texttt{diag}(0, ..., 0, \frac{\partial g_2}{\partial x_2}, ..., \frac{\partial g_2}{\partial x_2}, 0, ..., 0). \tag{4.35}$$

Note that g_i is only a function of x_i. Thus, the gradient terms with respect to other states vanish. The Hessian of Eq. (4.28) is given as

$$\begin{aligned} \nabla^2 J = {} & 2[DWD^T] \\ & + 2 \begin{bmatrix} D \frac{\partial W}{\partial x_1} D^T \boldsymbol{x} & \cdots & D \frac{\partial W}{\partial x_n} D^T \boldsymbol{x} \end{bmatrix} \\ & + 2 \begin{bmatrix} \boldsymbol{x}^T D \frac{\partial W}{\partial x_{1,1}} D^T \\ \vdots \\ \boldsymbol{x}^T D \frac{\partial W}{\partial x_n} D^T \end{bmatrix} + \texttt{diag}\Big(\boldsymbol{x}^T D \frac{\partial^2 W}{\partial \boldsymbol{x}_i^2} D^T \boldsymbol{x}\Big). \end{aligned} \tag{4.36}$$

Consequently,

$$\begin{aligned} & \boldsymbol{x}^T \nabla^2 J \boldsymbol{x} \\ & = \sum_i \sum_{i \leftarrow j} \|x_j - x_i\|^2 \Big[g_i + 2 x_i^T \nabla g_i + \frac{1}{2} x_i^T \nabla^2 g_i x_i \Big], \end{aligned} \tag{4.37}$$

where

$$\nabla g_i = -\frac{1}{f_i}\frac{\partial f_i}{\partial x_i}, \quad \nabla^2 g_i = \frac{1}{f_i^2}\left\|\frac{\partial f_i}{\partial x_i}\right\|^2 - \frac{1}{f_i}\frac{\partial^2 f_i}{\partial x_i^2}. \tag{4.38}$$

Let

$$p_i = -\frac{1}{f_i}x_i^T\frac{\partial f_i}{\partial x_i}. \tag{4.39}$$

Then, Eq. (4.37) gives

$$\begin{aligned}&\boldsymbol{x}^T\nabla^2 J\boldsymbol{x}\\ &= \sum_i \sum_{i,j\in E} \|x_j - x_i\|^2 \left[g_i + 2p_i + \frac{1}{2}\|p_i\|^2 + \frac{1}{2}\frac{1}{-f_i}x_i^T\frac{\partial^2 f_i}{\partial x_i^2}x_i\right].\end{aligned} \tag{4.40}$$

Similar to Eq. (4.9), defining g_i in Eq. (4.24) we have

$$\frac{1}{2}\|p_i\|^2 + 2p_i + g_i \geq 0 \tag{4.41}$$

and the fact that $f_i(x)$ is a convex and $f_i(x) < 0$ assure the rest of the Hessian is positive as

$$\frac{1}{2}\frac{1}{-f_i}x_i^T\frac{\partial^2 f_i}{\partial x_i^2}x_i \geq 0. \tag{4.42}$$

Thus, we have shown that

$$\nabla^2 J \geq 0. \tag{4.43}$$

□

Analogous to the *Canonical consensus algorithm*, the agreement protocol for the *Constrained consensus algorithm* is simply represented by the flow following the negative gradient of the total cost function Eq. (4.26) as

$$\dot{\boldsymbol{x}} = -\nabla J \tag{4.44}$$

$$= -2[DWD^T]\boldsymbol{x} - \begin{bmatrix} \boldsymbol{x}^T D\frac{\partial W}{\partial x_1}D^T\boldsymbol{x} \\ \vdots \\ \boldsymbol{x}^T D\frac{\partial W}{\partial x_n}D^T\boldsymbol{x} \end{bmatrix}, \tag{4.45}$$

where $\boldsymbol{x} = [\, x_1, ..., x_n \,]^T$ and we adopt the notation

$$\frac{\partial W}{\partial x_i} \tag{4.46}$$

that denotes the partial differentiation of the diagonal components of the matrix W with respect to x_i for notational brevity. Thus we have component-wise,

$$\dot{x}_i = \sum_{i,j \in E} 2(g_i + g_j)[x_j - x_i] + \|x_j - x_i\|^2 \, [-\nabla g_i], \tag{4.47}$$

where g_j denotes a connected neighbor's log barrier potential as

$$g_j = -\log\Big(\frac{f_j(x)}{e^2 \beta_j}\Big). \tag{4.48}$$

Note that ith agent does not need to know the corresponding convex function for the jth agent, e.g., $f_j(x_j)$, since ith agent is only required to know x_j and g_j transmitted its connected neighbors.

Proposition 4.5. *The protocol Eq. (4.47) asymptotically leads all state variables x_i in the strongly connected and balanced network $\mathcal{G}$ to the agreement subspace $\mathcal{A}$,*

$$\mathcal{A} = \{x \in \mathbf{R}] \mid x_i = x_j\}, \ \textit{for all } i, j. \tag{4.49}$$

Proof. Consider Eq. (4.29) as a Lyapunov function candidate. By the proposed protocol Eq. (4.47), the time derivative of J is given as

$$\dot{J} = -\|\nabla J\|^2 \leq 0, \tag{4.50}$$

and it is a weak Lyapunov function since it vanishes when the stacked state $\boldsymbol{x}$ is spanned by $\mathbf{1}$ due to the fact that $D^T\mathbf{1} = 0$ for the connected graph in Eq. (4.45). Let $S = \{\boldsymbol{x} \in R^n | \dot{J} = 0\}$. Then, $\dot{J}(\boldsymbol{x}) = 0 \iff D^T\boldsymbol{x} = 0 \iff J(\boldsymbol{x}) = 0$. Moreover, as $\boldsymbol{x} \to \infty$, $J(\boldsymbol{x}) \to \infty$. Therefore, the set S is the largest invariant set including $\boldsymbol{x}$ such that $J(\boldsymbol{x}) = 0$, and we conclude that by LaSalle's invariance principle [49], the invariant set S where

$$\{\boldsymbol{x} \in \mathbf{R}^n \,|\, J(\boldsymbol{x}) = 0\} \iff \{\boldsymbol{x} \in \mathbf{R}^n \,|\, \boldsymbol{x} = \alpha\mathbf{1}\} \tag{4.51}$$

is globally asymptotically stable. □

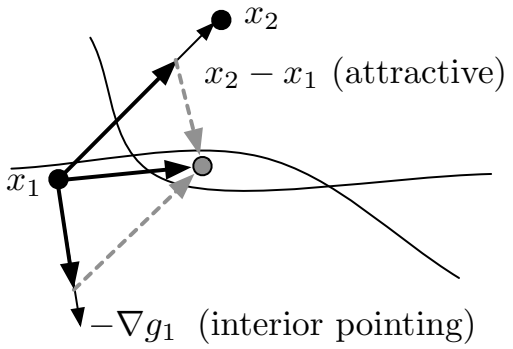

Figure 4.3: Geometric illustraion of the vector $\dot{x}_i$ from constrained consensus algorithm in the presence of one neighbor x_2

Getting back to the constrained consensus protocol, we note that the constrained consensus protocol can be partitioned by repulsive and attractive components as

$$\dot{x}_i = \sum_{i,j \in E} \underbrace{2(g_i + g_j)[x_j - x_i]}_{\text{attractive}} + \underbrace{\|x_j - x_i\|^2 [-\nabla g_i]}_{\text{repulsive}} \tag{4.52}$$

where $2(g_i + g_j)$ and $\|x_j - x_i\|^2$ are always positive. As illustrated in Fig. 4.3, the repulsive component provides an "interior pointing" vector, acting normal to its domain's boundary, while the attractive component guides the agents states toward consensus. From its structure, this also can be viewed as an agreement protocol on a state dependent network. In fact, Eq. (4.47) reduces to

$$\dot{x}_i = \sum_{i \leftarrow j} \alpha_{i,j}(\boldsymbol{x}_j - \boldsymbol{x}_i) \tag{4.53}$$

$$= -DW'D^T\boldsymbol{x} \tag{4.54}$$

where $\alpha_{i,j} = 2(g_i + g_j) - (x_j - x_i)^T \nabla g_i$ and denotes a state dependent weight on a directed edge $i \to j$.

Lemma 4.6. *Adding edges to any strongly connected and balanced graph $\mathcal{G} = (V,\ E)$ can be expressed as an addition of two incident matrices D associated with a strongly connected*

graph and edges respectively;

$$D'(\mathcal{G}) = D(\mathcal{G}) + D(\mathcal{G}_{edge}), \ \ or \tag{4.55}$$

$$D'_{>0}(\mathcal{G}) = D(\mathcal{G}) + D(\mathcal{G}_{edge}) \tag{4.56}$$

which result in

$$\mathcal{L}'(\mathcal{D}) = \mathcal{L}(\mathcal{D}) + \mathcal{L}(\mathcal{D}_{edge}) \tag{4.57}$$

where $\mathcal{D}_{tree} = (V,\ E_1)$, $\mathcal{D}_{edge} = (V,\ E_2)$, *and* $E(\mathcal{D}) = E_1 \cup E_2$.

Proof. See [21]. □

Proposition 4.7. *The convergence rate of the constrained consensus protocol Eq. (4.47) is governed by Eq. (4.50), which reaches the minimum of J when the connection is strongly connected and balanced minimally. This rate of convergence may be improved by adding an extra edge.*

Proof. According to *Lemma* 4.6, we rewrite Eq. (4.50) with Eq. (4.54) as

$$\dot{J} = -\|\nabla J\|^2 \tag{4.58}$$

$$= -\boldsymbol{x}^T \mathcal{L}^T \mathcal{L} \boldsymbol{x} \tag{4.59}$$

Plugging Eq. (4.55)-(4.56) into the above equation leads to

$$\begin{aligned} \dot{J} &= -\boldsymbol{x}^T (\mathcal{L}' - \mathcal{L}_e)^T (\mathcal{L}' - \mathcal{L}_e) \boldsymbol{x} \\ &= -\boldsymbol{x}^T \mathcal{L}'^T \mathcal{L}' \boldsymbol{x} - \boldsymbol{x}^T \mathcal{L}_e^T \mathcal{L}_e \boldsymbol{x} + \boldsymbol{x}^T (\mathcal{L}'^T \mathcal{L}_e + \mathcal{L}_e^T \mathcal{L}') \boldsymbol{x} \\ &= \dot{J}' + \dot{J}_{edge} + \mathcal{O}^2, \end{aligned} \tag{4.60}$$

where we know $\dot{J}_{edge}$ is non-negative; moreover $\mathcal{O}^2$ is non-negative as $\mathcal{L}'^T \mathcal{L}_e$ and $\mathcal{L}_e^T \mathcal{L}'$ are positive semi-definite. Thus, we conclude that

$$\dot{J}' \leq \dot{J}, \tag{4.61}$$

This completes the proof. □

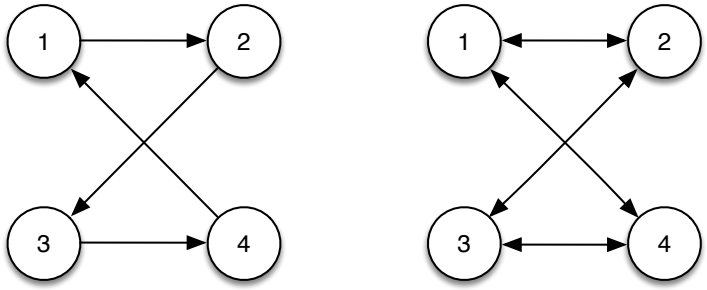

Figure 4.4: Two strongly connected and balanced communication topologies $\mathcal{G}_1$ and $\mathcal{G}_2$ for 4 UAVs

4.3.4 Example with Single Integrators

In this section, we present a simulation result for the application of the constrained consensus algorithm. One of practical applications for the proposed algorithm is the initialization of unmanned aerial vehicles (UAV) formation flying. In this simulation, each UAV is represented via its kinematic model as a single integrator. Furthermore, it is assumed that there are four UAVs in the formation. Each UAV takes off from its corresponding ground station, whose remote control coverage set is described by a convex set defined as the domain of a known convex function. Two strongly connected and balanced communication topologies, given as graphs $\mathcal{G}_1$ and $\mathcal{G}_2$ respectively, are shown in Fig. 4.4. The remote control coverage sets are shown in Table 4.1 and $\beta_{i,k}$ are chosen in order to satisfy the condition in *Proposition* 4.1 as in Table 4.2. The simulation results are illustrated in Figs. 4.5-4.6. Fig. 4.5 depicts the trajectory of each UAV as well as the initial position ($\times$ mark) and the final position ($\circ$ mark) in black. Note that the unfilled square denotes the final position when unconstrained. Fig. 4.6 and Fig. 4.6 show, respectively, the state evolution histories for $\mathcal{G}_1$ and $\mathcal{G}_2$. Note that in both cases consensus is asymptotically reached, but the convergence rate for $\mathcal{G}_2$ is faster. The final state attained by the agents depends on the initial conditions and state dependent weights acting on the edges of the communication graph as well as the shape of the respective convex sets defining each agent's remote control converge constrained set.

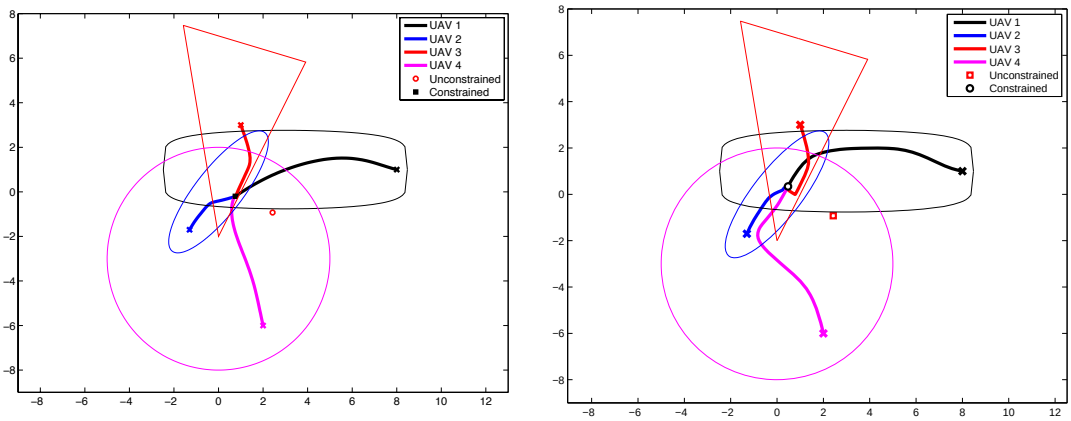

Figure 4.5: UAV trajectories with $\mathcal{G}_1$ (left) and $\mathcal{G}$ (right) on 2D space

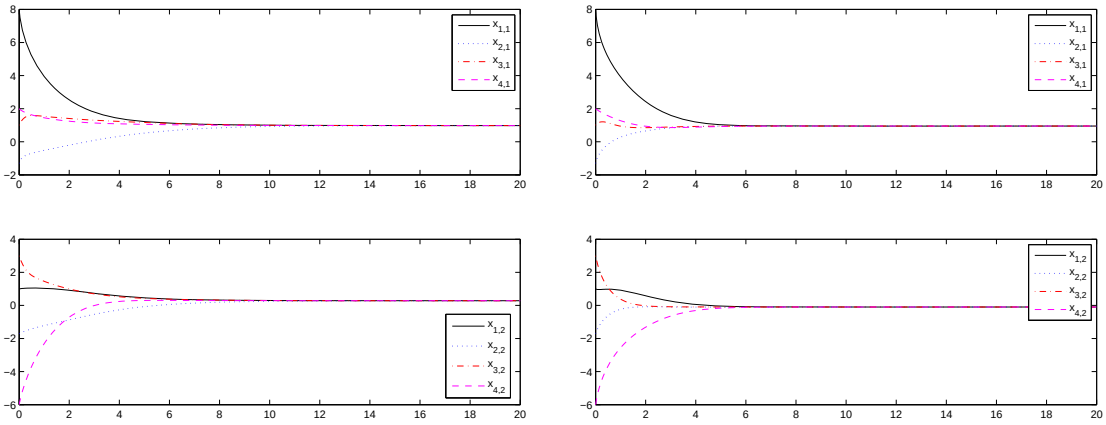

Figure 4.6: State evolution over time for $\mathcal{G}_1$ (left) and $\mathcal{G}_2$ (right)

Domains	Convex functions
$\mathbf{dom}\,\boldsymbol{x}_1$	$\{\boldsymbol{x}_1 = [\ x_{1,1} \quad x_{1,2}\ ] \in \mathrm{R}^2 \mid f_1 = (x_{1,1}-3)^2 + (x_{1,2}-1)^6 - 30 < 0\}$
$\mathbf{dom}\,\boldsymbol{x}_2$	$\{\boldsymbol{x}_2 = [\ x_{2,1} \quad x_{2,2}\ ] \in \mathrm{R}^2 \mid f_2 = 3x_{2,1}^2 + 2x_{2,2}^2 - 4x_{2,1}x_{2,2} - 5 < 0\}$
$\mathbf{dom}\,\boldsymbol{x}_3$	$\{\boldsymbol{x}_3 = [\ x_{3,1} \quad x_{3,2}\ ] \in \mathrm{R}^2 \mid f_{3,1} = x_{3,2} + 0.3x_{3,1} - 7 < 0$
	$f_{3,2} = -6x_{3,1} - x_{3,2} - 2 < 0$
	$f_{3,3} = 2x_{3,1} - 2 - x_{3,2} < 0\}$
$\mathbf{dom}\,\boldsymbol{x}_4$	$\{\boldsymbol{x}_4 = [\ x_{4,1} \quad x_{4,2}\ ] \in \mathrm{R}^2 \mid f_4 = x_{4,1}^2 + (x_{4,2}+3)^2 - 25 < 0\}$

Table 4.1: The remote control coverage sets - simulation parameters

β_1	β_2	$\beta_{3,1}$	$\beta_{3,2}$	$\beta_{3,3}$	β_4
68	5	14	168	168	62

Table 4.2: The shift parameter $\beta_{i,k}$ for the simulation example 2

4.4 Application to Spacecraft Attitude Synchronization under Attitude Constrained Zones

In this section, we consider an attitude synchronization problem when each spacecraft has its own attitude forbidden zone. This problem appears, for example, in the context of multiple spacecraft interferometry which requires precise target synchronization over multiple spacecraft while avoiding direct exposure to sunlight or other bright objects due to sensors' sensitivity. The presented approach is, however, novel as removing constrained zones from the rotational configuration space of the spacecraft generally results in a non-convex domain. Our approach utilizes a constrained consensus algorithm along with a convexified constrained zone formulation written in unit quaternions in order to describe the consensus in the presence of respective attitude constrained zones in the group of spacecraft. The fact that the total potential function for the group can be convexified enables us to apply the constrained consensus algorithm presented in the previous section. In the constrained

consensus problem, each agent converges to the intersection of the domain sets of its neighbors if the agents values are constrained in convex sets and each agent is only aware of its respective constrained set. We then proceed to show that a consensus-like control derived from this approach can be extended to the case of rigid bodies.

4.4.1 Attitude Consensus under Attitude Forbidden Zones

In this section, we expand on the previous section's results for multi-spacecraft scenarios by applying the constrained consensus algorithm. Revisiting §4.3, it has been shown that the potential function associated with the sum of squares of differences between agent's states in the strongly connected and balanced network, i.e.,

$$\begin{aligned} J(\mathbf{x}) &= \sum_i \sum_{i \leftarrow j} \frac{1}{2} \|x_j - x_i\|^2 g_i(x_i) \\ &= \frac{1}{2} \boldsymbol{x}^T [DWD^T] \boldsymbol{x} = \frac{1}{2} \boldsymbol{x}^T L_w \boldsymbol{x}, \end{aligned} \tag{4.62}$$

can be convexified in $\boldsymbol{x} = [\ x_1^T \ \cdots \ x_n^T\ ]^T$, where $x_i \in \{x \in \mathcal{D}_x \,|\, g_i(x_i) > 0\}$. The non-negative matrix W has the form

$$W = \begin{bmatrix} g_1(x_1) & 0 & 0 \\ 0 & \ddots & 0 \\ 0 & 0 & g_n(x_n) \end{bmatrix}_{m \times m}, \tag{4.63}$$

where n denotes the total number of agents and m denotes the total number of directed edges in the graph, and D denotes the incidence matrix representing the underlying information-exchange network. Note that $m \leq l = n(n-1)$ where l designates the maximum number of directed edges in the graph $\mathcal{G}$.

By *Proposition 4.4*, the fact that $x_i \to \partial \mathcal{D}_{x_i}$, $g_i(x_i) \to \infty$ and $J(\boldsymbol{x})$ is convex in $\boldsymbol{x}$, leads us to conclude that consensus

$$x_1 = x_2 = \cdots = x_n, \tag{4.64}$$

is achieved when $J(\boldsymbol{x})$ in Eq. (4.62) vanishes; moreover, the consensus value lies at the intersection of individual attitude permissible zones, which is an obvious result from the requirement that W is positive definite for all x_i.

Thus, the negative gradient of $J(\boldsymbol{x})$ in Eq. (4.62) leads to a distributed agreement protocol on the state dependent network:

$$-\frac{\partial V}{\partial x_i} = \sum_{i \leftarrow j} (g_i + g_j)[x_j - x_i] + \frac{1}{2} \|x_j - x_i\|^2 [-\nabla g_i]. \tag{4.65}$$

Note that the null space of L_w in Eq. (4.62) is only spanned by $\mathbf{1}$ if the agents form a strongly connected and balanced network. Analogous to the preceding section, convexity of the total potential function enables us to consider an energy-like potential

$$V_t : (\mathcal{S}^3 \times \mathbb{R}^3) \times \mathbb{R}^n \to \mathbb{R},$$

given as

$$\begin{aligned} V_t &= \sum_i \Big[\sum_{i \leftarrow j} \frac{1}{2} \|\mathbf{q}_j - \mathbf{q}_i\|^2 g_i + \frac{1}{2} \omega_i^T \boldsymbol{J}_i \omega_i \Big] && (4.66) \\ &= \frac{1}{2} \mathbf{q_t}^T [D_\oplus W_\oplus D_\oplus^T] \mathbf{q_t} + \sum_i \frac{1}{2} \omega_i^T \boldsymbol{J}_i \omega_i && (4.67) \\ &= \mathbf{q_t}^T M_\oplus \mathbf{q_t} + \sum_i \frac{1}{2} \omega_i^T \boldsymbol{J}_i \omega_i, && (4.68) \end{aligned}$$

where $\mathbf{q}_i \in \{\mathbf{q}_i \in \mathbf{U_q} \,|\, -q_i^T M_i q_i < 0\}$ for $i = 1, ..., n$, $\mathbf{q_t} = [\ \mathbf{q}_1^T \ \cdots \ \mathbf{q}_n^T\ ]^T$, $M_\oplus = M \oplus \mathbf{I}_4$, and M denotes the graph M matrix of the underlying network; note that $[\cdot]_\oplus$ signifies $[\cdot] \oplus \mathbf{I}_4$, where '$\oplus$' denotes the Kronecker product.[1] Next, recalling *Proposition 3.7*, the ith spacecraft's control law is given as

$$u_i = -k_w \omega_i + \frac{1}{2} \mathtt{Vec}\Big[\Big(\frac{\partial V_t}{\partial \mathbf{q}_i} \Big)^* \otimes \mathbf{q}_i \Big], \tag{4.69}$$

where the operator $\mathtt{Vec}[\cdot]$ denotes the vector part of the unit quaternion, and the gain k_w is strictly positive. Note that the above control law stabilizes the rigid body dynamics, Eqs. (3.43)-(3.44) around the global minimum of convex function V_t which yields $V_t = 0$; see §3.5.2 for more details. Hence, Eq. (4.52) leads to

$$\frac{\partial V_t}{\partial \mathbf{q}_i} = \sum_{i \leftarrow j} (g_i + g_j)[\mathbf{q}_i - \mathbf{q}_j] - \|\mathbf{q}_j - \mathbf{q}_i\|^2 \left[\frac{M_i \mathbf{q}_i}{\mathbf{q}_i^T M_i \mathbf{q}_i} \right]. \tag{4.70}$$

---

[1] In this paper, we use '$\oplus$' for denoting the Kronecker product in order to avoid confusion with the symbol for quaternion multiplication '$\otimes$'.

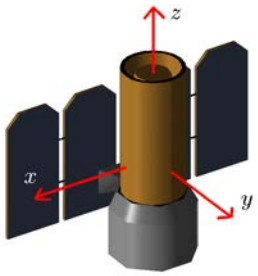

Figure 4.7: Spacecraft configuration with one light sensitive instrument and a high gain antenna.

Now, we rewrite Eq. (4.69) from Eq. (4.70) as

$$u_i = -k_w\omega_i - \frac{1}{2}\sum_{i\leftarrow j}\mathtt{Vec}\Big[(g_i+g_j)(\mathbf{q}_j\otimes\mathbf{q}_i) + \frac{\|\mathbf{q}_j-\mathbf{q}_i\|^2}{\mathbf{q}_i^T M_i\mathbf{q}_i}(M_i\mathbf{q}_i)^*\otimes\mathbf{q}_i\Big], \tag{4.71}$$

where

$$g_i(\mathbf{q}_i) = -k_i\log\Big[-\frac{\mathbf{q}_i^T M_i\mathbf{q}_i}{2e^2}\Big] \tag{4.72}$$
$$\text{for } i=1,2,\ldots n,$$

and k_i denotes a weighting parameter imposing to the ith spacecraft's constraint. We have used the fact $\mathtt{Vec}[\mathbf{q}_i^*\otimes\mathbf{q}_i]=\mathbf{0}$. Note that the control u_i for ith spacecraft only requires knowledge of $\mathbf{q}_j$ and g_j from the jth neighbor.

4.4.2 Simulations

In this section, we present simulation results for the attitude synchronization in the presence of attitude forbidden zones. Two scenarios where six spacecraft are required to align their attitudes have been explored. Each spacecraft is assumed to carry a light sensitive interferometer with a fixed bore-sight along the z-body axis as seen in Fig. 4.7. It is further assumed that each spacecraft only obtains its neighbors' attitude through a directional communication network. As mentioned in the preceding section, the strongly connected and balanced communication network is necessary.

In the first scenario, we consider the scenario where the attitude forbidden zones are identical over all six spacecraft while we consider each spacecraft with a distinct attitude

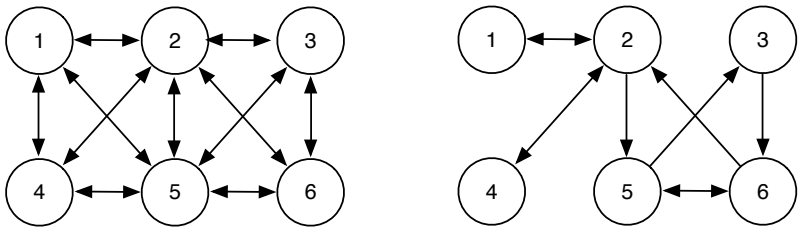

Figure 4.8: Communication graphs *network* **A** (left) and *network* **B** (right)

forbidden zone in the second scenario. Note that in the second scenario, the spacecraft attitude forbidden zone have been defined as the intersection of all permissible zones is non-empty in order to satisfy the requirements in *Proposition 4.4*. For each scenario, the strongly connected and balanced networks are considered, namely *network* **A** and *network* **B**. These graphs are shown in Fig. 4.8. All initial attitudes, shown in Table 4.3, are randomly selected but they satisfy the attitude permissible zone so that $\mathbf{q}_i(0) \in \mathbf{q}_{P_i}$ for all i.

The specific application is to the initialization of a group of spacecraft interferometers. Thus, we randomly choose the spacecraft's initial angular velocities presented in Table 4.5. In the other hand, although it is generally not necessary that the spacecraft's moments of inertias are identical, we assume that this condition holds for our simulation examples and given as

$$J = \begin{bmatrix} 907.8 & 0 & 0 \\ 0 & 782.7 & 0 \\ 0 & 0 & 471.9 \end{bmatrix} \text{ (kg}\cdot m^2\text{)}. \tag{4.73}$$

We note that the parameters k_w and k_i in the control laws, Eq. (4.71) influence the convergence rate of the algorithm since the corresponding logarithmic terms rapidly increase as the norm $\|\mathbf{q}_j - \mathbf{q}_i\|^2$, associated with an attraction term towards the neighbors' attitude, decreases.

Figs. 4.9 and 4.10 describe initial and final attitudes of the group of spacecraft and the attitude forbidden zones in three dimensional space. Figs. 4.11 and 4.12, on the other hand,

Network **A**				*Network* **B**			
0.5465	-0.2895	0.0852	0.7812	-0.3505	-0.7336	0.0384	0.5809
0.7692	-0.2582	-0.0230	0.5840	-0.5166	0.0013	-0.6128	0.5980
0.1936	-0.6657	0.4690	-0.5471	-0.5494	-0.6195	-0.1641	0.5361
0.5465	-0.2895	0.0852	0.7812	-0.8872	-0.4220	0.1362	0.1276
0.3234	0.7354	-0.2245	0.5515	0.4741	0.8041	-0.2990	-0.1981
-0.2451	0.6821	-0.5870	0.3607	-0.3505	-0.7336	0.0384	0.5809

Table 4.3: Initial attitudes in unit quaternions for scenario 1 and 2

depict the unit quaternion trajectories for scenarios 1 and 2, respectively, while Figs. 4.13 and 4.14 depict the corresponding angular velocities over time. Note that all spacecraft converge to the same attitude regardless of the configuration of their respective attitude forbidden zones. Figs. 4.15-4.16 trace the pointing directions of the light sensitive instruments on the cylindrical projection of celestial sphere for scenarios 1 with both *Network* **A** and *Network* **B** whereas Figs. 4.17-4.18 do these pointing directions for scenarios 2 with both *Network* **A** and *Network* **B**, where '$\circ$' denotes initial orientations while '$\square$' denotes the synchronized orientations. Figs. 4.19 and 4.20 represent the trajectories of $-\mathbf{q}_i^T M_i \mathbf{q}_i$ over time. Note that they are all assured to be positive.

As expected, the connection *network* **B**, compared to the more dense connection *network* **A**, shows prolonged convergences and oscillations due to its better connectivity as shown in Figs. 4.11-4.14. For the same error tolerance, *network* **B** takes 8 times longer period to reach consensus over *network* **A**.

4.5 Concluding Remarks

In this chapter, we have considered the continuous constrained consensus algorithm with the aid of the logarithmic barrier function. The proposed algorithm is applicable when each agents state is restricted to stay in the interior of a compact convex set. Subsequently, this algorithm has applied to spacecraft attitude synchronization over a network in presence

Network **A**			Angle	Type
-0.5000	0.8660	0	85 deg	Forbidden

Network **B**			Angle	Type
-0.1736	0.9848	0	70 deg	Forbidden
0	-0.9397	0.3420	50 deg	Forbidden
0.6040	-0.2118	-0.7683	45 deg	Forbidden
0.3420	-0.9397	0	55 deg	Forbidden
0.1170	0.7482	0.6531	70 deg	Forbidden
0	-0.8660	-0.5000	85 deg	Forbidden

Table 4.4: Attitude Forbidden Zones parameters, position vectors and forbidden angles for scenario 1 and 2

Scenario 1			Scenraio 2		
0.0930	-0.0685	0.0941	-0.0550	-0.0300	-0.0426
0.0914	-0.0029	0.0601	0.0855	-0.0897	0.0185
-0.0716	-0.0156	0.0831	-0.0674	0.0677	-0.0665
0.0584	0.0919	0.0311	0.0004	0.0999	-0.0289
-0.0929	0.0698	0.0868	-0.0906	-0.0573	-0.0204
0.0357	0.0515	0.0486	-0.0333	-0.0541	0.0872

Table 4.5: Initial angular velocities in body axis for scenario 1 and 2

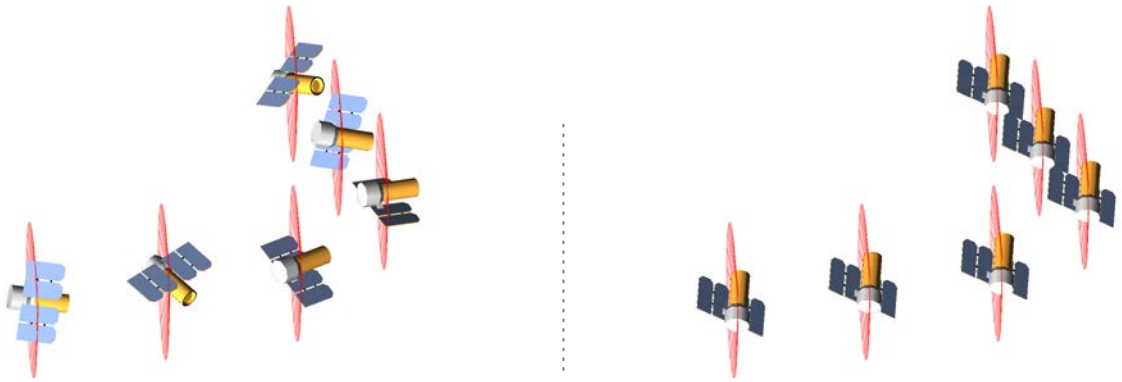

Figure 4.9: 3D illustration of spacecraft's initial attitudes (left) and final attitudes (right) in the presence of indentical attitude forbidden zones (scenario 1 with *Network* **A**)

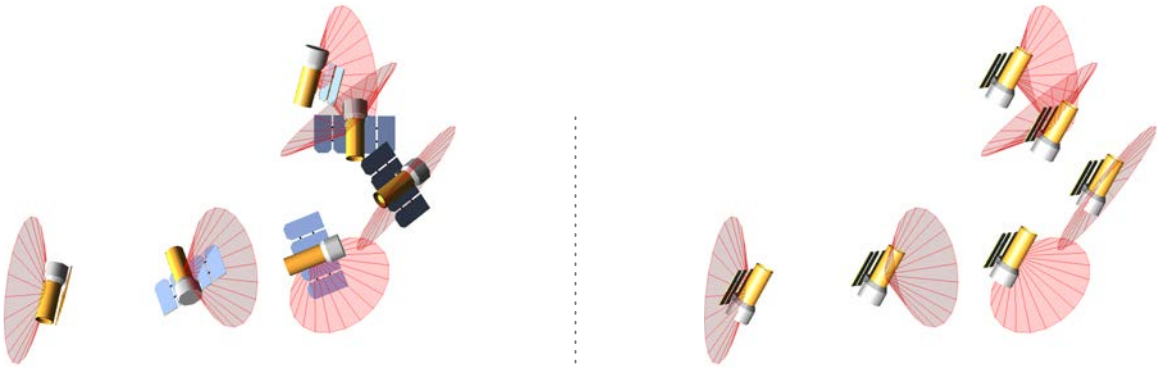

Figure 4.10: 3D illustration of spacecraft's initial attitudes (left) and final attitudes (right) in the presence of independent attitude forbidden zones (scenario 2 with *Network* **B**)

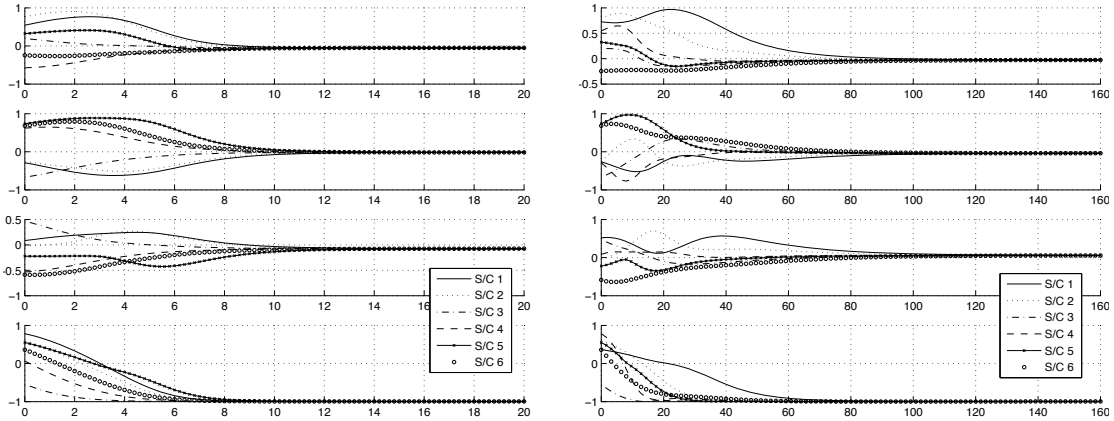

Figure 4.11: Spacecraft unit quaternions for scenario 1 with *network* **A** (left) and **B** (right)

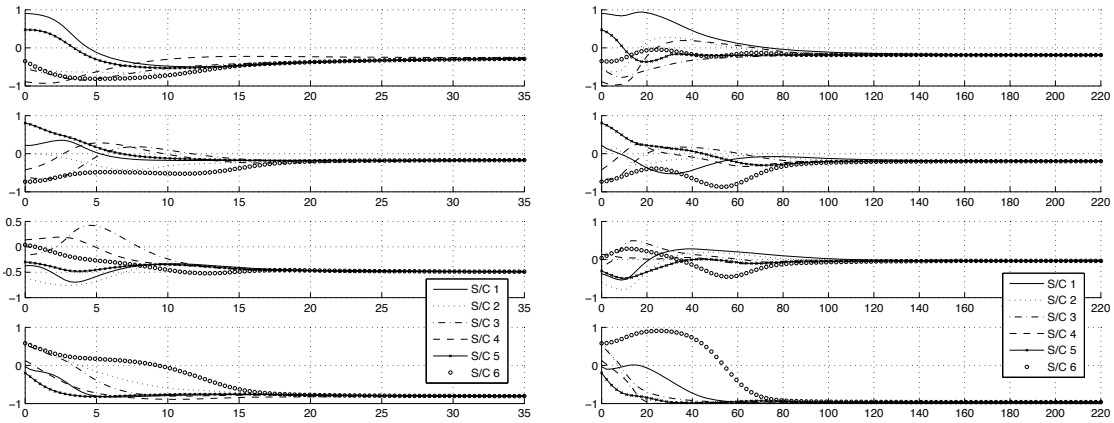

Figure 4.12: Spacecraft unit quaternions for scenario 2 with *network* **A** (left) and **B** (right)

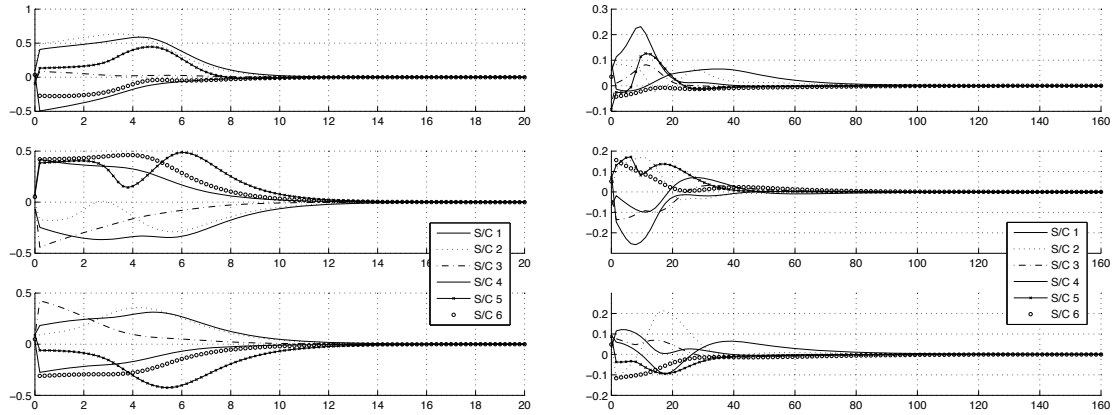

Figure 4.13: Spacecraft angular velocities for scenario 1 with *network* **A** (left) and **B** (right)

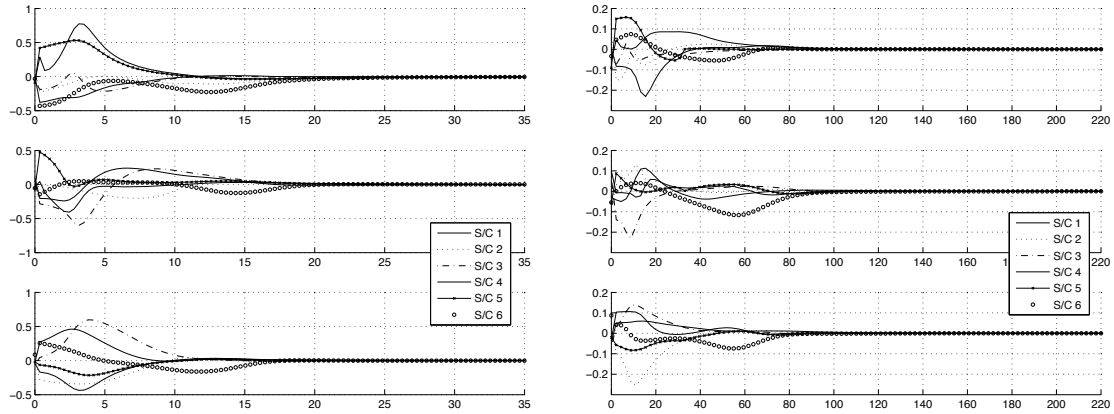

Figure 4.14: Spacecraft angular velocities for scenario 2 with *network* **A** (left) and **B** (right)

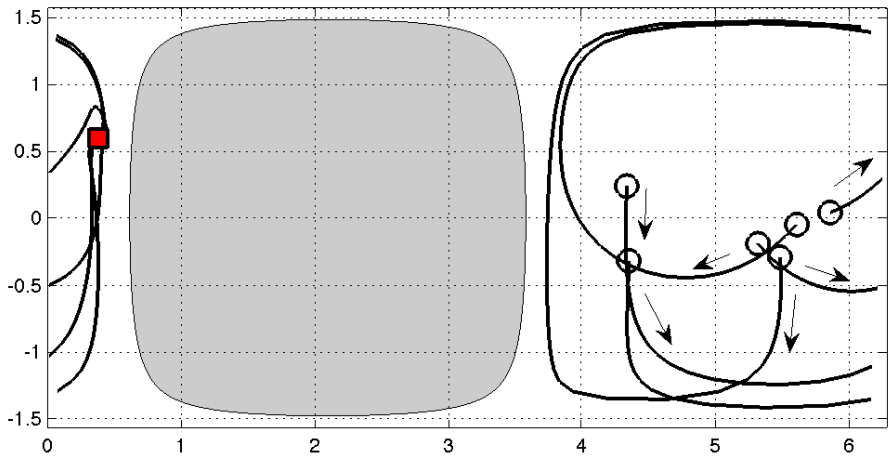

Figure 4.15: Spacecraft's orientation trajectories on a cylindrical projection of celestial sphere in scenario 1 with *Network* **A**. '○' denotes initial orientations while '□' denotes synchronized orientations.

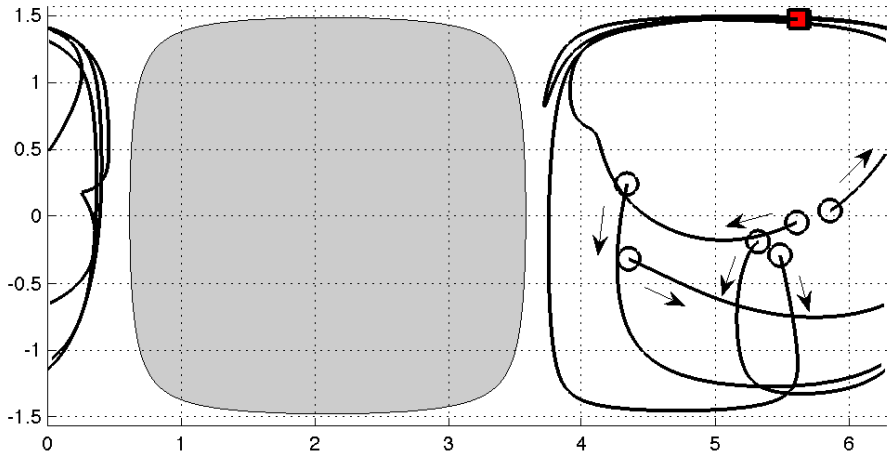

Figure 4.16: Spacecraft's orientation trajectories on a cylindrical projection of celestial sphere in scenario 1 with *Network* **B**. '○' denotes initial orientations while '□' denotes synchronized orientations.

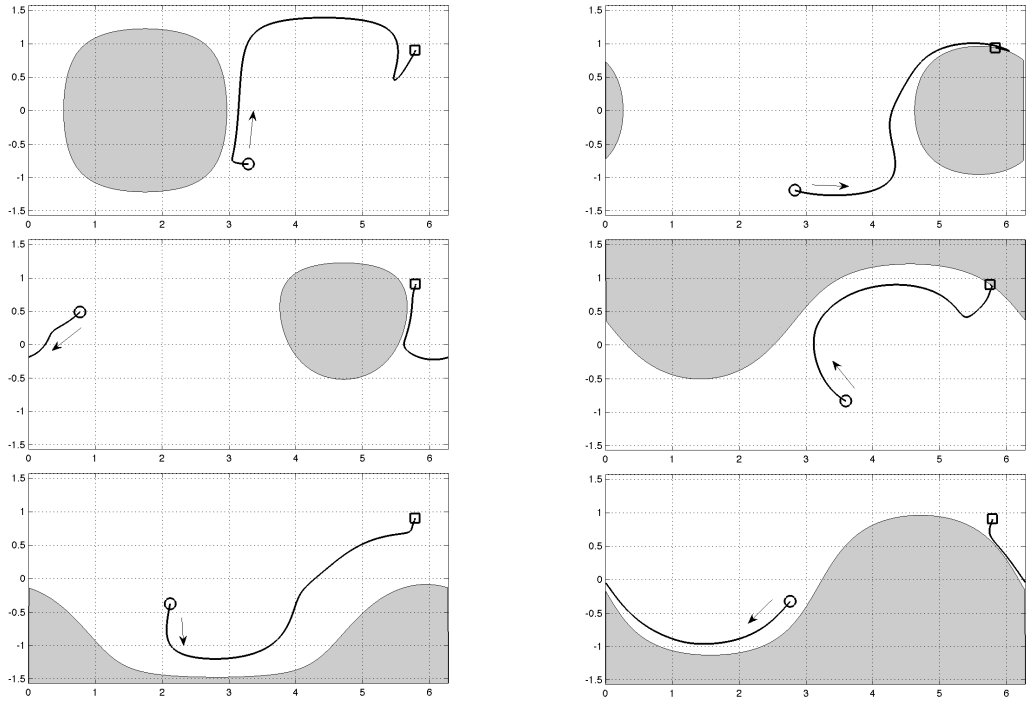

Figure 4.17: Spacecraft's orientation trajectories on a cylindrical projection of celestial spaces in scenario 2 with *Network* **A**.

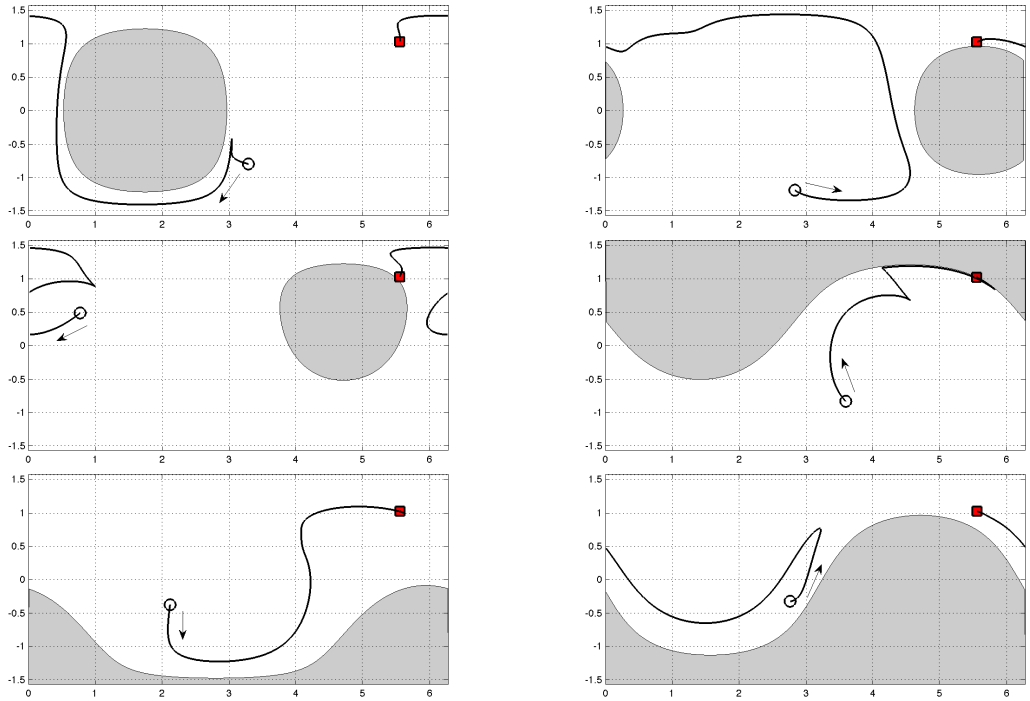

Figure 4.18: Spacecraft's orientation trajectories on a cylindrical projection of celestial spaces in scenario 2 with *Network* **B**.

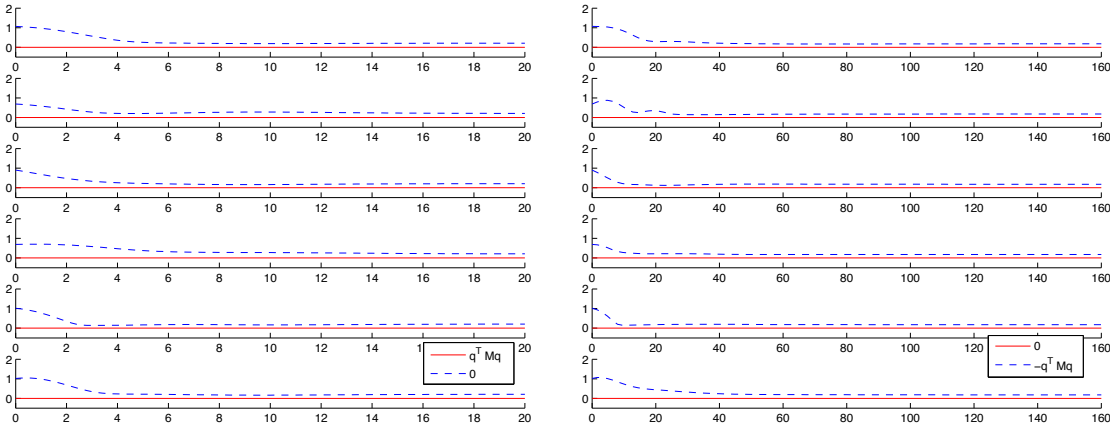

Figure 4.19: The trajectories of $-q_i^T M_i q_i$ over time for scenario 1 with *network* **A** (left) and **B** (right). . They stay positive over all time.

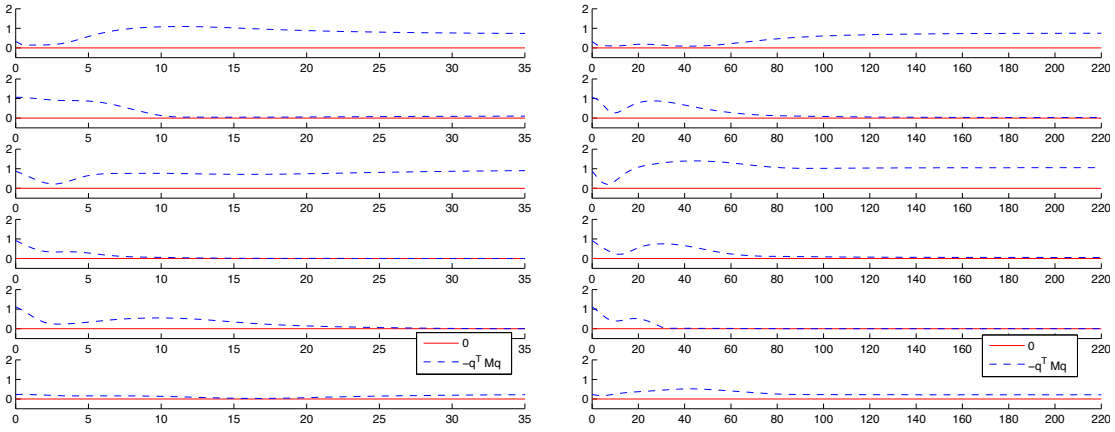

Figure 4.20: The trajectories of $-q_i^T M_i q_i$ over time for scenario 2 with *network* **A** (left) and **B** (right). . They stay positive over all time.

of multiple attitude constrained zones. For the synchronization problem, each spacecraft was assumed to be able to access only auxiliary system outputs and attitude parameters from its neighboring spacecraft. Simulation results were then presented for a six spacecraft formation to evaluate the effectiveness of the proposed distributed control algorithms.

Chapter 5

ROTATIONALLY AND TRANSLATIONALLY CONSTRAINED RIGID BODY CONTROL

In this chapter, we address a general framework for the analysis of unconstrained and rotationally and translationally coupled constrained control problems for a rigid body. Autonomous control algorithms for rotationally and translationally constrained motions are challenging to design as they involve dependent variables that evolve in distinct configuration spaces. The *unit dual quaternion* parameterization can capture this dependency. Using this parameterization, we develop an array of globally stable control laws for unconstrained and constrained rigid body dynamics via a convex energy-like Lyapunov function on dual quaternions. Furthermore, we characterize the convex representable subset of unit dual quaternions that corresponds to translational and rotational motions that satisfy predefined translationally and rotationally coupled constraints with respect to the body frame. We then proceed to construct a quadratically constrained quadratic programming to control a rigid body undergoing these constrained sets, which subsequently provides translational and rotational control laws for a wide range of applications. The powered-descent guidance problem for landers is discussed as a application for the proposed framework, which is considered to be challenging as the attitude of the lander is coupled with its translational dynamics via its human window view angle as well as the thruster incidence angle [10, 11].

5.1 Literature Reviews

Research in dynamics and control has always been interested in insightful representations of the three-dimensional rigid body dynamics on the special Euclidean group $\mathsf{SE}(3)$. In this context, translational and rotational motions of rigid bodies are independently considered and examined. As unit quaternions have become an attractive option for describing a large angle reorientation over canonical Euler angles [43], particularly in spacecraft applications, the unit "dual" quaternion has re-emerged as a plausible representation for $\mathsf{SE}(3)$. Meanwhile, the unit dual quaternion has been successfully applied in various fields such as inertial navigation [59], biomechanics [102], computer graphics [99], and attitude control [22,92,97,115]. Moreover, the work presented in [71] introduces the potential advantages of unit quaternions over a homogeneous transformation in robot arm control.

In this chapter, we propose a general framework based on unit dual quaternions for obtaining almost globally stable control laws on $\mathsf{SE}(3)$, and subsequently apply it for a control laws simultaneously tracking position and attitude with feedback. The dual quaternion representation has advantages over other parameterizations, such as the 4×4 homogeneous transformation matrix, not only for its minimal representation of $\mathsf{SE}(3)$ without singularities, but also for its ability to have seamless, amalgamated dynamics and kinematics, as developed in the later part of this chapter.

The research presented here is motivated in part by the early work of [69] on spacecraft attitude control in the presence of attitude constraints, which focused on the convexification of a subset of unit quaternions and adopted a Lyapunov approach to derived attitude control laws. As will be shown in this chapter, there exists a natural analogy between rotational controllers based on unit quaternions and combined translational and rotational controllers based on unit dual quaternions. In this chapter, we present a convex parameterization of the subset of unit dual quaternions corresponding to all possible orientations and positions that lie within a given field of view with respect to the body frame. We then build on this parameterization to obtain globally stable control laws that regulate the unit dual quaternion dynamics within the corresponding convexified subset using a logarithmic barrier potential [69].

5.2 Dual Vectors, Dual Quaternions and SE(3)

In this section, we provide a brief background on dual vectors, unit quaternions, and unit dual quaternions. More detailed discussion on these representations can be found in [59, 70, 112].

5.2.1 Dual Vectors

The concept of the "dual vector" was invented by Clifford to compensate for the insufficient information encoded in a "regular" vector; the latter are the 3×1 vectors in this paper. The dual vector $\tilde{v}$ is comprised of two vectors: v_1 and v_2, denoting the real and dual parts of $\tilde{v}$, respectively, combined as

$$\tilde{v} = v_1 + \epsilon\, v_2, \tag{5.1}$$

where ϵ denotes the "dual unit" satisfying the "unconventional" properties

$$\epsilon^2 = 0 \quad \text{and} \quad \epsilon \neq 0. \tag{5.2}$$

By definition, dual vectors satisfy

$$\tilde{v} + \tilde{p} = v_1 + p_1 + \epsilon\,(v_2 + p_2), \tag{5.3}$$

$$\alpha\,\tilde{v} = \alpha\, v_1 + \epsilon\,\alpha v_2, \tag{5.4}$$

$$\tilde{v}\tilde{p} = v_1 p_1 + \epsilon\,(v_1 p_2 + v_2 p_1). \tag{5.5}$$

where α is a scalar. Let us now present convenient notations for dual vectors. Since all operations are linear, dual vectors can be embedded in $\mathbb{R}^6$ Euclidean space as

$$\tilde{v} = \begin{bmatrix} v_1 \\ v_2 \end{bmatrix}_{6\times 1}. \tag{5.6}$$

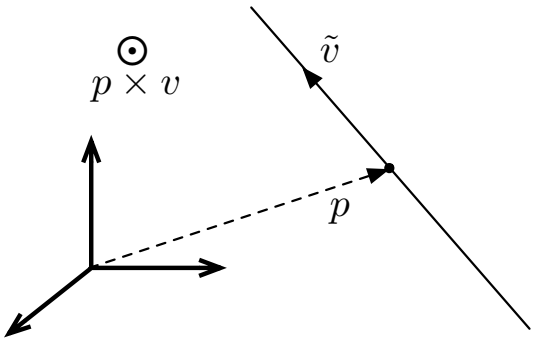

Figure 5.1: Plücker line in 3 dimensional space

Accordingly, Eqs. (5.3-5.5) can be rewritten as

$$\tilde{v} + \tilde{p} = \begin{bmatrix} v_1 + p_1 \\ v_2 + p_2 \end{bmatrix}, \tag{5.7}$$

$$\alpha\, \tilde{v} = \begin{bmatrix} \alpha\, v_1 \\ \alpha v_2 \end{bmatrix}, \tag{5.8}$$

$$\tilde{v}\tilde{p} = \begin{bmatrix} v_1 p_1 \\ v_1 p_2 + v_2 p_1 \end{bmatrix}. \tag{5.9}$$

A dual vector can represent a vector in space; in 3D the vector is known as the Plücker coordinates. As seen in Fig. 5.1 a vector passing through a point p in 3D space can be written as the dual vector $\tilde{v}$:

$$\tilde{v} = \begin{bmatrix} v \\ p \times v \end{bmatrix}. \tag{5.10}$$

Note that a conventional vector possesses information of direction and magnitude with $v \in \mathbb{R}^3$. On the other hand, a dual vector holds additional information that represents position with respect to a fixed frame from $p \times v$. This property enables a very intriguing geometric interpretation between two dual vectors. For example, since dual vectors are

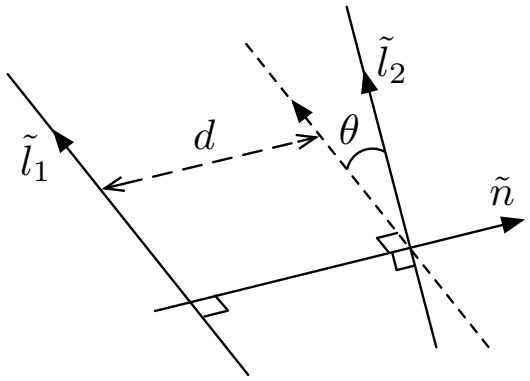

Figure 5.2: Geometric relationship between two dual vectors $\tilde{l}_1$ and $\tilde{l}_2$

closed under vector dot and cross products, it follows that,

$$\tilde{l}_1 \cdot \tilde{l}_2 = \cos\tilde{\theta} \tag{5.11}$$

$$\tilde{l}_1 \times \tilde{l}_2 = \sin\tilde{\theta}\tilde{n}, \tag{5.12}$$

where

$$\tilde{\theta} = \theta + \epsilon\, d, \tag{5.13}$$

and $\tilde{l}_1$ and $\tilde{l}_2$ are unit dual vectors (with unit norm real parts). The parameter $\tilde{\theta}$ (5.13) denotes a dual number (scalar) which has an angle θ and translation distance d, while $\tilde{n}$ denotes a unit dual vector which is perpendicular to the two lines. As shown in Fig. 5.2, the dot and cross products nicely illustrate the geometric relationship between two dual vectors.

5.2.2 Unit Quaternions

The attitude of a rigid body, describing the relative orientation between a reference frame and a body-fixed frame, evolves on the special orthogonal group $\mathsf{SO(3)}$. The unit quaternion is a minimal parameterization of $\mathsf{SO(3)}$ free from singularities. See Chapter 2.2 for more details. In order to interact with dual quaternions, we additionally define the following operation.

Quaternion Cross Products

For some quaternion operations on 3×1 vectors, i.e., $f : (\mathbf{q}, \mathbf{p}) \in \mathbb{R}^4 \to \mathbb{R}^3$, we define a relaxed quaternion operation because the scalar part in its output is ignored. For instance, the quaternion multiplication Eq. (2.18) can be relaxed to the newly defined *quaternion cross product* as

$$\mathbf{q} \times \mathbf{p} = \begin{bmatrix} q_0\boldsymbol{p} + p_0\boldsymbol{q} + \boldsymbol{q} \times \boldsymbol{p} \\ 0 \end{bmatrix} \tag{5.14}$$

$$= \begin{bmatrix} [\boldsymbol{q}]_\times + q_0\mathbf{I}_3 & \boldsymbol{q} \\ 0_{1\times 3} & 0 \end{bmatrix} \begin{bmatrix} \boldsymbol{p} \\ p_0 \end{bmatrix} \tag{5.15}$$

$$\stackrel{\text{def}}{=} [\mathbf{q}]_\times \mathbf{p}, \tag{5.16}$$

where $\mathbf{q}, \mathbf{p}$ denote quaternions and $[\cdot]_\times$ denotes a 4×4 matrix corresponding to the *quaternion cross product*.

5.2.3 Dual Quaternions

A dual quaternion is in fact what its name suggests: it is the dual of the usual quaternion, leading to an extension of the dual vector, namely,

$$\tilde{\mathbf{q}} = \mathbf{q}_1 + \epsilon\, \mathbf{q}_2, \text{ or } \tilde{\mathbf{q}} = \begin{bmatrix} \mathbf{q}_1 \\ \mathbf{q}_2 \end{bmatrix}_{8\times 1} \tag{5.17}$$

where $\boldsymbol{q}_1$ and $\boldsymbol{q}_2$ are quaternions. For a unit dual quaternion, the real part $\mathbf{q}_1$ is restricted to be a unit norm vector $\|\mathbf{q}_1\|_2 = 1$.

The dual quaternion is also closed under addition and multiplication, given the property

defined in Eq. (5.2). These linear operations are similarly given as

$$\tilde{\mathbf{p}} + \tilde{\mathbf{q}} = \mathbf{p}_1 + \mathbf{q}_1 + \epsilon\,(\mathbf{p}_2 + \mathbf{q}_2) = \begin{bmatrix} \mathbf{p}_1 + \mathbf{q}_1 \\ \mathbf{p}_2 + \mathbf{q}_2 \end{bmatrix}, \tag{5.18}$$

$$\alpha\,\tilde{\mathbf{q}} = \alpha\mathbf{q}_1 + \epsilon\,\alpha\mathbf{q}_2 = \begin{bmatrix} \alpha\mathbf{q}_1 \\ \alpha\mathbf{q}_2 \end{bmatrix}, \tag{5.19}$$

$$\tilde{\mathbf{q}} \otimes \tilde{\mathbf{p}} = \mathbf{q}_1 \otimes \mathbf{p}_1 + \epsilon\,(\mathbf{q}_1 \otimes \mathbf{p}_2 + \mathbf{q}_2 \otimes \mathbf{p}_1) = \begin{bmatrix} \mathbf{q}_1 \otimes \mathbf{p}_1 \\ \mathbf{q}_1 \otimes \mathbf{p}_2 + \mathbf{q}_2 \otimes \mathbf{p}_1 \end{bmatrix}. \tag{5.20}$$

Note that dual quaternion multiplication, denoted by $\otimes$ is a linear operation; we can represent it as a multiplication between a matrix and a vector (dual quaternion) in conformance with quaternion multiplication as described in Eq. (2.20). This is shown below:

$$\tilde{\mathbf{q}} \otimes \tilde{\mathbf{p}} = \begin{bmatrix} [\mathbf{q}_1]_\otimes & 0_{4\times4} \\ [\mathbf{q}_2]_\otimes & [\mathbf{q}_1]_\otimes \end{bmatrix} \begin{bmatrix} \mathbf{p}_1 \\ \mathbf{p}_2 \end{bmatrix} \tag{5.21}$$

$$\stackrel{\text{def}}{=} [\tilde{\mathbf{q}}]_\otimes\,\tilde{\mathbf{p}}. \tag{5.22}$$

As an extension of the *quaternion cross product*, we also define

$$\tilde{\mathbf{q}} \times \tilde{\mathbf{p}} = \begin{bmatrix} \mathbf{q}_1 \times \mathbf{p}_1 \\ \mathbf{q}_1 \times \mathbf{p}_2 + \mathbf{q}_2 \times \mathbf{p}_1 \end{bmatrix} = \begin{bmatrix} [\mathbf{q}_1]_\times & 0_{4\times4} \\ [\mathbf{q}_2]_\times & [\mathbf{q}_1]_\times \end{bmatrix} \begin{bmatrix} \mathbf{p}_1 \\ \mathbf{p}_2 \end{bmatrix} \tag{5.23}$$

$$\stackrel{\text{def}}{=} [\tilde{\mathbf{q}}]_\times\,\tilde{\mathbf{p}}. \tag{5.24}$$

When the dual quaternion has a nonzero real part, its inverse can be obtained as $\tilde{\mathbf{q}}^{-1} = \|\tilde{\mathbf{q}}\|^{-1}\tilde{\mathbf{q}}^*$; on the other hand, its conjugate is defined as

$$\tilde{\mathbf{q}}^* = \begin{bmatrix} \mathbf{q}_1^* \\ \mathbf{q}_2^* \end{bmatrix}. \tag{5.25}$$

Theorem 5.1 (Dual Quaternion Dot Product Identity)**.** *Consider* $\tilde{\mathbf{a}}, \tilde{\mathbf{b}}$*, and* $\tilde{\mathbf{c}}$ *to be dual quaternions. Then there are special properties between the dot and dual quaternion multiplication operations such that*

$$\tilde{\mathbf{a}}^T(\tilde{\mathbf{b}} \otimes \tilde{\mathbf{c}}) = \tilde{\mathbf{c}}^T[\mathbf{a}\mathbf{I}]\left(\tilde{\mathbf{b}}^* \otimes ([\mathbf{a}\mathbf{I}]\tilde{\mathbf{a}})\right), \tag{5.26}$$

where $[\mathbf{aI}]$ *denotes an anti-diagonal identity matrix defined by*

$$[\mathbf{aI}] = \begin{bmatrix} 0_{4\times4} & \mathbf{I}_4 \\ \mathbf{I}_4 & 0_{4\times4} \end{bmatrix}_{8\times8}. \tag{5.27}$$

Proof. The proof is as follows.

$$\begin{bmatrix} \mathbf{a}_1 \\ \mathbf{a}_2 \end{bmatrix}^T \left(\begin{bmatrix} \mathbf{b}_1 \\ \mathbf{b}_2 \end{bmatrix} \otimes \begin{bmatrix} \mathbf{c}_1 \\ \mathbf{c}_2 \end{bmatrix} \right) = \begin{bmatrix} \mathbf{a}_1 \\ \mathbf{a}_2 \end{bmatrix}^T \begin{bmatrix} \mathbf{b}_1 \otimes \mathbf{c}_1 \\ \mathbf{b}_1 \otimes \mathbf{c}_2 + \mathbf{b}_2 \otimes \mathbf{c}_1 \end{bmatrix} \tag{5.28}$$

$$= \mathbf{a}_1^T(\mathbf{b}_1 \otimes \mathbf{c}_1) + \mathbf{a}_2^T(\mathbf{b}_1 \otimes \mathbf{c}_2) + \mathbf{a}_2^T(\mathbf{b}_2 \otimes \mathbf{c}_1) \tag{5.29}$$

$$= \mathbf{c}_1^T(\mathbf{b}_1^* \otimes \mathbf{a}_1) + \mathbf{c}_2^T(\mathbf{b}_1^* \otimes \mathbf{a}_2) + \mathbf{c}_1^T(\mathbf{b}_2^* \otimes \mathbf{a}_2) \tag{5.30}$$

$$= \begin{bmatrix} \mathbf{c}_1 \\ \mathbf{c}_2 \end{bmatrix}^T \begin{bmatrix} \mathbf{b}^* \otimes \mathbf{a}_1 + \mathbf{b}_2^* \otimes \mathbf{a}_2 \\ \mathbf{b}_1^* \otimes \mathbf{a}_2 \end{bmatrix} \tag{5.31}$$

$$= \begin{bmatrix} \mathbf{c}_1 \\ \mathbf{c}_2 \end{bmatrix}^T [\mathbf{aI}] \begin{bmatrix} \mathbf{b}_1^* \otimes \mathbf{a}_2 \\ \mathbf{b}_1^* \otimes \mathbf{a}_1 + \mathbf{b}_2^* \otimes \mathbf{a}_2 \end{bmatrix} \tag{5.32}$$

$$= \begin{bmatrix} \mathbf{c}_1 \\ \mathbf{c}_2 \end{bmatrix}^T [\mathbf{aI}] \left[\begin{bmatrix} \mathbf{b}_1^* \\ \mathbf{b}_2^* \end{bmatrix} \otimes \begin{bmatrix} \mathbf{a}_2 \\ \mathbf{a}_1 \end{bmatrix} \right] \tag{5.33}$$

$$= \begin{bmatrix} \mathbf{c}_1 \\ \mathbf{c}_2 \end{bmatrix}^T [\mathbf{aI}] \left[\begin{bmatrix} \mathbf{b}_1^* \\ \mathbf{b}_2^* \end{bmatrix} \otimes \left([\mathbf{aI}] \begin{bmatrix} \mathbf{a}_1 \\ \mathbf{a}_2 \end{bmatrix} \right) \right] \tag{5.34}$$

$$= \tilde{\mathbf{c}}^T [\mathbf{aI}] \left(\tilde{\mathbf{b}}^* \otimes ([\mathbf{aI}]\tilde{\mathbf{a}}) \right) \tag{5.35}$$

□

The norm of a dual quaternion is defined as $\|\tilde{\mathbf{q}}\|_{dq} = \tilde{\mathbf{q}}^* \otimes \tilde{\mathbf{q}} = \tilde{\mathbf{q}} \otimes \tilde{\mathbf{q}}^*$. In the case of unit dual quaternions, the norm of the dual quaternion yields

$$\|\tilde{\mathbf{q}}\|_{dq} = \begin{bmatrix} \mathbf{q_I} \\ 0_{4\times1} \end{bmatrix}, \tag{5.36}$$

where $\mathbf{q_I}$ denotes an identity unit quaternion. Note that the norm of a dual quaternion in this sense is a dual quaternion, as distinct from the case of quaternions (the norm of a quaternion is a scalar).

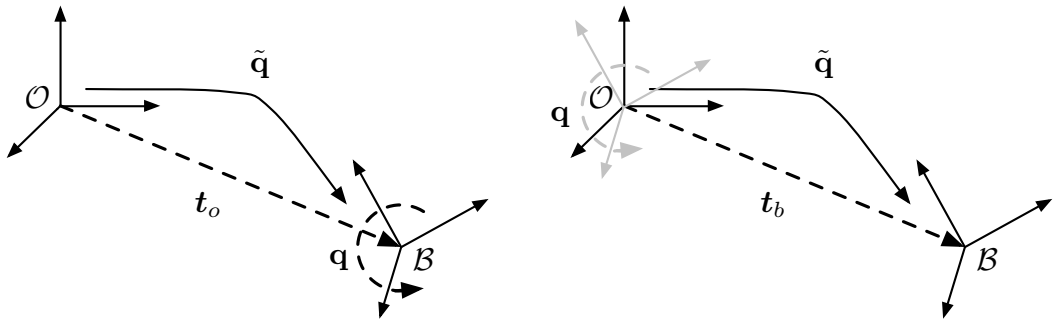

Figure 5.3: The geometric difference between the frame $\mathcal{B}$ and $\mathcal{O}$ can be expressed in two ways: a translation $\boldsymbol{t}_o$ followed by a rotation $\boldsymbol{q}$ [left figure] and a rotation $\boldsymbol{q}$ followed by a translation $\boldsymbol{t}_b$ [right figure], which are represented by the unit dual quaternion $\tilde{\mathbf{q}}$

5.2.4 Unit Dual Quaternions and $\mathsf{SE}(4)$

Suppose that the relationship between the inertially fixed frame $\mathcal{O}$ and the body frame $\mathcal{B}$ is as shown in Fig. 5.3. At each instance, the configuration space for position and orientation of the rigid body is described by a 4×4 homogeneous transformation matrix. $\mathsf{SE}(3)$ is the set of all rigid body transformation in three dimensional space:

$$\mathsf{SE}(3) = \left\{ T \in \mathbb{R}^{4\times 4} \,|\, T = \begin{bmatrix} R & t_o \\ 0 & 1 \end{bmatrix}, \, R \in \mathsf{SO}(3), \, t_o \in \mathbb{R}^3 \right\}, \tag{5.37}$$

where t_o denotes a position vector to the body frame $\mathcal{B}$ with inertial frame components. As unit quaternions parameterize $\mathsf{SO}(3)$, a unit dual quaternion can be used to define a rigid body rotation ($\tilde{\mathbf{q}} \in \mathbf{S}^3 \times \mathbb{R}^3 \mapsto \mathsf{SE}(3)$). The geometric difference between the frame $\mathcal{B}$ with respect to the inertially fixed frame $\mathcal{O}$ can be expressed in two ways. A translation $\boldsymbol{t}_o$ (represented in frame $\mathcal{O}$) followed by a rotation $\mathbf{q}_1$ and a rotation $\mathbf{q}_1$ followed by a translation $\boldsymbol{t}_b$ (represented in frame $\mathcal{B}$), which are represented in the form of *unit dual quaternions* as

$$\tilde{\mathbf{q}} \stackrel{\text{def}}{=} \begin{bmatrix} \mathbf{q} \\ \frac{1}{2}\boldsymbol{t}_o \otimes \mathbf{q} \end{bmatrix} = \begin{bmatrix} \mathbf{q} \\ \frac{1}{2}\mathbf{q} \otimes \boldsymbol{t}_b \end{bmatrix}, \tag{5.38}$$

where $\boldsymbol{t}_o$ and $\boldsymbol{t}_b$ represent the translation vector $\boldsymbol{t}$ with respect to the frames $\mathcal{O}$ and $\mathcal{B}$, respectively. Note that it is easy to check that Eq. (5.38) satisfies Eq. (5.36). Converting

	Unit quaternions	Unit dual quaternions
Governing theorem	Euler's rotation theorem	Chasles' theorem (screw theorem)
Representing group	$\mathsf{SO}(3)$	$\mathsf{SE}(3)$
Operand	vectors in $\mathbb{R}^3$	dual vectors in $\mathbb{R}^3$ / Plücker line
Operator	$v \to v'$ by $v' = \mathbf{q} \otimes v \otimes \mathbf{q}^*$	$\tilde{v} \to \tilde{v}'$ by $\tilde{v}' = \tilde{\mathbf{q}} \otimes \tilde{v} \otimes \tilde{\mathbf{q}}^*$
Degrees of freedom	3	6

Table 5.1: Comparison of unit quaternions and unit dual quaternions

between $\boldsymbol{t}_o$ and $\boldsymbol{t}_b$ is governed by quaternion rotation operator as follows:

$$\boldsymbol{t}_o = \mathbf{q} \otimes \boldsymbol{t}_b \otimes \mathbf{q}^*, \tag{2.35}$$

$$\boldsymbol{t}_b = \mathbf{q}^* \otimes \boldsymbol{t}_o \otimes \mathbf{q}. \tag{2.36}$$

Remark 5.1. *When using position information extracted from the unit dual quaternion, it should be noted that $\boldsymbol{t}_b$ and $\boldsymbol{t}_o$ are represented in two different frames but two vector are rooted in the inertially fixed frame; see Fig. (5.3). As a result, the position vector to the inertially fixed frame $\mathcal{O}$ from the body-fixed frame $\mathcal{B}$ is actually given as $-\boldsymbol{t}_b$.*

5.2.5 Dual Quaternion Transformation Operator

Analogous to the quaternion rotation operator, unit dual quaternions transform a dual vector representing a screw motion in $\mathbb{R}^3$ by having a form of

$$\tilde{v}' = \tilde{\mathbf{q}} \otimes \tilde{v} \otimes \tilde{\mathbf{q}}^*. \tag{5.39}$$

Geometrically, this is interpreted as a "rotation and translation $\tilde{\mathbf{q}}$ of the dual vector $\tilde{v}$" when assuming that $\tilde{v}$ and $\tilde{v}'$ are observed in the same frame. However, a dual vector is not a familiar concept in the current representation and the application to motions in R^3 is not clear. We can look at dual vectors as an extension of conventional vectors lying in $\mathbb{R}^3$ by observing the relationship between unit quaternions and unit dual quaternions. See table 5.1.

5.3 Rigid Body Dynamics in Unit Dual Quaternions

5.3.1 Dual Quaternion Kinematics

The unit dual quaternion kinematic equation is then given as

$$\dot{\tilde{\mathbf{q}}} = \frac{1}{2}\tilde{\mathbf{q}} \otimes \tilde{\boldsymbol{\omega}} \tag{5.40}$$

with

$$\tilde{\boldsymbol{\omega}} = \begin{bmatrix} \boldsymbol{\omega}_b \\ \boldsymbol{v}_b \end{bmatrix}_{8\times 1}, \tag{5.41}$$

where $\boldsymbol{\omega}_b = [\omega_b^T \ 0]^T$ denotes the angular velocity of the rigid body and $\boldsymbol{v}_b = [v_b^T \ 0]^T$ denotes the translational velocity defined by $v_b = \dot{t}_b + \omega_b \times t_b$.

5.3.2 Dual Quaternion Dynamics

The translational and rotational motions of a fully actuated rigid body are expressed by the rate of change of linear and angular momentum through a set of following differential equations [95]:

$$F = \left[\frac{d}{dt}(mv)\right]_{\mathcal{B}} = m\dot{v}_b + \omega_b \times mv_b, \tag{5.42}$$

$$T = \left[\frac{d}{dt}(J\omega)\right]_{\mathcal{B}} = J\dot{\omega}_b + \omega_b \times J\omega_b, \tag{5.43}$$

where $[d(\cdot)/dt]_{\mathcal{B}}$ denotes the time derivative represented in the body frame $\mathcal{B}$ and $m \in \mathbb{R}$ denotes the mass of the rigid body, $J \in \mathbb{R}^{3\times 3} = \texttt{diag}(J_1,\ J_2,\ J_3)$ denotes its inertia matrix along the body frame, and $\omega_b, v_b \in \mathbb{R}^3$ denote, respectively, the angular and translational velocities of the rigid body represented in the body frame. Moreover, F and T denote the external translational force and torque acting on the rigid body, written in the body frame. Note that in order to focus on the feasibility of the dual quaternion-based algorithm, we assume that uncertainties and all external disturbances on the rigid body are negligible.

Lemma 5.2. *Let $\boldsymbol{J}$ be a real block matrix of the form*

$$\boldsymbol{J} = \begin{bmatrix} A & B \\ C & D \end{bmatrix}. \tag{5.44}$$

where A, B, C, D are $n \times n$ matrices and all commute with each other. Then, det $(\boldsymbol{J}) = det(AD - BC)$.

Proof. See ref. [96] □

Proposition 5.3. *The rotational and translational motion dynamics Eqs. (5.43) and (5.42) can be represented in dual quaternions as*

$$\boldsymbol{J}\dot{\tilde{\boldsymbol{\omega}}} + \tilde{\boldsymbol{\omega}} \times \boldsymbol{J}\tilde{\boldsymbol{\omega}} = \tilde{\mathbf{F}} \tag{5.45}$$

where

$$\boldsymbol{J} = \left[\begin{array}{cc|cc} 0_{3\times3} & 0 & m\mathbf{I}_3 & 0 \\ 0 & 0 & 0 & 1 \\ \hline J & 0 & 0_{3\times3} & 0 \\ 0 & 1 & 0 & 0 \end{array}\right]_{8\times8} \quad \textit{and} \quad \tilde{\mathbf{F}} = \begin{bmatrix} F \\ 0 \\ T \\ 0 \end{bmatrix}. \tag{5.46}$$

Moreover, $\boldsymbol{J} \in \mathbb{R}^{8\times8}$ forms a block anti-diagonal matrix and is always invertible.

Proof. Rewriting Eq. (5.45) with Eqs. (5.41) and (5.46) yields

$$\begin{bmatrix} m\dot{\boldsymbol{v}}_b \\ J\dot{\boldsymbol{\omega}}_b \end{bmatrix} + \begin{bmatrix} \boldsymbol{\omega}_b \\ \boldsymbol{v}_b \end{bmatrix} \times \begin{bmatrix} m\boldsymbol{v}_b \\ J\boldsymbol{\omega}_b \end{bmatrix} = \begin{bmatrix} \boldsymbol{F} \\ \boldsymbol{T} \end{bmatrix} \tag{5.47}$$

where $\boldsymbol{F} = [\, F^T, 0\,]^T$ and $\boldsymbol{T} = [\, T^T, 0\,]^T$. Noting that

$$\boldsymbol{v}_b \times m\boldsymbol{v}_b = 0,$$

we have

$$\begin{bmatrix} m\dot{v}_b \\ J\dot{\omega}_b \end{bmatrix} + \begin{bmatrix} \omega_b \times m\boldsymbol{v}_b \\ \omega_b \times J\omega_b \end{bmatrix} = \begin{bmatrix} F \\ T \end{bmatrix}, \tag{5.48}$$

which is identical to Eqs. (5.42) and (5.43). Now, assume that $\boldsymbol{J}$ in Eq. (5.46) has the same form of matrix as Eq. (5.44). Since all 4×4 block matrices are commutative, from *Lemma 5.2* we have

$$\det(\boldsymbol{J}) = \det(-BC) \tag{5.49}$$

$$= \det(B)\, \det(C), \tag{5.50}$$

where B, C denote the right upper and left lower block matrices in $\boldsymbol{J}$ whose determinants are not zero. Thus, $\boldsymbol{J}$ is always invertible. □

Therefore, Eq. (5.40) and Eq. (5.45) constitute the kinematics and dynamics of the rigid body in terms of dual quaternions, considering *integrated* translational and rotational motion. Now, consider the gravitational force applied to the system. The gravitational force is defined as a constant force observed in the inertially fixed frame $\mathcal{O}$ as

$$\mathbf{g}_o = \begin{bmatrix} 0 \\ 0 \\ g \\ 0 \end{bmatrix}, \tag{5.51}$$

where g denotes a gravitational acceleration. Then, using the quaternion rotation operator, the gravitational acceleration observed in the body frame $\mathcal{B}$ is given in the form of a dual quaternion as

$$\tilde{\mathbf{g}}_b = \begin{bmatrix} m\ (\mathbf{q}^* \otimes \mathbf{g}_o \otimes \mathbf{q}) \\ 0_{4\times 1} \end{bmatrix}, \text{ or } \tilde{\mathbf{g}}_b = m\,(\tilde{\mathbf{q}}^* \otimes \tilde{\mathbf{g}}_o \otimes \tilde{\mathbf{q}}). \tag{5.52}$$

where $\tilde{\mathbf{g}}_0 = [\,\mathbf{g}_0^T \quad 0_{1\times 4}\,]^T$. The rotational and translational dynamics as dual quaternions are now given by

$$\boldsymbol{J}\dot{\tilde{\boldsymbol{\omega}}} + \tilde{\boldsymbol{\omega}} \times \boldsymbol{J}\tilde{\boldsymbol{\omega}} = \tilde{\mathbf{F}} + \tilde{\mathbf{g}}_b. \tag{5.53}$$

with Eq. (2.36).

5.4 Feedback Control for Simultaneous Attitude and Position Tracking

Dual quaternion-based simultaneous attitude and position tracking control laws have been examined in only a few research works. For example, in [97], a position and attitude tracking law is suggested based on the feedback of the dual relative velocity and the logarithm of the dual error quaternion. However, the proposed control law does not present the control in terms of a dual quaternion such as $\tilde{\mathbf{F}}$ in Eq. (5.46). Similar to our approach, the authors

of [98] design a tracking law for a leader-follower spacecraft formation using a sliding mode control

Now, consider a strictly convex non-negative (cost) function $V(\tilde{\mathbf{q}})$. Then, the linearity of quaternion kinematics, i.e. $\dot{\tilde{\mathbf{q}}} = \frac{1}{2}\tilde{\mathbf{q}} \otimes \tilde{\boldsymbol{\omega}}$, enables us to derive an almost globally stable control law as follows. Consider a candidate Lyapunov function $V_t : (\tilde{\mathbf{q}}, \tilde{\boldsymbol{\omega}}) \to \mathbb{R}$ expressed as unit dual quaternions as

$$V_t = V(\tilde{\mathbf{q}}) + \frac{1}{2}\tilde{\boldsymbol{\omega}}^T \boldsymbol{J} \tilde{\boldsymbol{\omega}}, \tag{5.54}$$

where

$$\boldsymbol{J} = \left[\begin{array}{cc|cc} 0_{3\times3} & 0 & m\mathbf{I}_3 & 0 \\ 0 & 0 & 0 & 1 \\ \hline J & 0 & 0_{3\times3} & 0 \\ 0 & 1 & 0 & 0 \end{array}\right]. \tag{5.55}$$

Then, $V_t \geq 0$ for all $(\tilde{\mathbf{q}}, \tilde{\boldsymbol{\omega}})$, and the time derivative of V_t along Eqs. (5.40)-(5.45) is given by

$$\dot{V}_t = \nabla V^T \left(\frac{1}{2}\tilde{\mathbf{q}} \otimes \tilde{\boldsymbol{\omega}}\right) + \tilde{\boldsymbol{\omega}}^T \boldsymbol{J} \dot{\tilde{\boldsymbol{\omega}}} \tag{5.56}$$

$$= \tilde{\boldsymbol{\omega}}^T [\mathbf{aI}] \left(\frac{1}{2}\tilde{\mathbf{q}}^* \otimes ([\mathbf{aI}]\nabla V)\right) + \tilde{\boldsymbol{\omega}}^T (-\tilde{\boldsymbol{\omega}} \times \boldsymbol{J}\tilde{\boldsymbol{\omega}} + \tilde{\mathbf{F}}) \tag{5.57}$$

$$= \tilde{\boldsymbol{\omega}}^T \left([\mathbf{aI}] \left(\frac{1}{2}\tilde{\mathbf{q}}^* \otimes ([\mathbf{In}]\nabla V)\right) + \tilde{\mathbf{F}}\right), \tag{5.58}$$

where *Theorem 5.1* is used to obtain Eq.(5.57); $[\mathbf{aI}]$ denotes an 8×8 anti-diagonal identity matrix defined by

$$[\mathbf{aI}] = \left[\begin{array}{cc} 0_{4\times4} & \mathbf{I}_4 \\ \mathbf{I}_4 & 0_{4\times4} \end{array}\right]. \tag{5.59}$$

Note that $\tilde{\boldsymbol{\omega}}^T(-\tilde{\boldsymbol{\omega}} \times \boldsymbol{J}\tilde{\boldsymbol{\omega}}) = 0$ in Eq. (5.57) by the vector identities, which makes the problem more tractable. By taking

$$\tilde{\mathbf{F}} = -\alpha\tilde{\boldsymbol{\omega}} - [\mathbf{aI}] \left(\frac{1}{2}\tilde{\mathbf{q}}^* \otimes ([\mathbf{In}]\nabla V)\right), \tag{5.60}$$

where α denotes a positive weighting parameter, Eq. (5.58) yields

$$\dot{V}_t = -\alpha \tilde{\boldsymbol{\omega}}^T \tilde{\boldsymbol{\omega}} \leq 0. \tag{5.61}$$

This observation justifies the following proposition.

Proposition 5.4. *The proposed control law, Eq. (5.60), makes the cost function V, as well as the combined cost function V_t, asymptotically converge to zero.*

Proof. Consider V_t as a candidate Lyapunov function, and let

$$S = \{\, \tilde{\boldsymbol{\omega}} \,|\, \dot{V}_t = 0 \,\}. \tag{5.62}$$

From Eq. (5.61), one can show

$$\dot{V}_t = 0 \quad \Longrightarrow \quad \tilde{\boldsymbol{\omega}} = [\, \boldsymbol{\omega}_b^T \;\; \boldsymbol{v}_b^T \,]^T = \mathbf{0}, \tag{5.63}$$

implying that $\tilde{\mathbf{F}} = 0$ due to Eq. (5.45). Similarly, given the above conditions, the only condition which leads Eq. (5.60) become identically zero is that

$$\nabla V = \mathbf{0} \text{ and } \tilde{\boldsymbol{\omega}} = 0 \quad \text{because} \quad \tilde{\mathbf{q}} \neq \mathbf{0}. \tag{5.64}$$

Since V is assumed to be strictly convex in $\tilde{\mathbf{q}}$, we have $\nabla V = 0$ iff $V = 0$. Therefore, the invariant set contains a unique minumum $\tilde{\mathbf{q}}_*$ for which $V(\tilde{\mathbf{q}}_*) = 0$, i.e.

$$\{\, \boldsymbol{\omega} \,|\, \dot{V}_t = 0\} \Longleftrightarrow \{\, (\tilde{\mathbf{q}}, \tilde{\boldsymbol{\omega}}) \,|\, V(\tilde{\mathbf{q}}_*) = 0 \text{ and } \tilde{\boldsymbol{\omega}} = \mathbf{0}\}. \tag{5.65}$$

Moreover,

$$\|\tilde{\mathbf{q}}\|, \|\tilde{\boldsymbol{\omega}}\| \to \infty \quad \Rightarrow \quad V_t \to \infty. \tag{5.66}$$

Therefore, by LaSalle's invariance principle [49], the origin $(\tilde{\mathbf{q}}_*, \tilde{\boldsymbol{\omega}} = 0)$ is *almost* globally asymptotically stable. □

Remark 5.2. *Note that the terminology "almost global" still exists with unit dual quaternions due to the simple fact that $\tilde{\mathbf{q}}$ and $-\tilde{\mathbf{q}}$ represent identical position and orientation in* $\mathsf{SE}(3)$ *configuration space; this can be easily checked by Eq. (5.38).*

Now, let us propose a strictly convex cost function V to represent the potential between two distinct unit dual quaternions as

$$V(\tilde{\mathbf{q}}) = \|\tilde{\mathbf{q}}_r - \tilde{\mathbf{q}}\|^2 \tag{5.67}$$

where $\tilde{\mathbf{q}}_r$ denotes a desired unit dual quaternion. Note that as discussed in Chapter 2, quaternions, as well as dual quaternions, are not Euclidean. However, we can employ a Euclidean metric to measure a distance on the dual quaternion manifold since the Euclidean norm grows proportionally to the actual arc length. Therefore, analogously to the treatment addressed in §2.4, given the current $\tilde{\mathbf{q}}$ and the desired $\tilde{\mathbf{q}}_r$, we find that a desired unit dual quaternion is updated to $\tilde{\mathbf{q}}_r$ and $-\tilde{\mathbf{q}}_r$ depending on the choice that yields the smaller chord length. With a properly chosen $\tilde{\mathbf{q}}_d$, combining Eq. (5.1) with Eq. (5.54), the total cost function for the tracking problem is proposed as

$$V_t = \|\tilde{\mathbf{q}}_r - \tilde{\mathbf{q}}\|^2 + \frac{1}{2}\tilde{\boldsymbol{\omega}}^T \boldsymbol{J}\, \tilde{\boldsymbol{\omega}}, \tag{5.68}$$

and the corresponding almost globally stabilizing control law for the tracking is given by

$$\tilde{\mathbf{F}} = -\alpha\tilde{\boldsymbol{\omega}} - [\mathbf{aI}]\left(\frac{1}{2}\tilde{\mathbf{q}}^* \otimes (2[\mathbf{In}](\tilde{\mathbf{q}} - \tilde{\mathbf{q}}_r))\right), \tag{5.69}$$

$$= -\alpha\tilde{\boldsymbol{\omega}} - [\mathbf{aI}]\left(\tilde{\mathbf{q}}^* \otimes [\mathbf{In}]\tilde{\mathbf{q}} - \tilde{\mathbf{q}}^*[\mathbf{In}] \otimes \tilde{\mathbf{q}}_r)\right). \tag{5.70}$$

Note that the control law presented above shows that position and attitude controls are coupled and represented by a dual quaternion variable $\tilde{\mathbf{q}}^*$.

Remark 5.3. *The motions are associated through the attitude variable* $\mathbf{q}$*. This is intuitive if viewed in the context of the inertial frame, where pure translational motion in one frame can be seen as combined translational and rotational motions in the other, e.g., a satellite revolving around earth requires a rotational maneuver to keep pointing a body-fixed antenna towards Earth's surface.*

5.5 Rotationally and Translationally Constrained Zone

One of the challenging algorithmic aspects of the powered-descent guidance problem is that translational and rotational dynamics of spacecraft are generally taken into account independently. Thus it becomes difficult to handle situations where translational and rotational

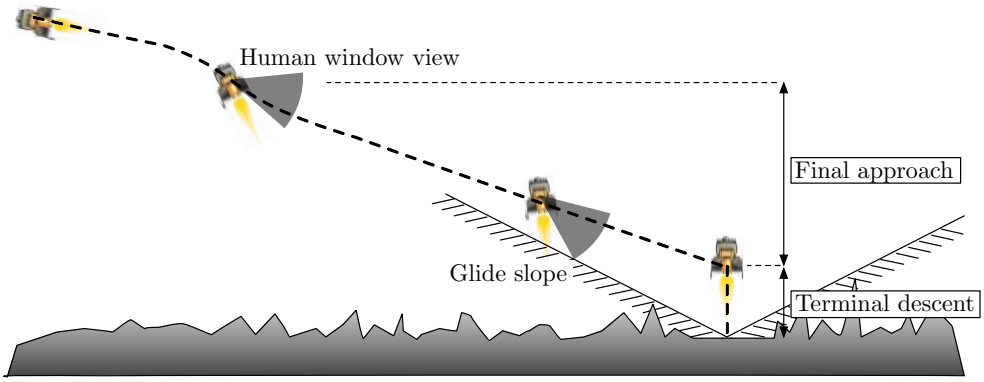

Figure 5.4: Power-descent scenario in the presence of human window view and glide slope constraints

dynamics are coupled through constraints. For example, it is often required that the lander should keep the thruster angle θ within 90 deg of the vertical axis while landing. However, such situations can more directly be approached via a dual quaternion notation and the corresponding algorithms. In this section, we develop rotationally and translationally constrained zones in the rigid-body motion's configuration space. Such constraints are involved in not only a rigid-body's translational positions but also its orientation. Since this framework was originally inspired by a power-descent guidance algorithm for the Mars lander, let us formulate the unit dual quaternion-based constrained zones to fit in such an application; see Fig. 5.4 for the overall landing scenario.

5.5.1 Human Window View Constraints

The human window view constraint can be defined as a cone around a boresight vector in the body frame $\mathcal{B}$ (see Fig. 5.5). We assume that the frame $\mathcal{O}$ lies on the landing site. Consider that the body frame $\mathcal{B}$ is initially aligned to the frame $\mathcal{O}$ and subject to translation and rotation by $\tilde{\mathbf{q}}$. Thus, at a specific time, whether the human view boresight vector $\boldsymbol{y}_b$ in the frame $\mathcal{B}$ stays within θ around the direction to the target $\boldsymbol{t}_b$ in the frame $\mathcal{O}$ can be expressed by the inner product

$$-\boldsymbol{t}_b \cdot \boldsymbol{y}_b \geq \|\boldsymbol{t}_b\| \cos\theta, \tag{5.71}$$

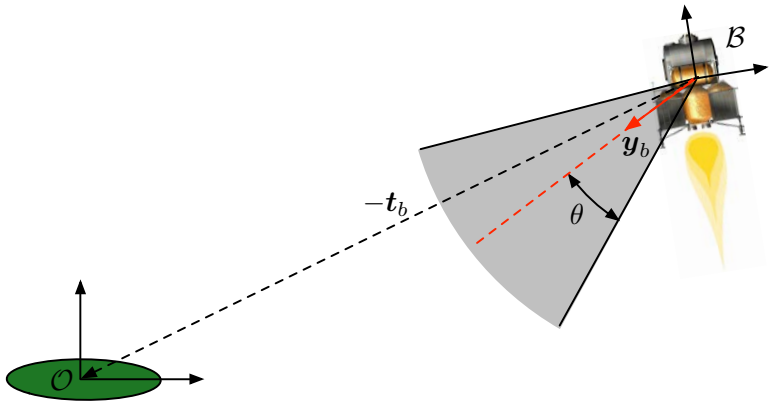

Figure 5.5: Illustration of human view constraint. It is defined as a cone around the fixed boresight vector $\boldsymbol{y}$ in the body frame.

where $\boldsymbol{t}_b$ denotes a translation vector represented in the frame $\mathcal{B}$. Note that Eq. (5.71) holds for $-\pi \leq \theta \leq \pi$.

Then one can show that the left hand side of the above equation can be expressed by a quadratic function as

$$\begin{aligned}
\boldsymbol{t}_b \cdot \boldsymbol{y}_b &= (\mathbf{q}_1 \otimes \mathbf{t}_b)^T (\mathbf{q}_1 \otimes \mathbf{y}_b) && (5.72)\\
&= (\mathbf{q}_1 \otimes \mathbf{t}_b)^T [\mathbf{y}_b]^*_{\otimes}\, \mathbf{q}_1 && (5.73)\\
&= \begin{bmatrix} \mathbf{q}_1 \\ \frac{1}{2}\mathbf{q}_1 \otimes \boldsymbol{t}_b \end{bmatrix}^T \begin{bmatrix} 0_{4\times4} & [\mathbf{y}_b]^{*\,T}_{\otimes} \\ [\mathbf{y}_b]^*_{\otimes} & 0_{4\times4} \end{bmatrix} \begin{bmatrix} \mathbf{q}_1 \\ \frac{1}{2}\mathbf{q}_1 \otimes \boldsymbol{t}_b \end{bmatrix} \\
&= \tilde{\mathbf{q}}^T M_H \tilde{\mathbf{q}}, && (5.74)
\end{aligned}$$

where $\tilde{\mathbf{q}}$ denotes a unit dual quaternion and the quaternion properties Eqs. (2.21) and (2.28) have been applied. We note that M_H forms an indefinite symmetric matrix.

In addition, inspired by Eq. (2.28), we can find the following useful identities:

$$\tilde{\mathbf{q}}^T \tilde{\mathbf{q}} = \|\tilde{\mathbf{q}}\|^2 = 1 + \frac{1}{4}\|\boldsymbol{t}_b\|^2, \tag{5.75}$$

$$\tilde{\mathbf{q}}^T E_u \tilde{\mathbf{q}} = 1, \quad 4\,\tilde{\mathbf{q}}^T E_d \tilde{\mathbf{q}} = \|\boldsymbol{t}_b\|^2, \text{ and} \tag{5.76}$$

$$\|\boldsymbol{t}_b\| = \|2\,E_d \tilde{\mathbf{q}}\| \tag{5.77}$$

where

$$E_u = \begin{bmatrix} \mathbf{I}_4 & 0_{4\times4} \\ 0_{4\times4} & 0_{4\times4} \end{bmatrix}, \quad E_d = \begin{bmatrix} 0_{4\times4} & 0_{4\times4} \\ 0_{4\times4} & \mathbf{I}_4 \end{bmatrix}. \tag{5.78}$$

Rewriting Eq. (5.71) with the above identities, we obtain

$$f_1(\tilde{\mathbf{q}}) = \tilde{\mathbf{q}}^T M_H \tilde{\mathbf{q}} + \|2\, E_d \tilde{\mathbf{q}}\| \cos\theta \leq 0, \tag{5.79}$$

where we note that the unit dual quaternion $\tilde{\mathbf{q}}$ is defined as an open set over $\mathbb{R}^3$ since $\boldsymbol{t}_b \in \mathbb{R}^3$. Consider a closed subset of $\mathbb{R}^3$ as

$$\|\boldsymbol{t}_b\| \leq \delta. \tag{5.80}$$

Correspondingly, we define the identical set in $\tilde{\mathbf{q}}$ as

$$\tilde{\mathbf{q}}^T \tilde{\mathbf{q}} \;\leq\; 1 + \frac{1}{4}\delta^2. \tag{5.81}$$

Then, one can show that the left hand side of Eq. (5.79) is convex over the defined closed subset.

Proposition 5.5. *Suppose the quadratic function $f : \tilde{\mathbf{q}} \to \mathbb{R}$ is given by*

$$f_1(\tilde{\mathbf{q}}) = \tilde{\mathbf{q}}^T M_H \tilde{\mathbf{q}} + \|2\, E_d \tilde{\mathbf{q}}\| \cos\theta \leq 0 \tag{5.79}$$

with

$$\mathbf{dom}\, f_1 = \left\{ \tilde{\mathbf{q}} \in (\mathbf{S}^3 \times \mathbb{R}^3) \mid \tilde{\mathbf{q}}^T \tilde{\mathbf{q}} \;\leq\; 1 + \frac{1}{4}\delta^2 \right\}, \tag{5.82}$$

where $\delta \in \mathbb{R}$. M_H and E_d are defined in Eqs. (5.74) and (5.78) respectively. Then f_1 is convex regardless of θ.

Proof. From the property of unit dual quaternions, Eq. (5.76), we have

$$\delta^2(\tilde{\mathbf{q}}^T E_u \tilde{\mathbf{q}}) - \delta^2 = 0. \tag{5.83}$$

Adding it into Eq. (5.79) yields

$$f_1 = \tilde{\mathbf{q}}^T M_H \tilde{\mathbf{q}} + \|2\, E_d \tilde{\mathbf{q}}\| \cos\theta + \delta^2(\tilde{\mathbf{q}}^T E_u \tilde{\mathbf{q}}) - \delta^2. \tag{5.84}$$

Note that f_1 is twice differentiable. Using the fact that

$$\tilde{\mathbf{q}}^T \left(\frac{d^2}{d\,\tilde{\mathbf{q}}^2} \|2E_d\tilde{\mathbf{q}}\| \right) \tilde{\mathbf{q}} = 0, \tag{5.85}$$

the quadratic form of the *Hessian* of f_1 with $\tilde{\mathbf{q}}$ now has the simple form of

$$\tilde{\mathbf{q}}^T(\nabla^2 f_1)\tilde{\mathbf{q}} = 2(\tilde{\mathbf{q}}^T M_H \tilde{\mathbf{q}}) + 2\delta^2(\tilde{\mathbf{q}}^T E_u \tilde{\mathbf{q}}) \tag{5.86}$$

$$= 2(\boldsymbol{t}_b \cdot \boldsymbol{y}_b + \delta^2). \tag{5.87}$$

It is simple to show that $\boldsymbol{t}_b \cdot \boldsymbol{y}_b + \delta^2 \geq 0$ on $\mathbf{dom}\, f_1$. Since $\boldsymbol{y}_b$ is a unit vector, we know

$$-\|\boldsymbol{t}_b\|^2 \leq \boldsymbol{t}_b \cdot \boldsymbol{y}_b \leq \|\boldsymbol{t}_b\|^2. \tag{5.88}$$

Due to Eq. (5.80), we obtain

$$\nabla^2 f_1(\tilde{\mathbf{q}}) \succeq 0. \tag{5.89}$$

and f_1 is convex on $\mathbf{dom}\, f$. □

Remark 5.4. *Similarly, we can show that the case in which the human view boresight vector $\boldsymbol{y}_b$ always stay outside of θ around the direction to the target $\boldsymbol{t}_b$ with*

$$\boldsymbol{t}_b \cdot \boldsymbol{y}_b \leq \|\boldsymbol{t}_b\| \cos\theta \tag{5.90}$$

is convex on the same given domain. This can be done because in Eq. (5.82), we can find that $\tilde{\mathbf{q}}^T\tilde{\mathbf{q}}$ is naturally lower bounded by 1 such that $1 \leq \tilde{\mathbf{q}}^T\tilde{\mathbf{q}} \leq 1 + \delta^2/4$, which allows the Hessian remain positive semidefinite on its domain.

5.5.2 Glide Slope Constraints

The glide slope constraint is defined as a cone around the fixed vector $\boldsymbol{z}_o$ that lies in the frame $\mathcal{O}$. See the illustration in Fig. 5.6. Note that the glide slope constraint only depends on the position of the frame $\mathcal{B}$. Similar to the human window view constraint, we find the condition with which the glide slope constraint is satisfied as

$$\boldsymbol{t}_o \cdot \boldsymbol{z}_o \geq \|\boldsymbol{t}_o\| \cos\phi, \tag{5.91}$$

where $\boldsymbol{z}_o$ and $\boldsymbol{t}_o$ denote a unitized y axis vector and a position vector to frame $\mathcal{B}$ respectively. Note that they are represented with respect to frame $\mathcal{O}$. We reasonably define $0 < \phi \leq \frac{1}{2}\pi$.

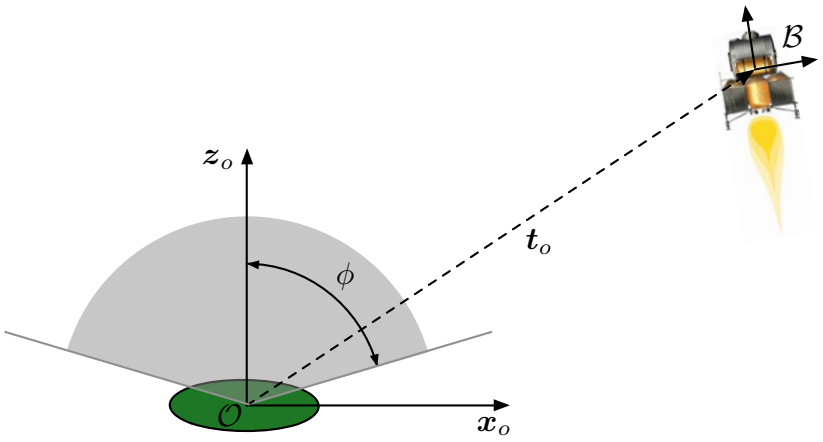

Figure 5.6: Illustration of the glide slope constraint. The constrained zone is defined as a cone around the inertially fixed vector $\boldsymbol{z}_o$ and angle ϕ.

Proposition 5.6. *The glide slope constraint can be represented in terms of the unit dual quaternion* $\tilde{\mathbf{q}}$ *as*

$$f_2(\tilde{\mathbf{q}}) = -\tilde{\mathbf{q}}^T M_G \tilde{\mathbf{q}} + \|2\, E_d \tilde{\mathbf{q}}\| \cos\phi \leq 0 \tag{5.92}$$

where

$$M_G = \begin{bmatrix} 0_{4\times4} & [\mathbf{z}_o]_\otimes{}^T \\ [\mathbf{z}_o]_\otimes & 0_{4\times4} \end{bmatrix}, \quad E_d = \begin{bmatrix} 0_{4\times4} & 0_{4\times4} \\ 0_{4\times4} & \mathbf{I}_4 \end{bmatrix} \tag{5.93}$$

with $\mathbf{z}_o = [\,\boldsymbol{z}_o^T \;\; 0\,]^T = [\,0 \;\; 0 \;\; 1 \;\; 0\,]^T$. *Then* $f_2 : \tilde{\mathbf{q}} \to \mathbb{R}$ *is convex on* $\mathbf{dom}\, f_2 = \{\tilde{\mathbf{q}} \in (\mathbf{S}^3 \times \mathbb{R}^3) \mid \tilde{\mathbf{q}}^T \tilde{\mathbf{q}} \leq 1 + \frac{1}{4}\delta^2\}$.

Proof. The left hand side of Eq. (5.91) is rewritten as follows

$$\begin{aligned} \boldsymbol{t}_o \cdot \boldsymbol{z}_o &= (\boldsymbol{t}_o \otimes \mathbf{q}_1)^T (\boldsymbol{z}_o \otimes \mathbf{q}_1) && (5.94)\\ &= (\boldsymbol{t}_o \otimes \mathbf{q}_1)^T [\mathbf{z}_o]_\otimes \mathbf{q}_1 && (5.95)\\ &= \begin{bmatrix} \mathbf{q}_1 \\ \frac{1}{2}\boldsymbol{t}_o \otimes \mathbf{q}_1 \end{bmatrix}^T \begin{bmatrix} 0_{4\times4} & [\mathbf{z}_o]_\otimes{}^T \\ [\mathbf{z}_o]_\otimes & 0_{4\times4} \end{bmatrix} \begin{bmatrix} \mathbf{q}_1 \\ \frac{1}{2}\boldsymbol{t}_o \otimes \mathbf{q}_1 \end{bmatrix} \\ &= \tilde{\mathbf{q}}^T M_G \tilde{\mathbf{q}}, && (5.96) \end{aligned}$$

where M_G denotes an indefinite symmetric matrix. Thus we obtain Eq. (5.92). The rest of the proof is analogous to the proof in *Proposition 5.5.* In $\mathbf{dom}\, f_2$, we can rewrite Eq. (5.92) as

$$f_2(\tilde{\mathbf{q}}) = \tilde{\mathbf{q}}^T M_G \tilde{\mathbf{q}} + \|2\, E_d \tilde{\mathbf{q}}\| \cos\phi + \delta^2(\tilde{\mathbf{q}}^T E_u \tilde{\mathbf{q}}) - \delta^2. \tag{5.97}$$

The quadratic form of the *Hessian* of f_2 yields

$$\tilde{\mathbf{q}}^T(\nabla^2 f_2)\tilde{\mathbf{q}} = 2(-\boldsymbol{t}_o \cdot \boldsymbol{y}_o + \delta^2). \tag{5.98}$$

Since $\|t_o\| = \|t_b\|$, we have

$$-\boldsymbol{t}_o \cdot \boldsymbol{y}_o + \delta^2 \geq 0 \tag{5.99}$$

on $\mathbf{dom}\, f_2$ from Eq. (5.80). Note that $\boldsymbol{y}_o$ is a unit vector. Thus,

$$\nabla^2 f_2(\tilde{\mathbf{q}}) \succeq 0, \tag{5.100}$$

and $f_2(\tilde{\mathbf{q}})$ is convex on $\mathbf{dom}\, f_2$, which concludes the proof. □

Remark 5.5. *The aforementioned two different constraints form an analogous formulation in terms of unit dual quaternions. This is because a unit dual quaternion can be represented either with the inertial frame component or with the body frame component, and both yielding the same quantity, as we observe from Eq. (5.38).*

5.5.3 General Spacecraft Attitude Constraints

Generally, the spacecraft's rotational maneuvers are restricted to a certain angle about inertially fixed axes. For example, there may be a camera onboard that has to be directed to the ground for a majority of the time during the descent, or, as seen in the Fig 5.7, the sky crane system used in the Mars Science Laboratory (MSL) mission by NASA is required to keep changes in the angle ψ minimal to avoid getting tangled in attached wires while maneuvering. Such rotational movements can be captured by the angle between inertially fixed vector z_o and the body-fixed vector z_b; see Fig. 5.8. In this formulation, we define an

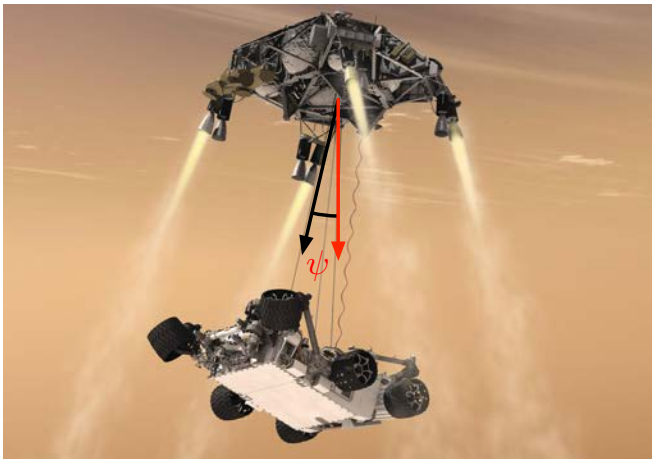

Figure 5.7: Curiosity is being lowered by the sky crane, whose rotational maneuvers are limited by the angle ψ. This angle should be maintained below a certain limit in all situations. Courtesy of NASA/JPL-Caltech

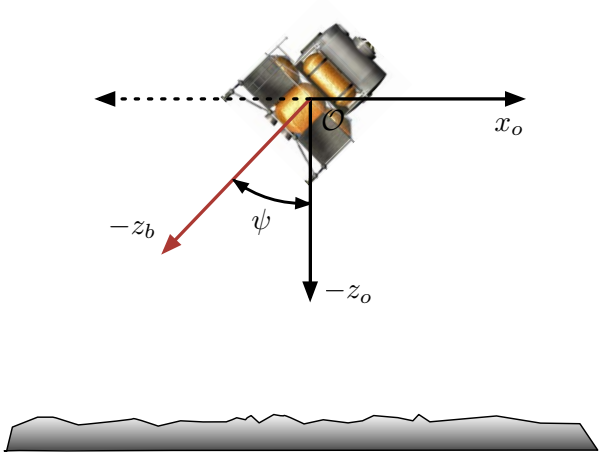

Figure 5.8: General spacecraft attitude constraint

inequality constraint as follows:

$$\boldsymbol{z}_o \cdot [\boldsymbol{z}_b]_{\mathcal{O}} \geq \cos\psi, \tag{5.101}$$

where $\boldsymbol{z}_o$ denotes a unitized inertially fixed vector and $[\boldsymbol{z}_b]_{\mathcal{O}}$ denotes a unitized body-fixed vector $\boldsymbol{z}_b$ represented in the inertial frame $\mathcal{O}$.

Proposition 5.7. *The aforementioned general spacecraft attitude constraint can be formulated in terms of the unit dual quaternion* $\tilde{\mathbf{q}}$ *as*

$$f_3(\tilde{\mathbf{q}}) = \tilde{\mathbf{q}}^T M_A \tilde{\mathbf{q}} \leq 0 \tag{5.102}$$

where

$$M_A = \begin{bmatrix} [\mathbf{z}_o]_{\otimes}^T [\mathbf{z}_b]_{\otimes}^* + \cos\psi\, \mathbf{I}_4 & 0_{4\times 4} \\ 0_{4\times 4} & \cos\psi\, \mathbf{I}_4 \end{bmatrix}_{8\times 8} \tag{5.103}$$

and $\mathbf{z}_o = [\boldsymbol{z}_o^T\ 0]^T$ *and* $\mathbf{z}_b = [\boldsymbol{z}_b^T\ 0]^T$.

Then $f_3 : \tilde{\mathbf{q}} \to \mathbb{R}$ on $\mathbf{dom}\, f_3 = \{\tilde{\mathbf{q}} \in (\mathcal{S}^3 \times \mathbb{R}^3) \mid \tilde{\mathbf{q}}^T \tilde{\mathbf{q}} \leq 1 + \frac{1}{4}\delta^2\}$ is convex.

Proof. First note that $\boldsymbol{z}_b$ is observed in the body frame $\mathcal{B}$. By Eq. (2.35), it can be represented with the components of the inertial frame $\mathcal{O}$. Then according to the quaternion rotation operator Eq. (2.35), it follows that

$$\mathbf{z}_o^T (\mathbf{q}_1 \otimes \mathbf{z}_b \otimes \mathbf{q}_1^*) \geq 0. \tag{5.104}$$

Using the algebraic quaternion properties presented in Chapter 2, we have

$$(\mathbf{z}_o \otimes \mathbf{q}_1)^T (\mathbf{q}_1 \otimes \mathbf{z}_b \otimes \mathbf{q}_1^* \otimes \mathbf{q}_1) \geq 0 \tag{5.105}$$

$$(\mathbf{z}_o \otimes \mathbf{q}_1)^T (\mathbf{q}_1 \otimes \mathbf{z}_b) \geq 0 \tag{5.106}$$

$$\mathbf{q}_1^T ((\mathbf{z}_o \otimes \mathbf{q}_1) \otimes \mathbf{z}_b^*) \geq 0 \tag{5.107}$$

$$\mathbf{q}_1^T (\mathbf{z}_o \otimes (\mathbf{q}_1 \otimes \mathbf{z}_b)) \leq 0 \tag{5.108}$$

$$\mathbf{q}_1^T (\mathbf{z}_o \otimes (\mathbf{q}_1 \otimes \mathbf{z}_b)) \leq 0 \tag{5.109}$$

$$\mathbf{q}_1^T [\mathbf{z}_o]_{\otimes}^T [\mathbf{z}_b]_{\otimes}^* \mathbf{q}_1 \leq 0 \tag{5.110}$$

$$\tilde{\mathbf{q}}^T M_A \tilde{\mathbf{q}} \leq 0, \tag{5.111}$$

where $\tilde{\mathbf{q}} = \begin{bmatrix} \mathbf{q}_1^T & \frac{1}{2}(\mathbf{t}_o \otimes \mathbf{q}_1)^T \end{bmatrix}^T$ and

$$M_A = \begin{bmatrix} [\mathbf{z}_o]_{\otimes}^T [\mathbf{z}_b]_{\otimes}^* + \cos\psi\, \mathbf{I}_4 & 0_{4\times 4} \\ 0_{4\times 4} & \cos\psi\, \mathbf{I}_4 \end{bmatrix}_{8\times 8}. \tag{5.112}$$

Note that $\boldsymbol{z}_o, \boldsymbol{z}_b \in \mathbb{R}^3$ results in

$$[\mathbf{z}_o]_{\otimes}^T [\mathbf{z}_b]_{\otimes}^* = \begin{bmatrix} [\boldsymbol{z}_o]_{\times}^T & -\boldsymbol{z}_o \\ \boldsymbol{z}_o^T & 0 \end{bmatrix} \begin{bmatrix} [\boldsymbol{z}_b]_{\times}^T & \boldsymbol{z}_b \\ -\boldsymbol{z}_b^T & 0 \end{bmatrix} \tag{5.113}$$

$$= \begin{bmatrix} [\boldsymbol{z}_o]_{\times}^T [\boldsymbol{z}_b]_{\times}^T + \boldsymbol{z}_o \boldsymbol{z}_b^T & (\boldsymbol{z}_b \times \boldsymbol{z}_o) \\ (\boldsymbol{z}_b \times \boldsymbol{z}_o)^T & z_o^T \boldsymbol{z}_b \end{bmatrix}. \tag{5.114}$$

Thus M_A forms a symmetric matrix. Utilizing the fact that $([\mathbf{z}_o]_{\otimes}^T [\mathbf{z}_b]_{\otimes}^*)^T ([\mathbf{z}_o]_{\otimes}^T [\mathbf{z}_b]_{\otimes}^*) = \mathbf{I}_4$, we obtain

$$\begin{gathered} ([\mathbf{z}_o]_{\otimes}^T [\mathbf{z}_b]_{\otimes}^*)\boldsymbol{v} = \lambda \boldsymbol{v} \\ ([\mathbf{z}_o]_{\otimes}^T [\mathbf{z}_b]_{\otimes}^*)^T ([\mathbf{z}_o]_{\otimes}^T [\mathbf{z}_b]_{\otimes}^*)\boldsymbol{v} = \lambda ([\mathbf{z}_o]_{\otimes}^T [\mathbf{z}_b]_{\otimes}^*)\boldsymbol{v}, \\ \left(\mathbf{I}_4 - \lambda_p^2\right)\boldsymbol{v} = 0, \end{gathered}$$

where λ denotes an eigenvalue of $([\mathbf{z}_o]_{\otimes}^T [\mathbf{z}_b]_{\otimes}^*)$, and $\boldsymbol{v}$ is the corresponding eigenvector. The eigenvalues of $([\mathbf{z}_o]_{\otimes}^T [\mathbf{z}_b]_{\otimes}^*)$, on the other hand, are

$$\lambda = -1,\ -1,\ 1,\ 1. \tag{5.115}$$

Now, rewrite Eq. (5.102) as

$$f_3 = \tilde{\mathbf{q}}^T M_A \tilde{\mathbf{q}} + \tilde{\mathbf{q}}^T E_u \tilde{\mathbf{q}} - 1 \tag{5.116}$$

where E_u is presented in Eq. (5.76). The quadratic form of the *Hessian* of f_3 is calculated by

$$\tilde{\mathbf{q}}^T (\nabla^2 f_3) \tilde{\mathbf{q}} = 2\mathbf{q}^T ([\mathbf{z}_o]_{\otimes}^T [\mathbf{z}_b]_{\otimes}^*)\mathbf{q} + 2\mathbf{q}^T \mathbf{q} \tag{5.117}$$

$$= 2\mathbf{q}^T ([\mathbf{z}_o]_{\otimes}^T [\mathbf{z}_b]_{\otimes}^* + \mathbf{I}_4)\mathbf{q} \tag{5.118}$$

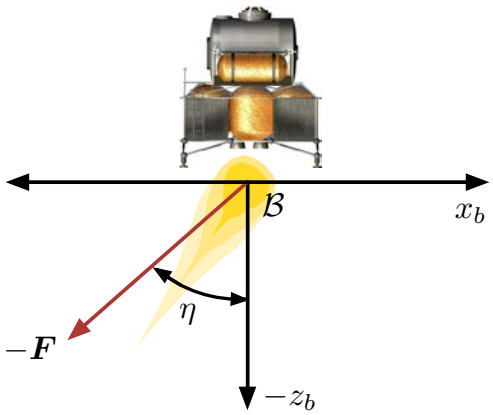

Figure 5.9: Net thrust direction constraint

Since the eigenvalues of $[\mathbf{z}_o]_{\otimes}^T[\mathbf{z}_b]_{\otimes}^*$ are greater than -1, we conclude that $[\mathbf{z}_o]_{\otimes}^T[\mathbf{z}_b]_{\otimes}^* + \mathbf{I}_4 \succeq 0$. Thus,

$$\nabla^2 f_3(\tilde{\mathbf{q}}) \succeq 0 \tag{5.119}$$

and $f_3(\tilde{\mathbf{q}})$ is convex. □

Note that this constraint is convex on the entire domain of the unit dual quaternion $\tilde{\mathbf{q}} \in (\mathbf{S}^3 \times \mathbb{R}^3)$. The proof presented here is inspired by an analogous argument presented with *unit quaternions* in [26].

5.5.4 Thrust Direction Constraints

When the spacecraft is treated as a point mass with a single thrust vector representing the net thrust, it can be assumed that the net thrust on the spacecraft can be pointed arbitrarily. However, in the case of a rigid body model, there should be an extra pointing constraint on the net thrust since in reality, the thrusters can not be attached on all 6 sides of the body. This may imply that the thrust direction should not deviate more than the angle η from the z body axis as depicted in Fig. (5.9). In this section, this type of constraint

is represented as follows:

$$\boldsymbol{z}_b \cdot \frac{\boldsymbol{F}(t)}{\|\boldsymbol{F}(t)\|} \geq \cos\eta, \tag{5.120}$$

where $\boldsymbol{z}_b$ denotes a body-fixed $\boldsymbol{z}$ axis and F denotes the net thrust vector represented in the body-fixed frame $\mathcal{B}$. Clearly, this type of constraint on the net thrust vector defines a convex set, as we can express it as a second order cone constraint. Let us reasonably define $-90^\circ \leq \eta \leq 90^\circ$. Then, Eq. (5.120) yields

$$f_4(\boldsymbol{F}) = -\boldsymbol{z}_b^T \boldsymbol{F}(t) + \cos\eta\|\boldsymbol{F}(t)\| \leq 0. \tag{5.121}$$

5.6 Convex Programming for Power-Descent Guidance for Mars Lander

5.6.1 Constrained Minimum Pinpoint Landing Error Problem

In this section, we describe the trajectory optimization problem for a Mars pinpoint landing, subject to rotationally and translationally constrained zones. The problem formulation consists of the spacecraft rotational and translational dynamics in terms of dual quaternions, rotationally- and translationally-related state constraints, and general control- and state-constrained bounds. Then, the minimum pinpoint landing error problem with convexified

dual quaternion constraints is formulated as follows:

Problem 1:

$$\min \int_0^{t_f} \|\tilde{\mathbf{q}}(t_f) - \tilde{\mathbf{q}}\|^2 + \|\tilde{\boldsymbol{\omega}}(t_f) - \tilde{\boldsymbol{\omega}}\|^2 dt \tag{5.122}$$

subject to:

$$\boldsymbol{J}\dot{\tilde{\boldsymbol{\omega}}} + \tilde{\boldsymbol{\omega}} \times \boldsymbol{J}\tilde{\boldsymbol{\omega}} = \tilde{\mathbf{F}} + \tilde{\mathbf{g}}_b, \tag{5.53}$$

$$\dot{\tilde{\mathbf{q}}} = \frac{1}{2}\tilde{\mathbf{q}} \otimes \tilde{\boldsymbol{\omega}}, \tag{5.40}$$

$$f_1(\tilde{\mathbf{q}}) = \tilde{\mathbf{q}}^T M_H \tilde{\mathbf{q}} + \|2\, E_d \tilde{\mathbf{q}}\| \cos\theta \leq 0, \tag{5.79}$$

$$f_2(\tilde{\mathbf{q}}) = -\tilde{\mathbf{q}}^T M_G \tilde{\mathbf{q}} + \|2\, E_d \tilde{\mathbf{q}}\| \cos\phi \leq 0, \tag{5.92}$$

$$f_3(\tilde{\mathbf{q}}) = \tilde{\mathbf{q}}^T M_A \tilde{\mathbf{q}} \leq 0, \tag{5.102}$$

$$f_4(\boldsymbol{F}) = -\boldsymbol{z}_b^T \boldsymbol{F}(t) + \cos\eta \|\boldsymbol{F}(t)\| \leq 0, \tag{5.121}$$

$$\|\tilde{\mathbf{q}}\|^2 \leq \zeta_{\tilde{\mathbf{q}}} \tag{5.123}$$

$$\|\omega_i\| \leq \zeta_{\tilde{\boldsymbol{\omega}}_i}, \quad \|F_i\| \leq \zeta_{F_i}, \quad i = 1, .., 8, \tag{5.124}$$

$$\tilde{\mathbf{q}}(0) = \tilde{\mathbf{q}}_0, \quad \tilde{\mathbf{q}}(t_f) = \tilde{\mathbf{q}}_{t_f}, \tag{5.125}$$

$$\tilde{\boldsymbol{\omega}}(0) = \tilde{\boldsymbol{\omega}}_0, \quad \tilde{\boldsymbol{\omega}}(t_f) = \mathbf{0}, \tag{5.126}$$

where $\zeta_{\tilde{\mathbf{q}}} = 1 + \frac{1}{4}\delta^2$ denotes the boundary of feasible positions from Eq. (5.81), and $\zeta_{\tilde{\boldsymbol{\omega}}}$ and $\zeta_{\tilde{\mathbf{F}}}$ denote the bounds on velocities and external forces, respectively. Note that the domains of f_1, f_2, and f_3 are parameterized by the constraint $\|\tilde{\mathbf{q}}\| \leq \zeta_{\tilde{\mathbf{q}}}$ into the problem. We consider, in the formulation, the rotational and translational motion constraint Eqs. (5.79),(5.92),(5.102) as hard constraints which must be satisfied during the given period of time.

In the previous chapter, we have shown that the proposed four types of rotation and translation related constraints in unit dual quaternion can be *convexified* over the close subset of unit dual quaternions. This observation would completely solve the constrained rigid body motion control if the nonlinear kinematic and dynamic equations could be seamlessly augmented to the convex program. However, the nature of rotational motions governed by the nonlinear differential equations destroy the convexity of the corresponding feasible set. We could count on the linearization of dynamics. Such a linearization scheme, on the other

hand, brings in integration errors and lead the iterates to leave the unit dual quaternion manifold. Nevertheless, the error resulting from the linearization can be predictable and reducible by projecting them on the respective manifold.

5.6.2 Discretization

This section describes the discretization of the aforementioned control problem and develop a numerical algorithm to solve the resulting discrete version of the problem. The discretization of Problem 1 converts the infinite dimensional optimization problem to a finite-dimensional one by discretizing the time domain into equal time intervals and imposing convex constraints at the temporal nodes. Because the constraints are quadratic and linear, the resulting problem becomes a finite-dimensional quadratically constrained quadratic program which can be efficiently solved by available convex programming solver. We discretize the kinematic and dynamic equations in the problem formulation via Euler's first order discretization method as

$$\dot{\tilde{\mathbf{q}}} \simeq \frac{\tilde{\mathbf{q}}(t+1) - \tilde{\mathbf{q}}(t)}{\Delta t}, \tag{5.127}$$

with a sampling time of Δt. The original problem formulation is subsequently transformed into finding a dual quaternion force $\tilde{\mathbf{F}}(t)$ for $t = 0, ..., N-1$, such that it satisfies the initial and terminal conditions

$$\tilde{\boldsymbol{\omega}}(0), \tilde{\mathbf{q}}(0) \quad \text{and} \quad \tilde{\boldsymbol{\omega}}(N), \tilde{\mathbf{q}}(N) \tag{5.128}$$

as well as state bounds and convex constraints presented in §5.5. Since the constraints are linear, quadratic, or second order cone constraints, the resulting problem is a convex programming problem, which can be efficiently solved by readily available algorithms [113].

Differential equations written with unit dual quaternions can be discretized as follows:

$$-\Delta t\, \tilde{\mathbf{F}}(t) + \boldsymbol{J}\tilde{\boldsymbol{\omega}}(t+1) = \boldsymbol{J}\tilde{\boldsymbol{\omega}}(t) - \Delta t\, [\tilde{\boldsymbol{\omega}}(t)]_{\times}(\boldsymbol{J}\tilde{\boldsymbol{\omega}}(t)) + \Delta t\, \tilde{\mathbf{g}}(t) \tag{5.53d}$$

$$-\frac{\Delta t}{2}\tilde{\mathbf{q}}(t+1) \otimes \tilde{\boldsymbol{\omega}}(t+1) + \tilde{\mathbf{q}}(t+2) = \tilde{\mathbf{q}}(t+1). \tag{5.40d}$$

Note that we have assumed that the time sequence of the differential equations is

$$\tilde{\mathbf{F}}(t) \implies \tilde{\boldsymbol{\omega}}(t+1) \implies \dot{\tilde{\mathbf{q}}}(t+2). \tag{5.129}$$

By defining a new state variable $x(t)$ as

$$x(t) = \begin{bmatrix} \tilde{\mathbf{F}}(t) \\ \tilde{\boldsymbol{\omega}}(t+1) \\ \tilde{\mathbf{q}}(t+2) \end{bmatrix}_{24\times 1}, \tag{5.130}$$

the convex optimization approach to the constrained minimum pinpoint landing error problem assumes the following form:

Problem 1a:

$$\min_{x(t)} \begin{bmatrix} x(t) \\ 1 \end{bmatrix}^T W \begin{bmatrix} x(t) \\ 1 \end{bmatrix} \tag{5.131}$$

subject to:

$$A(t)x(t) = b(t) \tag{5.132}$$

$$x(t)^T H_1 x(t) + \|Dx(t)\| \le 0 \tag{5.79'}$$

$$x(t)^T H_2 x(t) + \|Dx(t)\| \le 0 \tag{5.92'}$$

$$x(t)^T H_3 x(t) \le 0 \tag{5.102'}$$

$$H_4 x(t) + \cos\eta \|D_F x(t)\| \le 0 \tag{5.133}$$

$$x(t)^T H_5 x(t) - \zeta_{\tilde{\mathbf{q}}} \le 0 \tag{5.123'}$$

$$-\zeta \le Gx(t) \le \zeta \tag{5.124ab}$$

$$x(0) = x_0, \quad x(N) = x_N \tag{5.134}$$

where

$$W = \begin{bmatrix} 0_{8\times 8} & 0_{8\times 8} & 0_{8\times 8} & 0_{8\times 1} \\ 0_{8\times 8} & \mathbf{I}_{8\times 8} & 0_{8\times 8} & -\tilde{\boldsymbol{\omega}}(N) \\ 0_{8\times 8} & 0_{8\times 8} & \mathbf{I}_{8\times 8} & -\tilde{\mathbf{q}}(N) \\ 0_{1\times 8} & -\tilde{\boldsymbol{\omega}}(N)^T & -\tilde{\mathbf{q}}(N)^T & \tilde{\boldsymbol{\omega}}(N)^T\tilde{\boldsymbol{\omega}}(N) + \tilde{\mathbf{q}}(N)^T\tilde{\mathbf{q}}(N) \end{bmatrix}_{25\times 25} \in \mathbb{S}_+^{25}, \tag{5.135}$$

$$A(t) = \begin{bmatrix} -\Delta t\, \mathbf{I}_8 & \boldsymbol{J} & 0_{8\times 8} \\ 0_{8\times 8} & -\frac{\Delta t}{2}[\tilde{\mathbf{q}}(t+1)]_{\otimes} & \mathbf{I}_8 \end{bmatrix}_{16\times 24}, H_1 = \begin{bmatrix} 0_{16\times 16} & 0_{16\times 8} \\ 0_{8\times 16} & M_H \end{bmatrix}_{24\times 24} \tag{5.136}$$

$$b(t) = \begin{bmatrix} \boldsymbol{J}\tilde{\boldsymbol{\omega}}(t) - \Delta t\,[\tilde{\boldsymbol{\omega}}(t)]_\times\,(\boldsymbol{J}\tilde{\boldsymbol{\omega}}(t)) + \Delta t\,\tilde{\mathbf{g}}(t) \\ \tilde{\mathbf{q}}(t+1) \end{bmatrix}_{16\times 1}, H_4 = \begin{bmatrix} \mathbf{1}_{3\times 1} \\ 0_{21\times 1} \end{bmatrix}_{24\times 1} \tag{5.137}$$

$$H_2 = \begin{bmatrix} 0_{16\times 16} & 0_{16\times 8} \\ 0_{8\times 16} & -M_G \end{bmatrix}_{24\times 24}, \qquad H_3 = \begin{bmatrix} 0_{16\times 16} & 0_{16\times 8} \\ 0_{8\times 16} & M_A \end{bmatrix}_{24\times 24} \tag{5.138}$$

$$H_5 = \begin{bmatrix} 0_{16\times 16} & 0_{16\times 8} \\ 0_{8\times 16} & \mathbf{I}_8 \end{bmatrix}_{24\times 24}, \qquad D_F = \begin{bmatrix} \mathbf{I}_3 & 0_{3\times 21} \\ 0_{21\times 3} & 0_{21\times 21} \end{bmatrix}_{24\times 24} \tag{5.139}$$

$$G = \begin{bmatrix} \mathbf{I}_{16} & 0_{16\times 8} \\ 0_{8\times 16} & 0_{8\times 8} \end{bmatrix}_{24\times 24}, \quad \zeta = \begin{bmatrix} \zeta_{\tilde{\mathbf{F}}} \\ \zeta_{\tilde{\boldsymbol{\omega}}} \end{bmatrix}_{16\times 1}, \quad D = \begin{bmatrix} 0_{16\times 16} & 0_{16\times 8} \\ 0_{8\times 16} & 2E_d \end{bmatrix}_{24\times 24}. \tag{5.140}$$

As noted in [114], the unit quaternion part of unit dual quaternion grows in every iteration from the unit quaternion kinematic equations as

$$\mathbf{q}(t+1) = \mathbf{q}(t) + \frac{\Delta t}{2}\mathbf{q} \otimes \boldsymbol{\omega} \tag{5.141}$$

and, thereby

$$\|\mathbf{q}(t+1)\|^2 = \mathbf{q}(t)^T\mathbf{q}(t) + \frac{\Delta t^2}{4}(\mathbf{q}\otimes\boldsymbol{\omega})^T(\mathbf{q}\otimes\boldsymbol{\omega}) + \Delta t\,\mathbf{q}(t)^T(\mathbf{q}\otimes\boldsymbol{\omega}) \tag{5.142}$$

$$= 1 + \frac{\Delta t^2}{4}\|\boldsymbol{\omega}\|^2 + \Delta t\boldsymbol{\omega}^T(\mathbf{q}^*\otimes\mathbf{q}) \tag{5.143}$$

$$= 1 + \frac{\Delta t^2}{4}\|\boldsymbol{\omega}\|^2 \tag{5.144}$$

$$= 1 + \Delta\mathbf{q}(t+1) \geq 1. \tag{5.145}$$

Thus, as long as the initial unit quaternion is valid, we have from every iteration:

$$\|\mathbf{q}(t)\| \geq 1, \quad \forall t \geq 1. \tag{5.146}$$

The proposed convex constraints, Eqs. (5.40), (5.79), (5.92), (5.102), and (5.121) ensure rotationally and translationally constrained zones as long as the unit dual quaternions are valid. As we just observed, the error in the unit quaternion part grows over iterations due to

linearization, which is exacerbated in unit dual quaternions because the second quaternion part in a unit dual quaternion is given as a multiplication between the quaternion possessing error and translational displacement which is relatively large to the magnitude of unit quaternions as

$$\|\tilde{\mathbf{q}}(t+1)\|^2 = \|\mathbf{q}(t+1)\|^2 + \left\|\frac{1}{2}\boldsymbol{t}_o \otimes \mathbf{q}\right\|^2 \tag{5.147}$$

$$\simeq 1 + \Delta\mathbf{q}(t+1) + \left\|\frac{1}{2}\boldsymbol{t}_o(t+1) \otimes [\mathbf{q}(t+1) + \Delta\mathbf{q}(t+1)]\right\|^2 \tag{5.148}$$

$$\simeq 1 + \left\|\frac{1}{2}\boldsymbol{t}_o(t+1) \otimes \mathbf{q}(t+1)\right\|^2 + \Delta\mathbf{q}(t+1) + \left\|\frac{1}{2}\boldsymbol{t}_o(t+1) \otimes \Delta\mathbf{q}(t+1)\right\|^2. \tag{5.149}$$

We resolve the first issue by projecting every calculated unit quaternion $\hat{\mathbf{q}}(t+1) \in \mathbb{R}^4 \mapsto \mathbf{q} \in \mathcal{S}^3$ by utilizing the definition of the unit quaternion

$$\mathbf{q} \stackrel{\text{def}}{=} \frac{\hat{\mathbf{q}}}{\|\hat{\mathbf{q}}\|}, \tag{5.150}$$

where $\hat{\mathbf{q}} \in \mathbb{R}^4$. This updated unit quaternion forms updated dual unit quaternion to be used as an initial condition for next iteration. For the second part in the unit dual quaternion, there are still significant amount of drifting errors induced because the unit of the distance is much larger than unit quaternion and they are multiplied in the error term. For the simple treatment, we scale down the translational displacement to minimize such a drift error term.

5.7 Numerical Simulations

This section presents a numerical example to demonstrate the algorithm proposed in the previous section that solves the Mars pinpoint landing problem in the presence of constraints. In the example, it has been assumed that the Mars lander is required not to violate the four types of rotationally and translationally constrained zones. The simulation is carried out by using Matlab generic nonlinear solver with an interior point algorithm. Even though it was not processed by the solver customized for this algorithm, the anticipatable execution times and assurance for convergence makes this algorithm a good candidate for onboard

guidance algorithm. The spacecraft's physical properties are given as

$$\text{Moment of inertia: } J = \texttt{diag}[\,95.33, \quad 77.98, \quad 67.14\,]\, kg \cdot m^2, \tag{5.151}$$

$$\text{Mass: } m = 162.07kg, \tag{5.152}$$

$$\text{Gravity on Mars: } g_o = [\,0, \quad 0, \quad -3.7114\,]\, m/s^2. \tag{5.153}$$

The Mars lander configuration with the human window view vector is depicted in Fig. (5.10). The initial and final conditions including attitudes, positions, and velocities are given in Table 5.2. Detailed parameters for four rotation and translation related constraint are also presented. State bounds are reasonably defined and addressed in the Table 5.3. Based on initial and desired attitudes as well as their positions, corresponding initial and desired conditions in unit dual quaternions are calculated by

$$\begin{aligned} \tilde{\mathbf{q}}(0) &= \begin{bmatrix} \mathbf{q}(0) \\ \frac{1}{2}\boldsymbol{t}_o(0) \otimes \mathbf{q}(0) \end{bmatrix} \\ &= [-0.38,\, 0.49,\, -0.40,\, 0.67,\, 216.79,\, -70.70,\, 229.34,\, 312.89]^T \end{aligned} \tag{5.154}$$

$$\tilde{\mathbf{q}}(t_f) = [0,\, 0,\, 0,\, 1.00,\, 0,\, 0,\, 0.50,\, 0]^T, \tag{5.155}$$

where both initial and desired attitude $\mathbf{q}(0), \mathbf{q}(t_f)$ and positions $\boldsymbol{t}_o(0), \boldsymbol{t}_o(t_f)$ are randomly chosen from a set of corresponding dual quaternions that are satisfying all convex constraints as

$$f_i(\tilde{\mathbf{q}}(0)) \leq 0 \quad \text{and} \quad f_i(\tilde{\mathbf{q}}(t_f)) \leq 0, \quad \text{for } i = 1, .., 4. \tag{5.156}$$

In Fig. (5.11), overall trajectory of the Mars lander is depicted along with the representation of human window view angle cone. The desired position for landing is denoted by a blue circle in the figure. We note that different from the point mass model, the shape of overall trajectory is affected by the initial and desired attitudes. This is due to the fact that the rotational and translational motions are combined with dual quaternions and the shortest path between two points on unit dual quaternion manifold is exhibited as a screw motions in $\mathsf{SE}(3)$. By weighting the second part of dual quaternion which is related to positions, we can easily modify the convergence rate between rotational and translational

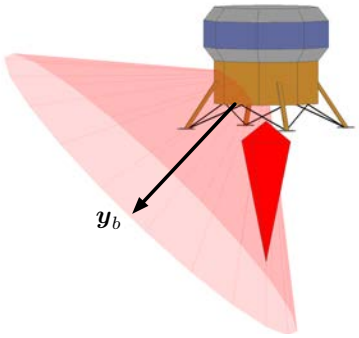

Figure 5.10: Mars lander configuration with the human window view vector $\boldsymbol{y}_b$

motions. Fig. (5.12) show the time histories for the position and attitude in unit quaternions of Mars lander which is observed with respect to an inertially fixed frame while Fig. (5.13) depicts the time histories for translational and angular velocities in the body-fixed frame. Note that the translational velocities for the first 100 seconds have been restricted by their upper and lower bounds given in Table 5.3. The translational forces and torques acting along the body-fixed axes are represented in Fig. (5.14). Note that the translational forces never vanish since there exists a gravitational force acting downwards and forces acting along $\boldsymbol{z}_b$ compensate such a gravitational force to maintain the desired altitude in the later part of simulation.

Fig. (5.15) shows the trace of the deviating angle over time from human window view vector $\boldsymbol{y}_b$ to the desired landing spot. As we can expect from Mars lander configuration in Fig. 5.10, pure vertical descent arises around the boundary of the human window view constraint cone. Glide slope angle constraint is defined by 65° and Fig. 5.16 represents the glide slop angle and the trajectory of position over time. Fig. 5.17 represents the time histories of the general attitude angle and net thrust direction angle. The initial general attitude angle from a randomly generated initial attitude results in net thrust direction that hits the limit in order to generate a maximum force for the vertical maneuver.

Δt	0.2 seconds
No. of iterations	2000
t_f	400 seconds
Initial Attitude $\mathbf{q}(0)$	[-0.3841, 0.4913, -0.4009, 0.6710]
Initial Position $\boldsymbol{t}_o(0)$	[700, -400, 400] m
Initial Velocity $\boldsymbol{v}_b(0)$	[1, 3, 0] m/s
Initial Angular Velocity $\boldsymbol{\omega}_b(0)$	[0, 0, 0] rad/s
Desired Attitude $\mathbf{q}(t_f)$	[0, 0, 0, 1]
Desired position $\mathbf{q}(t_f)$	[0, 0, 0]
Desired Velocity $\boldsymbol{v}_b(t_f)$	[0, 0, 0] m/s
Desired Angular Velocity $\boldsymbol{\omega}_b(t_f)$	[0, 0, 0] rad/s
Human window view	$\boldsymbol{y}_b$ = [0, $\sqrt{2}/2$, -$\sqrt{2}/2$], $\theta = 40^\circ$
Glide slope	$\boldsymbol{z}_o$ = [0, 0, 1], $\phi = 65^\circ$
General spacecraft attitude	$\boldsymbol{z}_o$ = [0, 0, -1], $\boldsymbol{z}_b$ = [0, 0, -1], $\psi = 75^\circ$
Net thrust direction	$\boldsymbol{z}_b$, $\eta = 90^\circ$

Table 5.2: Constrained pin-point landing simulation parameters

$\|\boldsymbol{t}_b\|$	$\leq 900\ m$
$\|F_x\|, \|F_y\|, \|F_z\|$	$\leq 700\ N$
$\|M_x\|, \|M_y\|, \|M_z\|$	$\leq 5\ N \cdot m$
$\|v_x\|, \|v_y\|, \|v_z\|$	$\leq 7\ m/s$
$\|\omega_x\|, \|\omega_y\|, \|\omega_z\|$	$\leq 0.03\ rad/s$

Table 5.3: Pin-point landing simulation state bounds

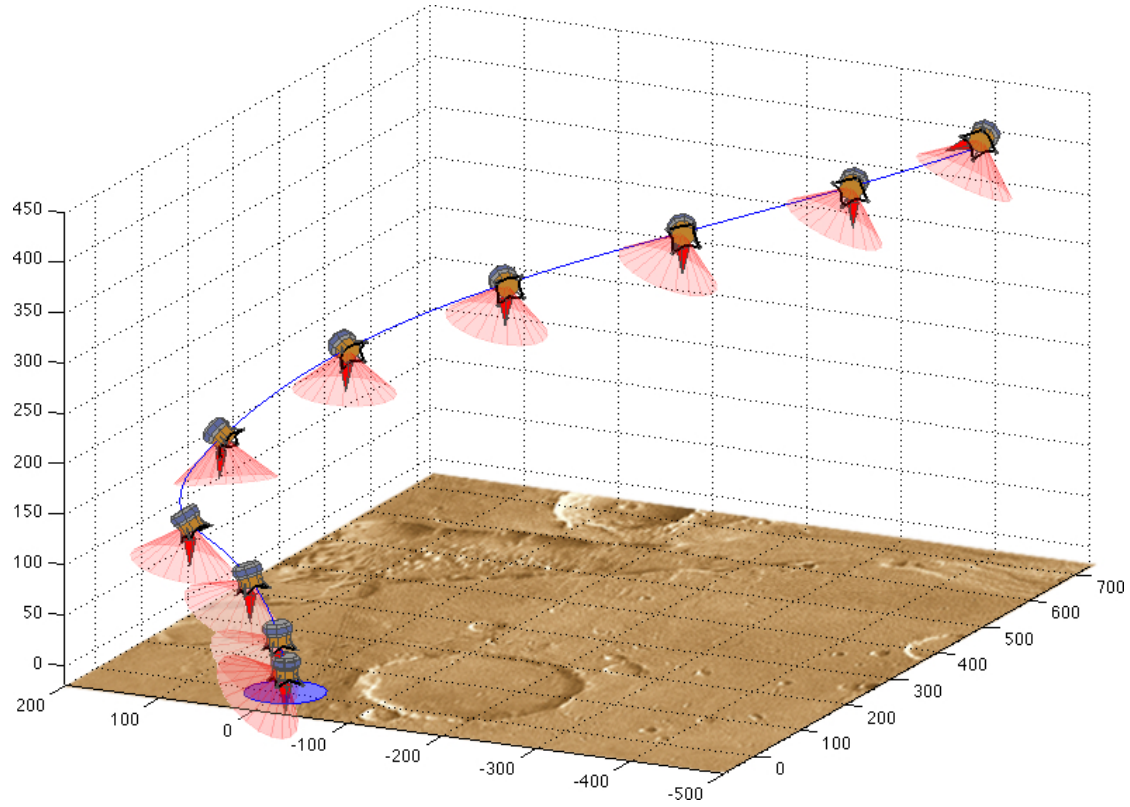

Figure 5.11: Overall trajectory of Mars lander's powered descent for pin-point landing along with the representation of human window view angle cone.

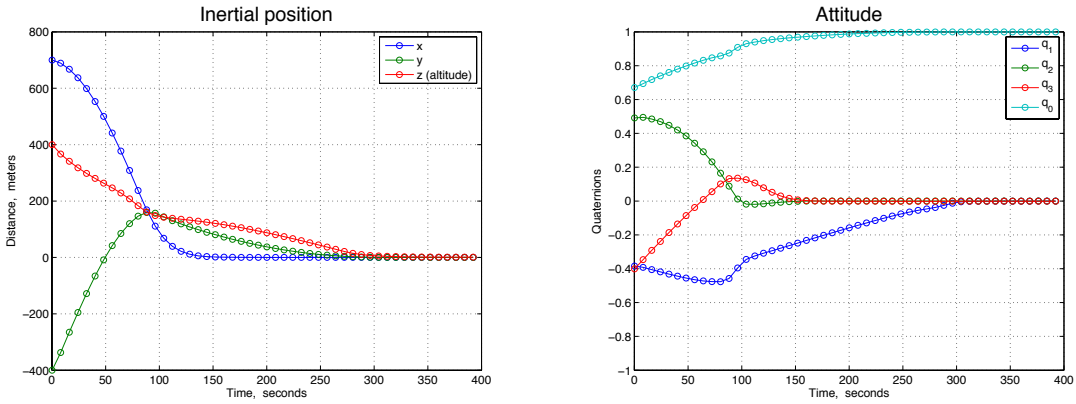

Figure 5.12: Time histories for the position and attitude of Mars lander observed in an inertially fixed frame.

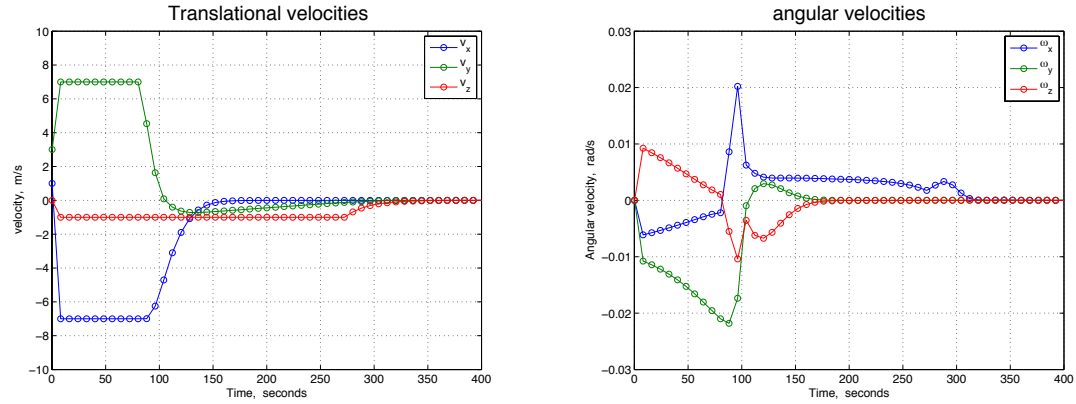

Figure 5.13: Time histories for the translational and angular velocities in the body-fixed frame.

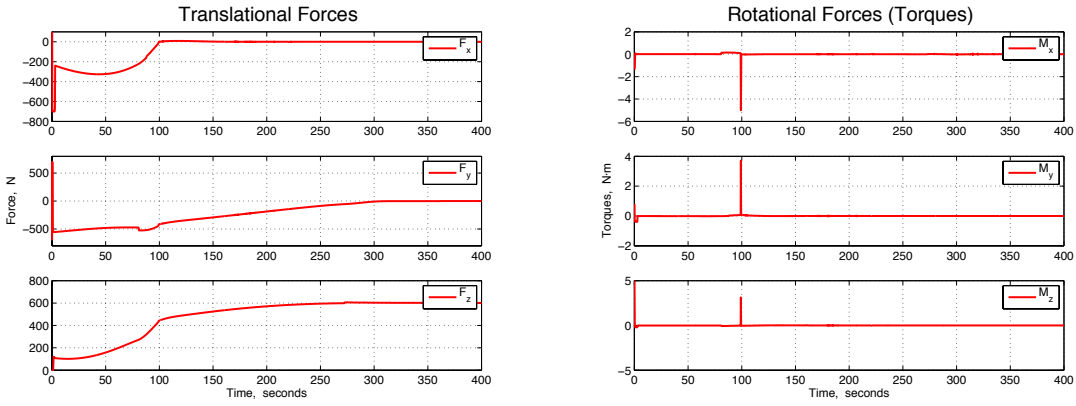

Figure 5.14: Time histories for the translational forces and torques expressed in the body-fixed frame.

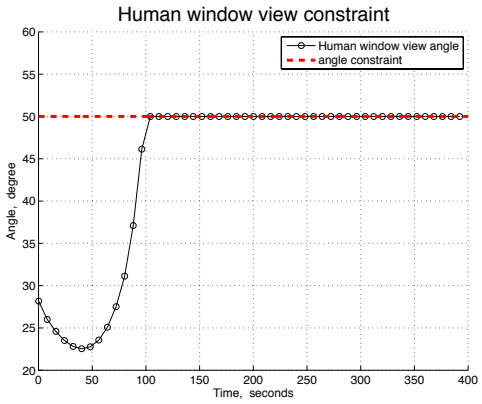

Figure 5.15: Trace of deviating angle over time from human window view vector $\boldsymbol{y}_b$ to the desired landing spot.

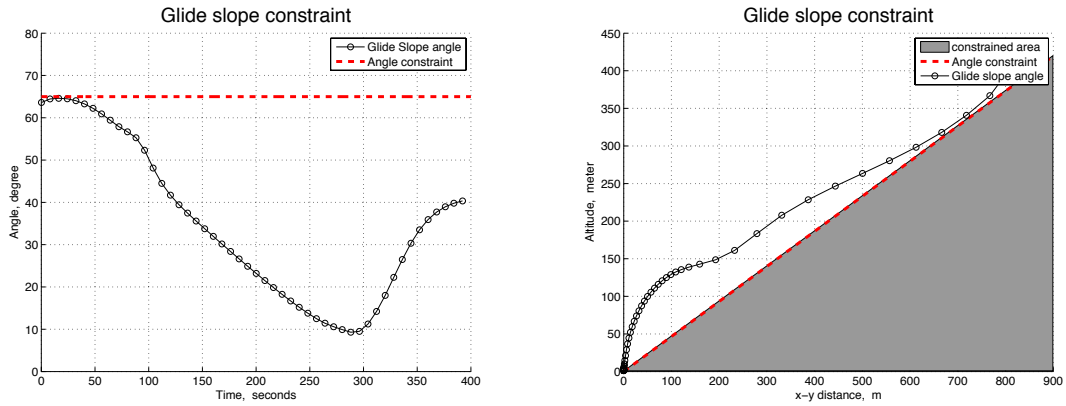

Figure 5.16: Glide slop angle over time on the left and the trajectory of Mars lander position over time on the right

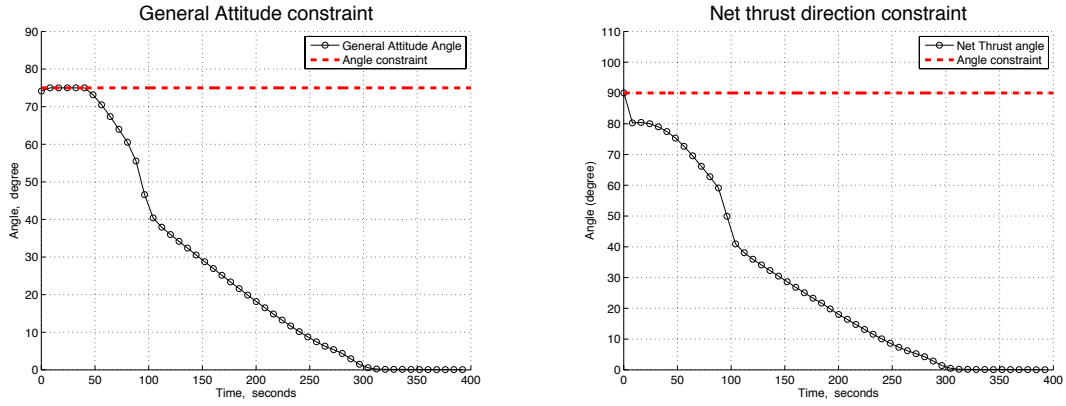

Figure 5.17: Time histories of the general attitude angle and net thrust direction angle.

5.8 Concluding Remarks

In this chapter, we first provided a general framework for the analysis of unit dual quaternion-based rigid body control and presented a number of almost globally stable tracking control laws. Inspired by the fact that unit dual quaternion can efficiently parameterize the rotational and translational motions, we developed the convex representable subset of dual unit quaternions corresponding to rotationally and translationally constrained zones in the context of a powered descent guidance algorithm since a lander is the most typical rigid body experiencing rotational and translational motion constraints. Then, we constructed a quadratically constrained quadratic program for power-descent guidance algorithm for a Mars lander. The convex programming approach was shown to provide a unifying framework through which various classes of unit dual quaternion-based constraints can be solved in polynomial time through the elegant interior-point algorithm.

Chapter 6

CONCLUSIONS AND FUTURE RESEARCH

In this dissertation we presented a number of control algorithms for monolithic and distributed space systems in the presence of rotationally and translationally constrained zones. In the first part of dissertation, consisting of Chapters 2 and 3, we addressed the advantages of adapting the unit quaternion representation over other parameterizations in modeling spacecraft rotational dynamics. Moreover, we addressed some of important issues related to unit quaternion representations such as "almost global stability" properties and the "unwinding phenomenon" and a simple solution for the latter phenomenon has been suggested. We then formulated a convex optimization framework for attitude reorientation planning in the presence of rotationally constrained zones. Taking advantage of a novel strictly convex logarithmic barrier potential, we proposed two classes of control laws and showed that both approaches are valuable not only in their flexibility in handling extremely complex maneuver planning problems but also in terms assuming a feedback control form. Additionally, we investigated a quaternion based time/energy-optimal spacecraft reorientation problem via a judiciously formulated nonlinear optimal control problem, and subsequently solved using a Gauss pseudospectral method. In Chapter 4, we treated the problem of achieving identical orientation for a distributed spacecraft system in the presence of rotationally constrained zones. In order to develop such an algorithm, we first presented a distributed algorithm for consensus of multiple robotic agents where the shared state was assumed to be constrained in a compact convex set. We then proposed a distributed algorithm for the agents to reach agreement on a state that lies at the intersection of the individual convex constraint sets.

The spacecraft attitude synchronization problem in the presence of rotationally constrained zones is then formulated based on the proposed distributed protocol. In order to evaluate the effectiveness of the algorithm, we also presented two sets of simulations where synchronization of six spacecraft with identical and independent rotationally constrained zones with random initial attitude were considered.

In Chapter 5, as an extension to the first part of the dissertation, we presented the general framework for the analysis of rotationally and translationally constrained spacecraft control problems. We derived the general dynamics of a rigid body describing a translation and a rotation in terms of *unit dual quaternions*. Analogous to the unit quaternion based algorithm, we developed an almost globally stable control algorithm for unconstrained rigid-body dynamics via a convex energy like Lyapunov function on unit dual quaternions. We then proceeded to characterize the convex representable subsets of unit dual quaternions that correspond to several types of translationally and rotationally constrained zones. To evaluate the effectiveness of proposed formulation, we developed a semi-definite programming approach to control synthesis of a Mars lander that has the aforementioned constrained zones embedded in its mission specifications. The chapter concluded with a set of numerical simulations demonstrating the efficacy of the proposed approach to rotationally and translationally constrained space systems.

6.1 Future Research

In Chapter 5, we analyzed the rotationally and translationally constrained motion planning problem. This type of problem has a number of potential applications since they arise in wide array of fields. For example, rendezvous with tumbling objects in the Earth circular orbit requires a prudent approach following a spinning axis to avoid a collision because such tumbling objects are characterized by unpowered satellites required for on-orbit servicing or space debris from the launch vehicle. Thus the object's rotational motion not only restricts the approach direction toward the object but also compels the approaching spacecraft's sensors to lock on the objects en-route. This constitutes a challenging rotationally and translationally coupled constrained motion. In this direction, taking advantage of the unit dual quaternion parameterization that can capture this combined spacecraft motions

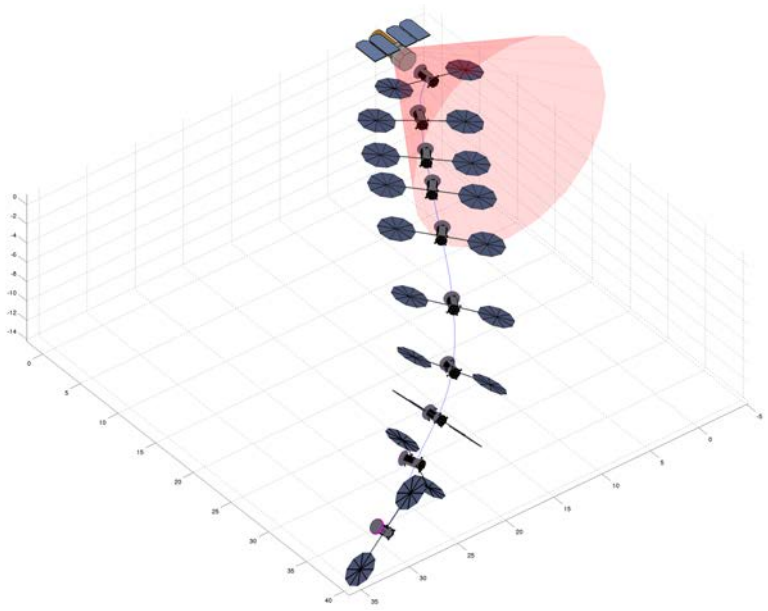

Figure 6.1: Position and orientation time history of a solar electric propulsion spacecraft during rendezvous with an uncooperative object.

simultaneously, we can compactly represent the relative motion dynamics in Earth circular orbit as well as the spacecraft rotational dynamics. Based on a convex representable subset to represent all feasible translational and rotational motions proposed in Chapter 5, semi-definite programming can then be used to find the control algorithms for the approaching spacecraft over this required convex subset. In Fig. 6.1, position and orientation time history of the approaching spacecraft obtained from a preliminary simulation result is presented.

Appendix A

STABILITY THEORY

A.1 Lyapunov Stability

Consider the nonlinear time invariant system:

$$\dot{x} = f(x) \quad \text{and} \quad x(0) = x_0, \tag{A.1}$$

where $x \in \mathbb{R}^n$ and $f : \mathbb{R}^n \to \mathbb{R}^n$ is assumed to *locally Lipschitz* in x. Suppose $f(x)$ has an equilibrium at x_d so that

$$f(x_d) = 0. \tag{A.2}$$

Then,

1. the equilibrium of the system $f(x)$ is *Lyapunov stable* if, for each $\epsilon > 0$, there exists a $\delta(\epsilon) > 0$ such that

$$\|x(0) - x(x_d)\| < \delta(\epsilon) \Rightarrow \|x(t) - x_d\| < \epsilon, \quad \forall t \geq 0. \tag{A.3}$$

2. the equilibrium is *locally asymptotically stable*, if it is Lyapunov stable and if there exists $\delta > 0$ such that

$$\|x(0) - x(x_d)\| < \delta(\epsilon) \Rightarrow \lim_{t\to\infty} \|x(t) - x_d\| = 0. \tag{A.4}$$

3. the equilibrium is *locally exponentially stable*, if there are positive constant α, β, and δ such that

$$\|x(0) - x(x_d)\| < \delta \Rightarrow \|x(t) - x_d\| < \alpha\|x(0) - x(x_d)\|e^{-\beta t}, \quad \forall t \geq 0 \tag{A.5}$$

4. the equilibrium is *globally asymptotically stable*, if it is locally asymptotically stable and if for every trajectory $x(t) \in \mathbb{R}^n$ we have

$$\lim_{t\to\infty} \|x(t) - x_d\| = 0 \tag{A.6}$$

A.2 Lyapunov's Direct Method

Theorem A.1 (Lyapunov's Direct Method)**.** *Let x_d be the equilibrium point of the system $f(x)$ and assume that $f(x)$ is locally Lipschitz in x. Let $V : \mathbb{R}^n \to \mathbb{R}_+$ be a continuously differentiable function $V(t)$ satisfying:*

- $V(x) > 0, \quad \forall x \in \mathbb{R}^n \setminus \{0\}$,
- $\dot{V}(x) = \frac{\partial V(x)}{\partial x} f(x) \leq -G(x) \leq 0$,

Then the equilibrium point x_d is locally stable if $G(x) \geq 0$, or locally asymptotically stable if $G(x) > 0$, $\forall x, x \neq x_d$. In addition, if we have

- $V(x) \to \infty$ *as* $\|x\| \to \infty$ *(radially unbounded),*

the equilibrium point x_d is globally stable if $G(x) \geq 0$, or globally asymptotically stable if $G(x) > 0$, $\forall x, x \neq x_d$.

Proof. See Khalil [49]. □

A.3 Krasvskii-LaSalle's Theorem

The theorem of Krasovskii-Lasalle can be used to check a nonlinear autonomous sytem for globally asymptotical stability.

Theorem A.2. *Let $V : R^n \to R_+$ be a continuously differentiable positive definite function such that*

$$V(x) \to \infty \text{ as } \|x\| \to \infty \text{ and } \dot{V}(x) \leq 0, \quad \forall x, \tag{A.7}$$

and let $\mathcal{D}$ be the set of all point where $\dot{V}(x) = 0$, that is

$$\mathcal{D} = \{x \in \mathbb{R}^n | \dot{V}(x) = 0\}, \tag{A.8}$$

and $\mathcal{M}$ be the largest invariant set in $\mathcal{D}$. Then all solutions $x(t)$ converge to $\mathcal{D}$. If $\mathcal{M} = \{x_d\}$, the equilibrium point x_d of $f(x)$ is globally asymptotically stable.

Proof. See Khalil [49]. □

Appendix B

BACK-STEPPING CONTROL

Consider the following cascaded system:

$$\dot{x} = f(x) + g(x)y \tag{B.1}$$

$$\dot{y} = f'(x,y) + g'(x,y)u, \tag{B.2}$$

where $x \in \mathbb{R}^n, y \in \mathbb{R}^m, u \in \mathbb{R}^m, f(0) = 0$ and $f'(0,0) = 0$. The functions $f(x)$ and $f'(x,y)$ are continuous and g' is assumed to be invertible. The subsystem described by Eq. (B.1) is stabilized first using the control law $y = -f(x)$ and then the resulting control u is developed so that the overall system described by Eqs. (B.1-B.2) is stabilized. The backstepping control design scheme can be briefly described by the following two theorems.

Theorem B.1. *Using a candidate Lyapunov function $V(x)$, the subsystem described by Eq. (B.1) can be stabilized by the control law $y = -f(x)$ which satisfies the following condition*

$$\frac{\partial V}{\partial x}\left(f(x) - g(x)f(x)\right) \leq -W(x) \tag{B.3}$$

where $W(x)$ denotes a positive definite function.

Proof. See Khalil [49]. □

Theorem B.2. *Assume that Eq. (B.3) is satisfied, the overall system described by Eqs. (B.1)-(B.2) is stabilized by the control input given by*

$$u = g'^{-1}\left(-\frac{\partial f}{\partial x}(f + gy) - \left(\frac{\partial V}{\partial y}g\right)^T - f' - k(y + f)\right), \tag{B.4}$$

with the augmented Lyapunov function

$$V'(x,y) = V(x) + \frac{1}{2}(y+f)^T(y+f) \tag{B.5}$$

and its time derivative as

$$\dot{V}' = \frac{\partial V}{\partial x}(f - gf) + \frac{\partial V}{\partial x}g(y+f) + (y+f)^T(f' + g'u + \frac{\partial f}{\partial x}(f+gy)), \tag{B.6}$$

where k denotes a positive constant.

Proof. See Khalil [49]. □

BIBLIOGRAPHY

[1] C. G. Mayhew, R. G. Sanfelice, and A. R. Teel, "Quaternion-based bybrid control for robust global attitude tracking," *IEEE Transactions on Automatic Control,* col. 56, no. 11, pp. 2555-2566, Nov. 2011.

[2] C. G. Mayhew, R. G. Sanfelice, and A. R. Teel, "On Quaternion-based Attitude Control and the Unwinding Phenomenon," *Proceedings of the American Control Conference,* 2011, pp. 299-304, 2011.

[3] B. Wie, H. Weiss, and A. Arapostathis, "Quaternion Feedback Regulator for Spacecraft Eigenaxis Rotations, *Journal of Guidance, Control, and Dynamics,* vol. 12, no. 3, pp. 375-380.

[4] D. Seo and M. R. Akella, "Seperation Property for the Rigid-body Attitude Tracking Control Problem," *Journal of Guidance, Control, and Dynamics,* vol. 30, no. 6, pp. 1569-1576, 2007.

[5] D. Angeli, "A Global Notion of Input-to-State Stability," *IEEE Transactions on Automatic Control,* vol. 49, no. 6, pp. 866-874, 2004.

[6] B. Wie and P. M. Barba, "Quaternion Feedback for Spacecraft Large Angle Maneuvers," *Journal of Guidance, Control and Dynamics*, Vol. 8, No. 3, pp. 360-365, 1985.

[7] S. Bhat and D. S. Bernstein, "A Topological Obstruction to Continuous Global Stabilization of Rotational Motion and the Unwinding phenomenon," *Systems & Control Letters*, vol. 39, no. 1, 63-70, 2000.

[8] J. R. Lawton and R. W. Beard, "Synchronized Multiple spacecraft rotations, *Automatica,* vol. 38, no. 8, pp. 1359-1364, Aug. 2002.

[9] J. T. Betts, "Survey of Numerical Methods for Trajectory optimization," *Journal of Guidance, Control, and Dynamics,* vol. 21, no. 2, pp. 193-207, 1998.

[10] B. Acikmese and S. R. Ploen, "Convex Programming Approach to Powered Descent Guidance for Mars Landing," *Journal of Guidance, Control, and Dynamics,* vol. 30, No. 5, 2007.

[11] B. Acikmese, L. Blackmore, D. P. Scharf, and A. Wolf, "Enhancements on the Convex Programming Based Powered Descent Guidance ALgorithm for Mars Landing," *AIAA/AAS Astrodynamics Specialist Conference and Exhibit,* AIAA 2008-6426, 2008.

[12] P. Cui, W. Zhong, and H. Cui, "Onboard Spacecraft Slew-planning by Heuristic State-space Search and Optimization," *International Conference on Mechatronics and Automation*, pp. 2115-2119, 2007.

[13] Y. D. Song and W. C. Cai, "New Intermediate Quaternion based Control of Spacecraft: Part I - Almost Global Attitude Tracking," *International Journal of Innovative Computing, Information and Control,* vol. 8, no. 10(B), 2012.

[14] A. Sanyal and N. Chaturvedi, "Almost Global Robust Attitude Tracking Control of Spacecraft in Gravity," *Proceedings of the AIAA Conference on Guidance, Navigation and Control*, 2008.

[15] R. Ball, "The Theory of Screws: A Study in the Dynamics of a Rigid Body," *Mathematische Annalen*, vol. 9, no. 4, pp. 0025-5831, 1876.

[16] J. Diebel, "Representing Attitude: Euler Angles, Unit Quaternions, and Rotation Vectors," Stanford University, Stanford, CA, Technical Report, 2006.

[17] S.R. Stadin and R.W. Davis, "The Small Satellite Revolution-Back to the Future," IAF-93-U, 1993.

[18] N. Moshtagh, A. Jadbabaie, and K. Danilidis, "Distributed geodesic control laws for flocking of nonholonomic agents,*Proceedings of 44th IEEE Conference on Decision and Control,* pp. 2835-2841, Dec. 2005.

[19] J. Vlassenbroeck and R. V. Dooren, "A Chebyshev Technique for Solving Nonlinear Optimal Control Problem," *IEEE Transactions on Automatic Control,* vol. 33, no. 4, pp. 333-340, 1988.

[20] N. Deo, "Graph Theory with Applications to Engineering and Computer Science," PHI, New Delhi, 1974.

[21] M. Mesbahi and M. Egerstedt, *Graph Theoretic Methods in Multiagent Networks*, Princeton University Press, 2010.

[22] H. L. Pham, V. Perdereau, B. V. Adorno, and P. Fraisse, "Position and Orientation Control of Robot Manipulators using Dual Quaternion Feedback," *in The 2010 IEEE/RSJ International Conference on Intelligent Robots and Systems,* Taiwan, October, 2010.

[23] S. D, Gennaro, "Output Stabilization of Flexible Spacecraft with Active Vibration Suppression," *IEEE Transactions on Aerospace and Electronic Systems,* vol.39, no.3, pp.747,759, 2003.

[24] Y. Xiao, Y. Censor, D. Michalski, J. Galvin, "The Least-Intensity Feasible Solution for Aperture-Based Inverse Planning in Radiation Therapy," *Annals of Operations Research*, vol. 119, no. 1-4, 183-203, 2003.

[25] H. B. Hablani, "Attitude Commands Avoiding Bright Objects and Maintaining Communication with Ground Station," *Journal of Guidance, Control, and Dynamics*, vol. 22, no. 6, pp. 759-767, 1999.

[26] Y. Kim, M. Mesbahi, G. Singh, and F. Hadaegh, "On the Convex Parametrization of Spacecraft Orientation in the presence of Constraints and its Applications," *IEEE Transactions on Aerospace and Electronic Systems*, vol. 46, no. 3, pp. 1097-1109, 2010.

[27] G. Ma, Y. Zhuang, C. Li, and H. Huang, "Pseudospectral Method for Optimal Motion Planning of a Rigid Under-actuated Spacecraft," *2010 8th IEEE International Conference on Control and Automation*, Xianmen, China, 2010.

[28] D. Hoag, "Apollo Guidance and Navigation Considerations of Apollo IMU Gimbal Lock," *MIT Instrumentation Laboratory Document E-1344,* April, 1963.

[29] W. R. Hamilton, "On quaternions, or on a New System of Imaginaries in Algebra," *Philosophical Magazine,* vol. 25, no. 3, pp. 489-495, 1844.

[30] W. R. Hamilton, "Lectures on Quaternions", *Royal Irish Academy,* 1853.

[31] A. V. Rao, D. A. Benson, C. Darby, M. A. Patterson, C. Francolin, I. Sanders, and G. T. Huntington, "Algorithm 902: GPOPS, A MATLAB software for solving multiple-phase optimal control problems using the gauss pseudospectral method," *ACM Transaction on Mathematical Software,* vol 37, no. 2, Article 22, 2010.

[32] D. Garg, M. A. Patterson, W. W. Hager, A. V. Rao, D. A. Benson and G. T. Huntington, "A Unified Framework for the Numerical Solution of Optimal Control Problems Using Pseudospectral Methods," *Automatica,* vol. 46, No. 11, 2010, pp. 1943-1851.

[33] D. Garg, M. A. Patterson, W. W. Hager, A. V. Rao, D. A. Benson and G. T. Huntington, "An Overview of Three Pseudospectral Method for the Numerical Solution of Optimal Control Problems," *Advances in the Astronautical Sciences,* Univelt Inc., San Diego, 2010, pp. 475-487.

[34] M. Egerstedt and X. Hu, "Formation Control with Virtual Leaders and Reduced Communications," *IEEE Transaction on Robotics and Automation,* vol. 17, no. 6, pp. 947-951, 2001.

[35] D. G. Hull, "Conversion of Optimal Control Problem into Parameter Optimization Problems," *Journal of Guidance, Control, and Dynamics,* vol. 20, no. 1, pp. 57-60, 1997.

[36] I. Ali, "Spacecraft Nonlinear Attitude Control with Bounded Control Input," Ph.D dissertation, University of Glasgow, 2009.

[37] P. Singla, K. Subbarao, and J. Junkins, "Adaptive Output Feedback Control for Spacecraft Rendezvous and Docking under Measurement Uncertainty," *Journal of Guidance, Control and Dynamics,* vol. 29, no. 4, pp. 892-902, 2006.

[38] S. R. Vadali, and J. L. Junkins, "Optimal Open Loop and Stable Feedback Control of Rigid Spacecraft Attitude Maneuvers," *Jounrnal of the Astronautical Sciences,* vol. 32, no. 2, pp105-122.

[39] R. D. Robinett, G. G. Parker, H. Schaub, and J. L. Junkins, "Lyapunov Optimal Saturated Control for Nonlinear Systems," *Journal of Guidance, Control, and Dynamics,* vol. 20, no. 6, pp. 1083-1088.

[40] H. Schaub and J. L. Junkins, *Analytical Mechanics of Space Systems,* AIAA Education Series, 2009.

[41] K. Kim and Y. Kim, "Robust Back-stepping Control for Slew Maneuver using Nonlinear Tracking Function," *IEEE Transactions on Control Systems Technology*, vol. 11, no. 6, pp. 822-829, 2003.

[42] J. D. Koenig, "A Novel Attitude Guidance Algorithm for Exclusion Zone Avoidance," *IEEE Aerospace Conference,* ,vol. 14, pp. 1-10, IEEE Publications, Piscataway, NJ, 2009.

[43] J. T. Wen and K. Kreutz-Delgado, "The Attitude Control Problem," *IEEE Transactions on Automatic Control,* vol. 36, no. 10, pp. 1148-1162, 1991.

[44] D.E. Koditschek, "Application of a New Lyapunov Function to Global Adaptive Tracking," *Proceedings of the 27th Conference on Decision and Control,* Austin, Texas, Dec., pp. 63-68. 1988.

[45] D. E. Koditschek, "The Application of Total Energy as a Lyapunov Function for Mechanical Control Systems, *Contemporary Mathematics,* vol. 97, pp. 131-157, 1989.

[46] E. Frazzoli, M. A. Dahleh, E. Feron, and R. P. Kornfeld, "A Randomized Attitude Slew Planning Algorithm for Autonomous Spacecraft," *Proceedings of the AAIA Guidance, Navigation, and Control Conference*, 2001.

[47] R. P. Kornfeld, "On-board Autonomous Attitude Maneuver Planning for Planetary Spacecraft using Genetic Algorithms," *Proceedings of the AIAA Conference on Guidance, Navigation and Control*, 2003.

[48] R. A. Freeman and P. Kokotović, *Robust Nonlinear Control Design: State Space and Lyapunov Techniques,* Birkhäuser, 1996.

[49] H. K. Khalil, *Nonlinear Systems*, Prentice Hall, 2002.

[50] J. B. Kuipers, *Quaternions and Rotation Sequences*, Princeton University Press, 1999.

[51] H. C. Kjellberg and E. G. Lightsey, "Discretized Constrained Attitude Pathfinding and Control for Satellites," *Journal of Guidance, Control, and Dynamics,* 2013.

[52] P. Tsiotras, M. Corless, and J. M. Longuski, "A Novel Approach to the Attitude Control of Axisymmetric Spacecraft," *Automatica,* vol. 31, no. 8, pp. 1099-1112, 1995.

[53] D. Han, Q. Wei, and Z. Li, "Kinematic Control of Free Rigid Bodies using Dual Quaternions," *International Journal of Automation and Computing,* vol. 4, pp. 319-324, July 2008.

[54] W.M. Haddad, V. S. Chellaboina, J. L. Fausz, and A. Leonessa, "Optimal Nonlinear Robust Control for Nonlinear Uncertain Cascade Systems," *Proceedings of the American Control Conference,* vol.1, pp.403-407, 1997.

[55] J. P. Frakes, D. A. Henretty, T. W. Flatley, F. L. Markley, J. San, and E. G. Lightsey, "SAMPEX Science Pointing with Velocity Avoidance," *AAS/AIAA Spaceflight Mechanics Meeting,* Colorado Springs, CO, pp. 949-966, 1992.

[56] B. Wie and J. Lu, "Feedback Control Logic for Spacecraft Eigenaxis Rotations Under Slew Rate and Control Constraints," *Journal of Guidance, Control, and Dynamics,* vol. 18, no. 6, pp. 1372-1379.

[57] R. Sepulchre, D. A. Paley, and N. E. Leonard, "Stabilization of Planar Collective Motion with Limited Communication," *IEEE Transactions on Automatic Control*, vol. 53, no. 3, pp. 706-719, Apr. 2008.

[58] K. L. Moore and D. Lucarelli, "Forced and Constrained Consensus Among Cooperating Agents," *Proceedings in Networking, Sensing and Control,* pp. 449- 454, 2005.

[59] Y. Wu, X. Hu, D. Hu, and J. Lian, "Strapdown Inertial Navigation System Algorithms Based on Dual Quaternions," *IEEE Transaction on Aerospace and Electronic Systems*, vol. 41, no. 1. pp. 110-132, 2005.

[60] R. E. Mortensen, "A Globally Stable Linear Attitude Regulator," *International journal of control,* vol. 8, no. 3, pp. 297-302, 1968.

[61] C. R. McInnes, "Large Angle Slew Maneuvers with Autonomous Sun Vector Avoidance," *AIAA Journal of Guidance, Control and Dynamics*, vol. 17, no. 4, pp. 875-877, 1994.

[62] C. R. McInnes, "Nonlinear Control for Large Angle Attitude Slew Maneuvers," *Proceedings of the Third ESA Symposium on Spacecraft Guidance, Navigation, and Control*, pp. 543-548, 1996.

[63] C. R. McInnes, "Potential Function Methods for Autonomous Spacecraft Guidance and Control, *Advances in the Astronautical Sciences,* Univelt, Inc., San Diego, CA, vol. 90, pp. 2093-2109, 1996.

[64] Y. Kim and M. Mesbahi, "Quadratically Constrained Attitude Control via Semidefinite Programming," *IEEE Transactions on Automatic Control*, vol. 49, no. 5, pp. 731-735, 2004.

[65] N. B. Chaturvedi, A. Bloch, and N. McClamroch, "Global Stabilization of a Fully Actuated Mechanical System on a Riemanian Manifold Including Control Saturation Effects," *Proceeding of the 45th IEEE Conference on Decision and Control,* pp. 6116-6121, 2006.

[66] D. J. Bennet, C. R. McInnes, "Distributed Control of Multi-robot Systems using Bifurcating Potential Fields," *Robotics and Autonomous Systems*, vol. 58, pp. 256-264, 2010.

[67] R. Olfati-Saber and R. M. Murray, "Distributed Cooperative Control of Multiple Vehicle Formations using Structural Potential Functions," *The 15th IFAC World Congress,* Barcelona, Spain, Jul. 2002.

[68] R. Olfati-Saber, J. A. Fax, and R. M. Murray, "Consensus and Cooperation in Networked Multi-agent Systems," *Proceedings of the IEEE*, vol. 95, no. 1, pp. 215-233, Jan. 2007.

[69] U. Lee and M. Mesbahi, "Spacecraft Reorientation in Presence of Attitude Constraints via Logarithmic Barrier Potentials," *Proceedings of the 2011 American Control Conference*, no. 1, pp. 450-455, 2011.

[70] J. M. McCarthy, *An Introduction to Theoretical Kinematics*, MIT Press, 1990.

[71] A. Perez and J. M. McCarthy, "Dual Quaternion Synthesis of Constrained Robotic Systems," *Journal of Mechanical Design*, vol. 126, no. 3, pp. 425-435, 2004.

[72] R. Kristiansen and P. J. Nicklasson, "Satellite Attitude Control by Quaternion-based Backstepping," *Proceedings of American Control Conference*, Portland, Oregon, USA 2005.

[73] R. Kristiansen, A. Loria, A. Chaillet, P. J. Nicklasson, "Spacecraft Relative Rotation Tracking Without Angular Velocity Measurements," *Automatica*, 45 (2009), pp. 750-756, 2009.

[74] R. Olfati-Saber, "Flocking for Multi-agent Dynamic Systems: Algorithms and Theory," *IEEE Transaction on Automatic Control,* vol. 51, no. 3, pp. 401-420, Mar. 2006.

[75] R. Bach and R. Paielli, "Linearization of Attitude Control Error Dynamics," *IEEE Transactions on Automatic Control,* vol. 38, no. 10, pp. 1521-1525, 1993.

[76] M. Xin and H. Pan, "Indirect Robust Control of Spacecraft via Optimal Control Solution," *IEEE Transactions on Aerospace and Electronic Systems,* vol.48, no.2, pp.1798,1809, 2012.

[77] S. Bharadwaj, M. Osipchuk , K. D. Mease, K. D. Mease Zx, and F. C. Park, "Geometry and Inverse Optimality in Global Attitude Stabilization," *Journal of Guidance, Control, and Dynamics,* vol. 21, no. 6, pp. 930-939, 1998.

[78] D. P. Scharf, F. Y. Hadeagh and S. R. Ploen, "A Survey of Spacecraft Formation Flying Guidance and Control (part II): Control," *Proceedings of the 2004 American Control Conference*, Boston, Massachusetts, pp. 2976-2985, June 2004.

[79] K. Petersen and M. Pedersen *The Matrix Cookbook,* 2007.

[80] A. Berman and R. J. Plemmons, *Nonnegative Matrices in the Mathematical Sciences,* Society for Industrial and Applied Mathematics, 1994.

[81] A. Nedic, A. Ozdaglar, and P. A. Parrilo, "Constrained Consensus and Optimization in Multi-Agent Networks," *IEEE Transactions on Automatic Control,* vol.55, no.4, pp. 922-938, April 2010.

[82] N.M. Horri, P. Palmer, M. Roberts, "Gain-Scheduled Inverse Optimal Satellite Attitude Control," *IEEE Transactions on Aerospace and Electronic Systems,* vol.48, no.3, pp.2437,2457, 2012.

[83] G. Singh, G. Macala, E. Wong, and R. Rasmussen, "A Constraint Monitor Algorithm for the Cassini Spacecraft," *Proceedings of the AIAA Guidance, Navigation, and Control Conference,* pp. 272-282, AIAA, Reston, VA, 1997.

[84] F. Fahroo and I. M. Ross, "Direct Trajectory Optimization by a Chebyshev Pseudospectral Method," *Journal of Guidance, Control, and Dynamics,* vol. 25, no. 1, pp. 160-166, 2002.

[85] E. D. Jin and Z. W. Sun, "Robust Attitude Tracking Control of Flexible Spacecraft for Achieving Globally Asymptotic Stability," *International Journal of Robust and Nonlinear Control,* vol. 19, pp. 1201-1223, 2009.

[86] J. Stuelpnagel, "On the Parameterization of the Three-dimensional Rotation Goup," *SIAM Review,* vol. 6, no. 4, pp. 422-430, 1964.

[87] W. Ren, "Distributed attitude alignment in spacecraft formation flying," *International Journal of Adaptive Control and Signal Processing,* 21, pp. 95-113, 2007.

[88] A. V. Savkin, "Coordinated collective motion of groups of autonomous mobile robots: Analysis of Vicseks model," *IEEE Transaction on Automatic Control,* vol. 49, no. 6, pp. 981-982, Jun. 2004.

[89] S. Liu, and G. Trenkler, " "Hadamard, Khatri-Rao, Kronecker and other Matrix Products," *International Journal of Information and Systems Sciences,* vol. 4, no. 1, pp. 160-177, 2008.

[90] P. Tsiotras, "Further Passivity Results for the Attitude Control Problem," *IEEE Transactions on Automatic Control,* vol. 43, no. 11, pp. 1597-1600, 1998.

[91] A. Abdessameud and A. Tayebi, "Attitude Synchronization of a Group of Spacecraft without Velocity Measurements, *IEEE Transactions on Automatic Control,* vol. 54, no. 11, pp. 2642-2648, Oct. 2009.

[92] N. Filipe and P. Tsiotras, "Simultaneous Position and Attitude Control without Linear and Angular Velocity Feedback using Dual Quaternion," *Proceedings of the American Control Conference,* Washington DC, 2013.

[93] M. D. Shuster, "A Survey of Attitude Representations," *The Journal of the Astronautical Sciences,* vol. 41, no. 4, pp. 438-517, 1993.

[94] K. Spindler, "New Methods in On-board Attitude Control," *Advanced in the Astronautical Sciences*, vol. 100, no. 2, pp. 111-124, 1998.

[95] R. F. Stengel, *"Flight Dynamics"*, Princeton University Press,2004.

[96] J. R. Silvester, "Determinants of Block Matrices," *The Mathematical Gazette,* Vol. 84, No. 501 , pp. 460-467, Nov., 2000.

[97] D. Han, Q. Wei, Z. Li, and W. Sun, "Control of Oriented Mechanical Systems: A Method Based on Dual Quaternions," *Proceedings of the 17th IFAC World Congress,* Seoul, Korea, pp. 3836-3841, 2008.

[98] J. Wang and Z. Sun, "6-DOF Robust Adaptive Terminal Sliding Mode Control for Spacecraft Formation Flying," *Acta Astronautica,* vol. 73, pp. 676-687, 2012.

[99] L. Kavan, S. Collins, J. Zara, and C. O. Sullivan, "Geometric Skinning with Approximate Dual Quaternion Blending," em ACM Transactions on Graphics, vol. 27, no. 4, 2008.

[100] A. Tewari, *Atmospheric and Space Flight Dynamics: Modeling and Simulation with MATLAB,* Birkhauser, 2007.

[101] S. Boyd and L. Vandenberghe, *Convex Optimization*, Cambridge University Press, 2004.

[102] E. Pennestri and P. Valentini, "Dual Quaternions as a Tool for Rigid body Motion Analysis: A tutorial with an application to Biomechanics," *ECCOMAS Thematic Conference*, Poland, 2009.

[103] S. M. Joshi, A. G. Kelkar, and J. T. Wen, "Robust Attitude Stabilization of Spacecraft using Nonlinear Quaternion Feedback," *IEEE Transactions on Automatic Control,* vol. 40, no. 10, pp. 1800-1803, 1995.

[104] J. R. Wertz, *Spacecraft Attitude Determination and Control,* Kluwer, Norwell, MA, 1978.

[105] A. Ahmed, J. Alexander, D. Boussalis, W. Breckenridge, G. Macala, M. Mesbahi, M. San Martin, G. Singh, and E. Wong, *Cassini Control Analysis Book*, Jet Propulsion Laboratory, 1998.

[106] K. Bilimoria and B. Wie, "Time-Optimal Three-Axis Reorientation of a Rigid Spacecraft," *Journal of Guidance, Control, and Dynamics,* vol.16, no. 3, pp. 446-452.

[107] L. Lai, C. Yang, and C. Wu, "Time-Optimal Maneuvering Control of a Rigid Spacecraft," *Acta Astronauitica,* vol. 60, pp. 791-800.

[108] H. Bai, M. Arcak, and J. T.Wen, "Rigid Body Attitude Coordination without Inertial Frame Information, *Automatica,* vol. 44, no. 12, pp. 3170-3175, Dec. 2008.

[109] H. Bai, M. Arcak and J. T. Wen, "A Decentralized Design for Group Alignment and Synchronous Rotation without Inertial Frame Information," *Proceedings of the 46th IEEE Conference of Decision and Control*, New Orleans, LA, USA, pp. 2552-2557, 2007.

[110] A. Berman, R.S. Varga and R.C. Ward, "A L P S: Matrices with nonpositive off-diagonal entries," *Linear Algebra and its Applications,* vol. 21, no. 3, pp. 233-244, 1978.

[111] S. N. Singh and W. Yim, "Nonlinear Adaptive Backstepping Design for Spacecraft Attitude Control using Solar Radiation Pressure," *Proceedings of the 41th IEEE Conference on Decision and Control*, Las Vegas, Nevada, 2002.

[112] A. T. Yang, "Application of Quaternion Algebra and Dual Numbers to the Analysis of Spatial Mechanisms," Ph.D dissertation, Columbia University, 1963.

[113] Y. Ye, *Interior Point Algorithms,* John Wiley & Sons, Inc., 1997.

[114] Y. Kim, "Topics in Constrained Optimal Control: Spacecraft Formation Flying, Constrained Attitude Control, and Rank Minimization Problems," Ph.D dissertation, University of Washington, 2004.

[115] X. Wang and C. Yu, "Feedback Linearization Regulator with Coupled Attitude and Translation Dynamics Based on Unit Dual Quaternion," *IEEE Multi-Conference on Systems and Control*, 2010.

[116] J. Erdong and S. Zhaowei, "Robust Attitude Synchronization Controllers Design for Spacecraft Formation, *IET Control Theory & Applications,* vol. 3, no. 3, pp. 325-339, Mar. 2009.